DIRECT MONITORING OF METAL-CATALYZED REACTIONS USING ELECTROSPRAY IONIZATION MASS SPECTROMETRY

Thesis submitted at Charles University in Prague
in fulfillment of the requirements for
the PhD degree in Chemistry

by

Ing. Alexandra Tsybizova
Department of Organic Chemistry
Charles University in Prague, Faculty of Science

Supervisors: Dr. habil. Detlef Schröder; Prof. Mgr. Jana Roithová, Ph.D

Prague, June 2015

Contents

Frontispiece

"An original idea. That can't be too hard. The library must be full of them."

Stephen Fry

Declaration

The scientific work for the current thesis was performed at the Department of Physical-Organic Chemistry, Institute of Organic Chemistry and Biochemistry, AS CR, v.v.i., from January 2011 to March 2013. And from April 2013 to June 2015 at the Department of Organic Chemistry, Charles University in Prague.

I hereby declare that I have developed this thesis independently. All sentences or passages quoted in this project dissertation from other people's work have been specifically acknowledged by clear cross referencing to author, work and page(s). I understand that failure to do this amounts to plagiarism and will be considered grounds for failure in this module and the degree examination as a whole. While discussing the results in the current dissertation, self plagiarism was avoided to the maximum possible extend.

The current dissertation work has not been used for the acquisition of any other academic qualification.

Name: Alexandra Tsybizova

Signed:

Date:

Acknowledgment

The preparation of this dissertation thesis would not have been possible without the involvement of many people.

First I would like to warmly thank both of my supervisors - Dr. Detlef Schröder and Prof. Jana Roithová. Both of them provided a great source of inspiration and admiration for me. I am very grateful for the opportunity not only to learn and expand my knowledge, but also for the ability to test and freely share my ideas, even those that did not necessarily lead to the successful solutions. I would also like to thank Drs Schröder and Roithová for their unique ability to boost my optimism, at the most dark moments of my research, when it seemed that the project reached the dead end.

Loosing Detlef suddenly and unexpectedly on August 22, 2012 in the age of 49 was a great shock and tragedy for all who knew him. I believe that his untimely passing was a great loss to the scientific community as a whole, and I still terribly miss him, bursting with ideas, optimism and generosity.

Secondly, I want to thank my collaborators, who contributed to the projects discussed below: Tibor András Rokob and Lubomír Rulíšek for the theoretical calculations that were done for the Ni-PhPy project; Andrew Gray for his calculations for the C-H activation project; Bradford L. Ryland and Shannon S. Stahl for the EPR measurements for the $Cu(OAc)_2$ speciation. The discussion of the obtained results would not have been complete without their contribution. I would also like to thank Anna Březinová for the GC-MS measurements of the purity of the phenylpyridine samples for the Ni-PhPy project.

Thirdly, many thanks to my former and current group mates: Christopher Shaffer, Divya Agrawal, Ágnes Rokobné Révész, Ján Tarábek, Anton Škríba, Jakub Hývl and many others from both Detlef's and Jana's group for the constant readiness to help, and a friendly atmosphere. Andrew Gray I cannot only praise as an excellent research partner, being ready to test all of my crazy ideas, but also as a good friend with whom I am happy

to co-author a research paper. I would also like to thank him for reading the current dissertation, as well as his valuable comments during its preparation. Special thanks to Eric Andris, whose awesome Python programs made the extraction of the data from spectra series (CID, kinetics) a lot more easier and less time consuming.

I would also like to thank my family and especially my husband for the constant support and belief in my abilities.

Last, but not least, I am grateful for the financial support provided from the following organizations and facilities:

- Academy of Sciences of the Czech Republic (RVO 61388963)
- the European Research Council (AdG HORIZOMS)
- the Grant Agency of the Czech Republic (207/11/0338, 207/12/0846 and No. 14-20077S)
- The results from CLIO were obtained with funding from the European Union´s Seventh Framework Programme (FP7/2007-2013) under the grant agreement No. 226716. CLIO staff, particularly Philippe Maître and Vincent Steinmetz, are acknowledged for their help and assistance

Abstract

The current dissertation thesis is focused on the investigation of metal-catalyzed reactions using electrospray ionization mass spectrometry as the primary research technique. However, other gas-phase methods such as tandem mass spectrometry, infrared multiphoton dissociation spectroscopy and quantum chemical calculations have also been involved to unravel and support the findings and proposals. As organometallic chemistry is a very broad and complicated topic, this thesis is only focused on a few projects. The first of them is dedicated to copper acetate speciation in organic solvents, the second - to the mechanistic investigation of copper catalyzed aerobic cross coupling of thiol esters and arylboronic acids, the third project studied coordination and bond activation of nickel(II) - phenylpyridine complexes and carboxylate assisted C-H activation reactions were investigated last.

Předkládaná dizertační práce je zaměřena na studium reakcí katalyzovaných kovy s použitím hmotnostní spektrometrie spojené s elektrosprejovou ionizací představující základní metodu výzkumu. Nicméně další metody jako tandemová hmotnostní spektrometrie, infračervená multifotonová disociační spektroskopie a kvantově chemické výpočty byly použity pro dořešení a podporu výsledků a návrhů. Organokovová chemie zahrnuje širokou škálu často velmi komplikovaných témat, tato práce je zaměřena na řešení pouze několika z nich. První část dizertační práce se věnuje studiu chování acetátu mědi v organických rozpouštědlech, druhá výzkumu mědí katalyzovaného aerobního cross couplingu thiolesterů a arylboronových kyselin, třetí studiu koordinace a vazebné aktivace nikl(II) - fenylpyridiniových komplexů a poslední výzkumu karboxylátem asistované C-H aktivace.

Chapter 1

Literature overview and aims of the present work

1.1 Metal catalysis in contemporary organic synthesis

The discovery of cross-coupling reactions has brought about the breakthrough of organometallic chemistry, which was recently acknowledged by award of the Nobel Prize in Chemistry (2010) [1–4]. These reactions have dramatically changed the synthetic approach of many natural compounds, supramolecular materials or polymers, and many well-known organic molecules; in the past their synthesis required many more steps than nowadays [5].

Therefore the mechanistic investigation of metal-catalyzed reactions has become a "hot topic" in contemporary organic chemistry, as their mechanisms greatly differ from what is considered a classical mechanistic scheme (*e.g.* Ad_E or S_N2). The first difference is the presence of the catalytic cycle and recovery of the metal catalyst. The second is the formation of metalloorganic complexes, which are sometimes difficult to characterize and study. Many of them are unstable at normal conditions and require careful handling (*e.g.* under the atmosphere of an inert gas). The situation is also complicated by the constant growth of various catalytic species that may behave differently in the catalytic cycle.

Rational design of catalytic complexes represents a popular challenge as many catalytic species are difficult and expensive to synthesize. Such design allows evaluation of the possible properties and estimation of catalytic activity [6].

1.2 Reaction mixture monitoring and ESI-MS

Reaction mixture monitoring is widely used nowadays for mechanistic investigations of new reactions. It has a wide potential allowing for kinetic studies, establishment of the reaction end points and modification of the synthetic procedure (improve yields, reduce catalyst loading and by-product formation, make the reaction more environmentally friendly, *etc.*). Among many available techniques nuclear magnetic resonance, infrared spectroscopy and mass spectrometry are used frequently.

Electrospray ionization mass spectrometry (ESI-MS) is very popular for reaction monitoring. An ideal reaction for ESI-MS studies would proceed at room temperature, in a polar volatile solvent (*e.g.* acetonitrile, methanol, or water), in ambient atmosphere and would contain ionic reaction intermediates for easy detection and characterization. Organometallic reactions fulfill most of these requirements and therefore are popular for investigations with ESI-MS. ESI is also a soft method for ion transfer from solution to the gas phase [7–9], and has been called the "major tool for the investigation of reaction mechanisms" [10–12]. Moreover, mass spectrometry allows for the advantageous investigation of both the intermediates properties in greater detail, and the thermodynamic and kinetic properties of elemental reaction steps [13,14].

In principle, there are two ways to investigate a reaction mixture using mass spectrometry: on-line and off-line monitoring. Off-line monitoring indicates that the reaction mechanism is being investigated in many steps, requiring the analysis of various differently prepared mixtures (with different amounts, concentrations or numbers of reagents in the mixture, as well as the use of different solvents). These condition changes, ideally, allow for the generation of different reaction intermediates that can be characterized by tandem mass spectrometry.

On the other hand, an on-line approach requires the determination of reaction mixture composition over time, and can be done either by repetitive sampling from an investigated reaction mixture at fixed time intervals, or by the direct connection of a reactor to the ionization source. The latter option can not only be achieved under atmospheric pressure [15,16] (see Figure 1.1a), but also using a glovebox - to maintain special reaction conditions (see Figure 1.1b) [17]. It should be kept in mind that continuous flow monitoring methods are not suitable for heterogeneous reactions, because they can cause capillary blockage and lead to signal loss. On the other hand, repetitive sampling from the reaction

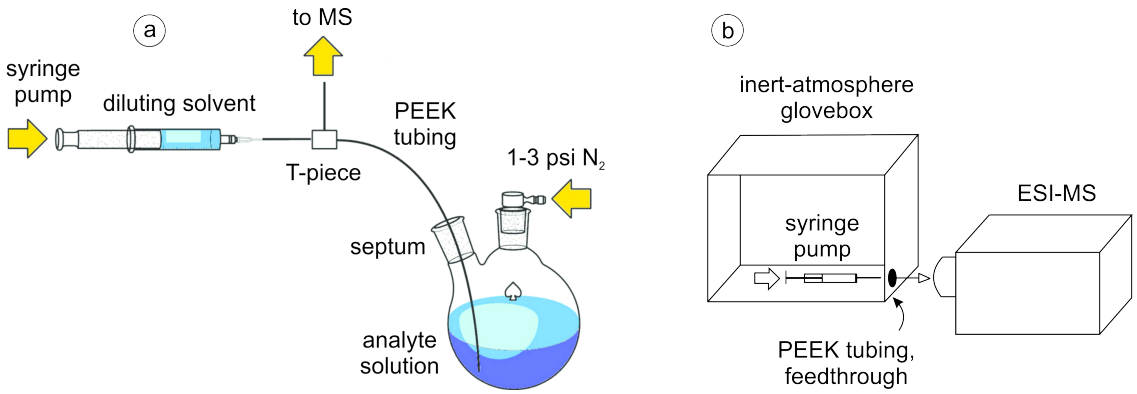

Figure 1.1: a) Continuous pressurized sample infusion (PSI), set-up with on-line sample dilution *via* a syringe pump (reprinted from [16], copyright (2012) with permission from Elsevier); b) Inert-atmosphere glovebox situated next to the ESI mass spectrometer. Syringe pump for sample infusion is located inside the glovebox; the PEEK tubing passes through a standard glovebox feedthrough sealed with O-rings. Adapted from [17].

mixture allows these difficulties to be overcome [18]. The combination of recently developed paper-spray ionization with MS is also worth mentioning as it provides a convenient way for on-line monitoring [19,20].

In spite of the advantages that ESI-MS monitoring brings, one should be very careful with the interpretation of its results. The very first question that every solution chemist would have in mind is whether ESI-MS can, in fact, characterize, or at least predict solution properties [21–23]. Recently, an example fully illustrating this skepticism was published in Organometallics [24–26]. The discussion was concentrated on the mechanism of C-H bond activation of benzene catalyzed by Pt(II) diimine complexes. It is therefore important for both gas-phase and synthetic chemists to work in parallel, in order to provide a unified view of the investigated problem. Thus, combination with different methods (infrared spectroscopy, NMR, crystallography, *etc.*) is often required for the full interpretation of ESI-MS results, providing a good base for the reaction mechanism establishment.

1.3 Metal-catalyzed reaction mechanisms studied in the gas phase

There are many approaches for the gas-phase analysis of a catalytic reaction [23]. Investigation of metal-catalyzed reactions is often straightforward as metal intermediates that are either charged or could be easily charged are formed during the catalytic course. ESI-MS can efficiently "fish out" reactants, products and intermediates, isolate them in

the gas phase and subject them to more detailed investigation. Structural information is often gained by coupling of ESI-MS with tandem mass spectrometry and/or IRMPD spectroscopy [27,28]. The reactivity of the mass-selected species can also be investigated *via* ion-molecule reactions in the collision cell. This can eliminate solution-phase effects from the solvent, counterions or pH [29,30]. ESI-MS can therefore detect and characterize reactant, product and intermediate complexes in order to map a reaction mechanism.

Reaction intermediates that are not easily chargeable (*e.g.* by protonation) can be detected upon introduction of a charged tag. A charged tag is usually a remote group, artificially introduced either to a substrate or catalyst molecule, that is bearing a charge (for example, trimethylamonium or sulphonic group) and does not influence the course of the reaction [31,32].

In this section a few gas-phase investigations of metal-catalyzed reaction mechanism are described, in order to fully illustrate the power of the method.

1.3.1 Copper mediated naphthol coupling

The mechanism of naphthol coupling, catalyzed by copper(II), was revealed by the combination of ESI-MS, ion spectroscopy and tandem mass spectrometry (Scheme 1.1) [33,34]. To this end, a mixture of methyl-3-hydroxy-2-naphtholate (**1**) and Cu(OH)Cl-TMEDA was subjected to ESI-MS experiments. The spectra revealed the formation of two intermediate complexes assigned as $[(\mathbf{1}\text{-H})\text{Cu(TMEDA)}]^+$ and $[(\mathbf{1}\text{-H})_2\text{Cu}_2\text{Cl(TMEDA)}_2]^+$.

Previous studies on the same reaction suggested that mononuclear species were the key intermediates in the catalytic cycle. Behaving as carbon-centered radicals these intermediates could couple to the second naphthol molecule to yield binol **2**. Accordingly, the reactivity of the observed mononuclear complex $[(\mathbf{1}\text{-H})\text{Cu(TMEDA)}]^+$ was tested in the collision cell with CH_3–S–S–CH_3 and CH_3–Se–Se–CH_3. If $[(\mathbf{1}\text{-H})\text{Cu(TMEDA)}]^+$ behaved as a C-centered radical, homogeneous cleavage of the S-S or Se-Se bond would be expected, however no reaction was observed. Therefore, the $[(\mathbf{1}\text{-H})\text{Cu(TMEDA)}]^+$ complex would not be capable of reacting with a second naphtole molecule.

The $[(\mathbf{1}\text{-H})\text{Cu(TMEDA)}]^+$cation structure was also checked by IRMPD spectroscopy [34]. Figure 1.2a shows the comparison of the experimental IRMPD spectrum and the theoretical IR spectrum of the most stable structure found for the corresponding complex. Careful analysis of the experimental bands revealed that the unpaired electron is localized at the copper(II) center and therefore the structure cannot represent a C-radical. These observa-

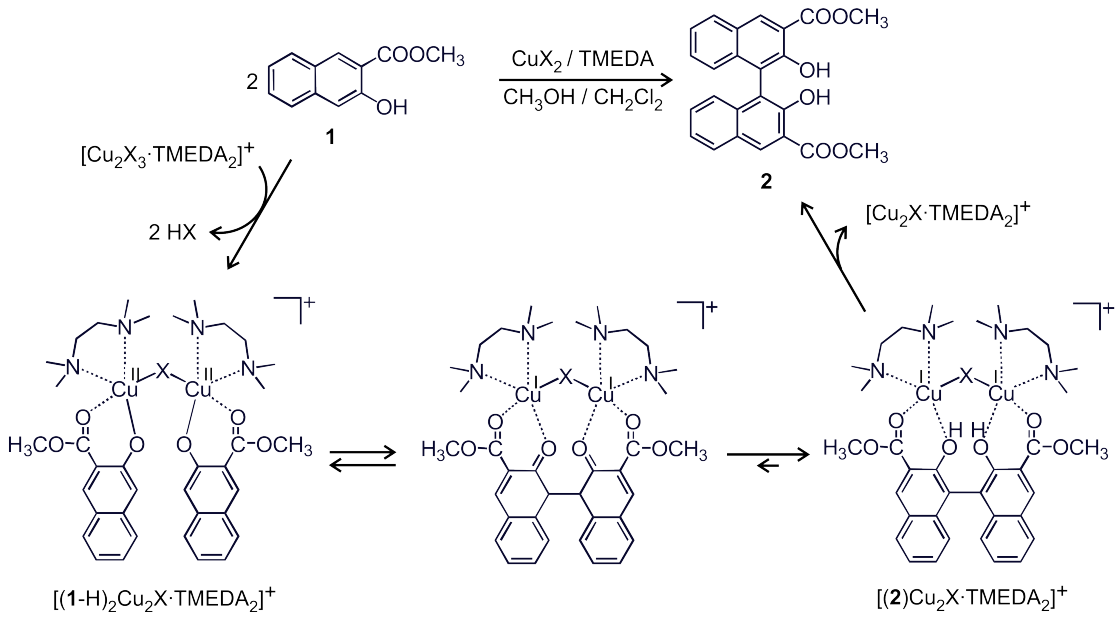

Scheme 1.1: Mechanism for naphthol coupling mediated by a binuclear copper complex, where metals are bound *via* a counterion X (X = NO_3^-, Cl^-, or Br^-) and each metal atom bears a TMEDA ligand and deprotonated naphthol. Adapted according to [33].

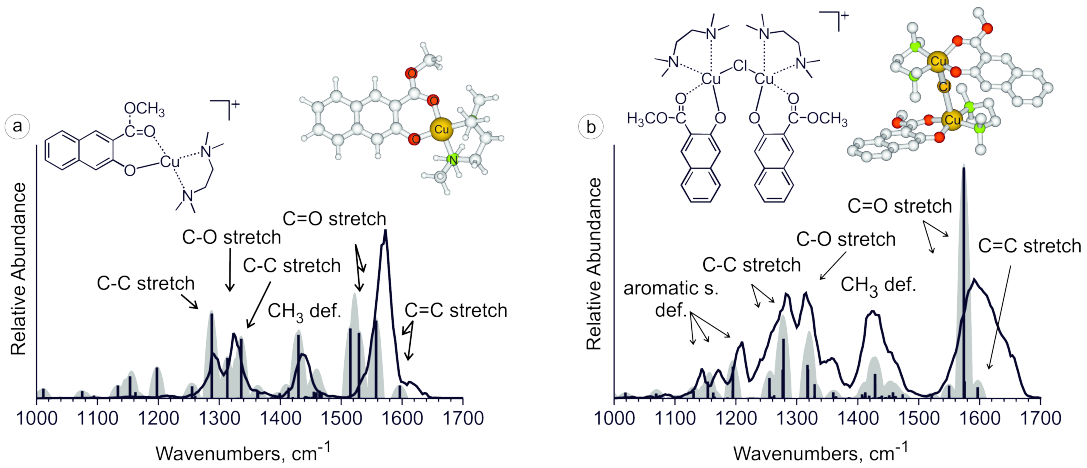

Figure 1.2: IRMPD spectra (black lines) of a) [(**1**-H)Cu(TMEDA)]$^+$ and b) [(**1**-H)$_2$Cu$_2$Cl (TMEDA)$_2$]$^+$ compared with the theoretical IR spectra (black bars) calculated at the B3LYP/6-311+G*(Cu):6-31G*(C,O,N,H) level (scaling factor 0.95). The gray areas show the theoretical spectra folded with Gaussian peak shapes with a FWHM (full width at half maximum) of 20 cm^{-1}. In the shown structures copper is represented in yellow, oxygen in red, nitrogen in green, and carbon and hydrogen atoms in gray; for clarity, the hydrogen atoms are removed in b). Adapted from [34].

tions suggested that that the $[(\mathbf{1}\text{-H})Cu(TMEDA)]^+$ complex would not react with a second inactivated naphthol molecule to yield the binol **2**.

Therefore the investigation turned to the binuclear complex $[(\mathbf{1}\text{-H})_2Cu_2Cl(TMEDA)_2]^+$ as the potential key reaction intermediate. CID experiments on this complex revealed three fragmentation channels: i) dissociation into complexes $[(\mathbf{1}\text{-H})Cu(TMEDA)]^+$ and $[(\mathbf{1}\text{-H})CuCl(TMEDA)]^+$, ii) loss of the TMEDA ligand and iii) the elimination of the binol **2**. IRMPD studies on the complex $[(\mathbf{1}\text{-H})_2Cu_2Cl(TMEDA)_2]^+$ (Figure 1.2b) revealed that it contains two naphthoxo ligands, separated from each other. Therefore, elimination of binol **2** is a sign of a C-C coupling reaction that can be induced by collisional activation.

1.3.2 Methanol to alkyne addition catalyzed by gold

In 2012 gold(I)-mediated addition of methanol to alkynes (see Scheme 1.2) was investigated by means of ESI-MS, NMR, IRMPD and theoretical calculations [35].

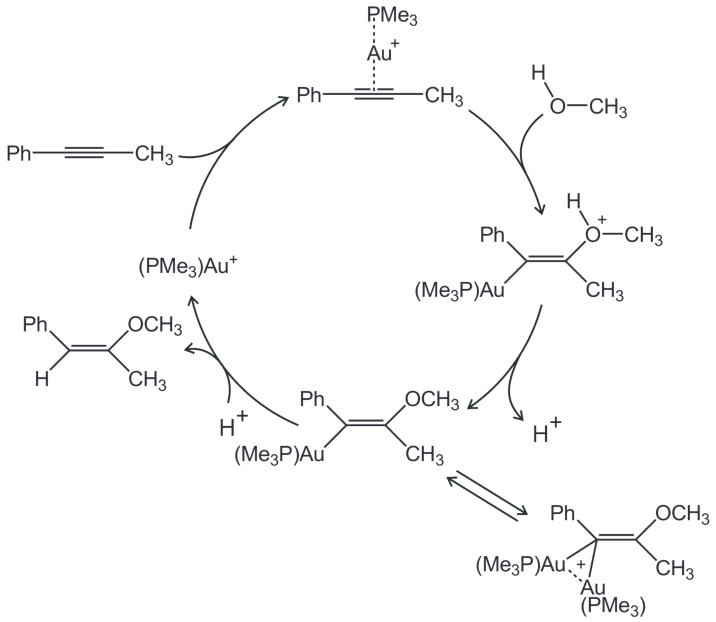

Scheme 1.2: The mechanism of methanol addition to alkynes, catalyzed by gold (I).

To this end, a reaction mixture containing 1-phenylpropyne and $AuCl(PMe_3)$ was investigated. ESI of the mixture of 1-phenylpropyne with the catalyst led to the formation of ion **X** assigned as $[(PMe_3)_2Au_2(OCH_3)(PhCCMe)]^+$ which could correspond to a possible intermediate. The behaviour of this ion was investigated in experiments with CD_3OD. Thus, 1-phenylpropyne was mixed with $AuCl(PMe_3)$ in CD_3OD, kept for one hour, diluted to a double volume by CH_3OH and immediately sprayed to the mass spectrometer. The spectra recorded at the very beginning of the experiment showed dominant abundance of

the [D_3]-**X** complex, whereas after 20 minutes the statistically expected 1:1 ratio of the unlabeled **X** and the labeled [D_3]-**X** complexes was established (Figure 1.3).

The mass spectrum in Figure 1.3 also shows the generation of species **Y** (m/z 421) at minor abundances which corresponds to a complex between a (trimethylphosphino)gold cation and the product of a methanol addition to 1-phenylpropyne. Thus intermediate **X** could formally be related to **Y** by replacement of H by $AuPMe_3$. Likewise, in the experiments with CD_3OD, only the fully deuterated version of **Y** was observed in the beginning (Figure 1.3c).

Therefore, the labeling experiments demonstrated that the ions **X** and **Y** are formed in the solution and thus are not ESI-MS artifacts. The experiment also allowed determination of the half-life of **X**, which was about 3.7 minutes at 25°C in the reaction solution.

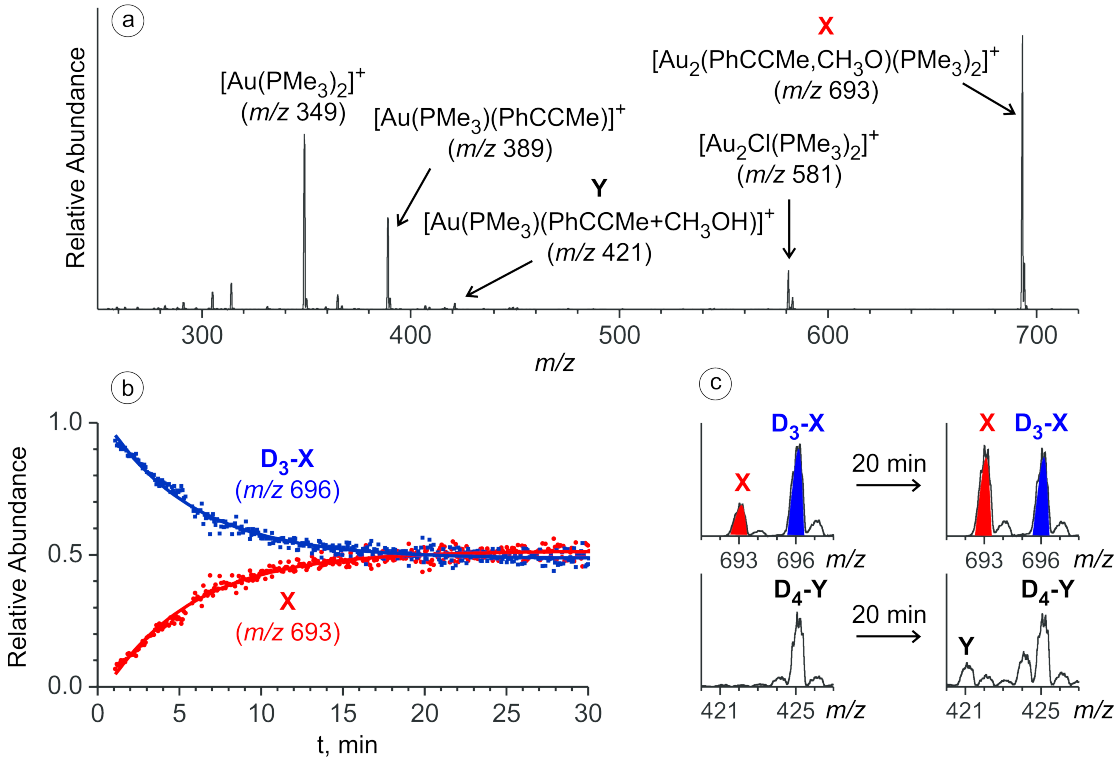

Figure 1.3: a) ESI-MS source spectrum of a MeOH solution of 1-phenylpropyne with catalyst (2.5 mol % [$AuCl(PMe_3)$]/3 mol % $AgSbF_6$). b) Time dependence of the relative abundances of [D_3]-**X** and **X** upon adding CH_3OH to a solution of 1-phenylpropyne in CD_3OD and the catalyst after 1 hour reaction time. The solid lines correspond to the fitted exponential functions. c) The averaged spectra sections in the beginning (1–5 min) and in the end (26–30 min) of the experiment. The figure is adapted from [35].

Subsequent IRMPD and DFT studies on the $[(PMe_3)_2Au_2(OCH_3)(PhCCMe)]^+$ cation

helped to reveal its structure and account for the reaction mechanism (Scheme 1.2) as well as the role of diaurated complex in it.

1.3.3 Intramolecular aliphatic C-H bond activation catalyzed by Cu(II)

In 2012 Shaffer *et al.* investigated intramolecular aliphatic C-H bond activation catalyzed by copper (II) [36]. For that, the reactive substrate **2** was synthesized according to Scheme 1.3 and subjected to ESI-MS together with $Cu(NO_3)_2$ catalyst for the generation of $[(\mathbf{2})Cu(NO_3)]^+$. CID of $[(\mathbf{2})Cu(NO_3)]^+$ showed the major fragment pathway to be the ester cleavage and subsequent octene elimination (leading to the formation of $[(\mathbf{1})Cu(NO_3)]^+$). The minor fragmentation pathway is the loss of NO_2 , which leads to the formation of $[(\mathbf{2})CuO]^+$.

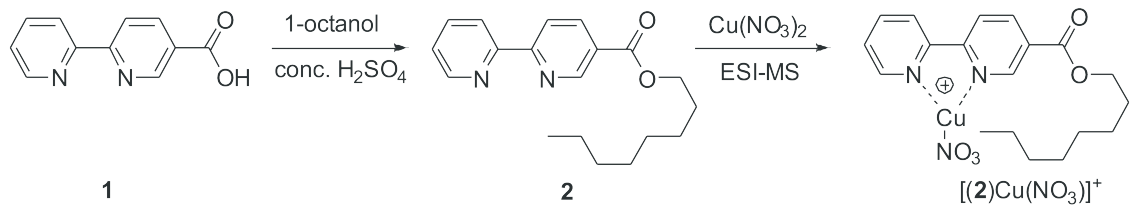

Scheme 1.3: Synthesis of the precursor **2** followed by ESI-MS to generate $[(\mathbf{2})Cu(NO_3)]^+$.

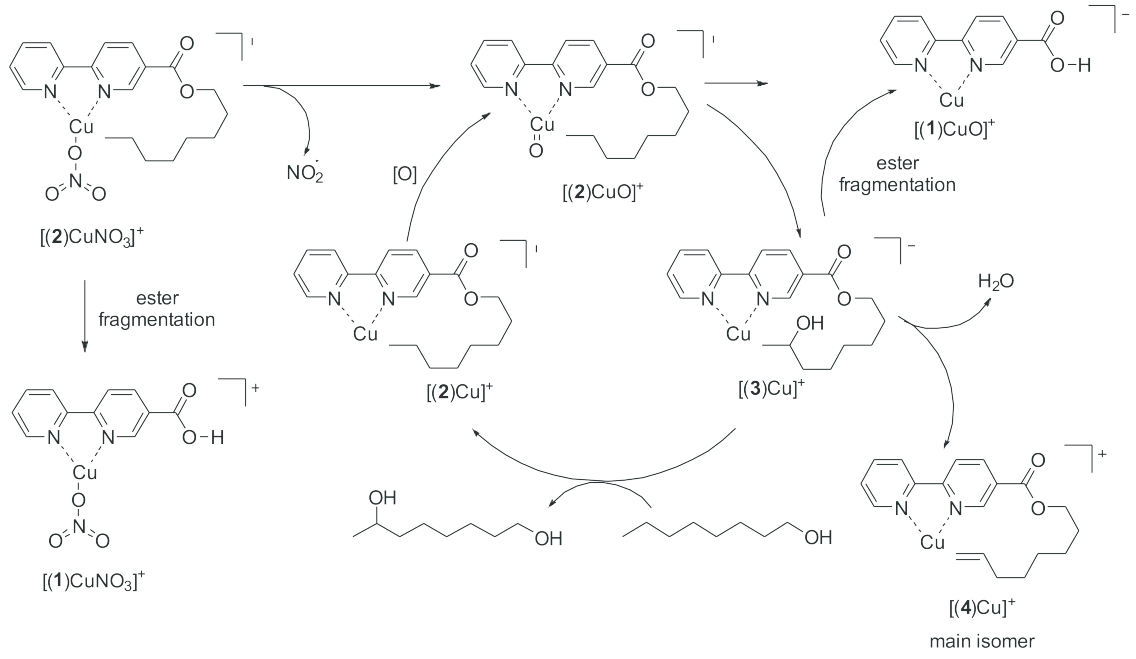

Scheme 1.4: Gas-phase reactivity and theoretical completion of catalytic cycle. Adapted from [36].

The MS^3 experiments on $[(\mathbf{2})CuO]^+$ again revealed two fragmentation channels: either

the elimination of a water molecule, or the formation of $[(\mathbf{1})Cu]^+$ (which most likely occurs due to the ester cleavage). The former elimination channel suggests that the complex undergoes a C-H activation reaction at ligand **2**. Experiments with a deuterium labeled ligand **2** have proved this suggestions and moreover revealed that the activation occurs selectively at the terminus of the alkyl chain.

Ion mobility mass spectrometry experiments gave further information about the structure of the investigated ions. The arrival times for most of the studied ions were linearly dependent on their m/z ratio. However, the mobilities for $[(\mathbf{2})CuO]^+$ and $[(\mathbf{2}\text{-}H_2O)Cu]^+$ were significantly greater than expected, which pointed out conformational changes for these two ions with respect to the other investigated ions. Therefore it was suggested that the changes in conformation are caused by hydroxylation of the side chain by the reactive copper(III) oxo precursor.

Finally, the mechanism for the C-H activation was proposed (Scheme 1.4).

1.3.4 Cobalt catalyzed Diels-Alder reaction

In recent studies on the mechanism of the Diels-Alder reaction (Scheme 1.5) Fiebig and coworkers investigated intermediates using mass spectrometry [37]. In brief, it was shown that the catalyst $CoBr_2(dppe)$ is reduced *in situ* by Zn/ZnI_2 to form the reactive catalytic cobalt (I) species $[Co(dppe)]^+$. The reactivity of these species with isoprene and phenylacetylene was further tested in the collision cell. It was shown that the central solution-phase intermediate $[Co(dppe)(isoprene)(phenylacetylene)]^+$ could also be generated in the collision cell upon ion/molecule reactions. The CID of $[Co(dppe)(isoprene)(phenylacetylene)]^+$ showed the elimination of the product molecule and thus the occurrence of a collision induced Diels-Alder reaction.

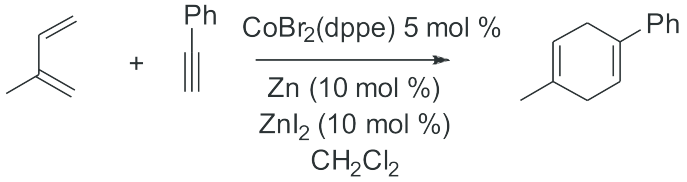

Scheme 1.5: Cobalt-catalyzed Diels−Alder reaction of phenylacetylene and isoprene.

1.4 Aims and objectives of the current work

Development of efficient on-line monitoring techniques for organometallic reactions is important. Ideally, it should provide rapid and accurate kinetic data that is useful for fundamental mechanistic investigations as well as synthesis optimization and other areas of research.

The aim of the current dissertation work was the investigation of metal catalyzed reaction mechanisms with ESI-MS using suitable reaction monitoring methods.

Chapter 2 describes the methods and instruments that were used in the current dissertation.

Chapter 3 is focused on the results, namely, for projects that were also published as individual research papers:

- A. Tsybizova, B. L. Ryland, N. Tsierkezos, S. S. Stahl, J. Roithová, D. Schröder, Speciation Behavior of Copper(II) Acetate in Simple Organic Solvents – Revealing the Effect of Trace Water, Eur. J. Inorg. Chem. 2014, 1407-1412
- A. Tsybizova, D. Schröder, J. Roithová, A. Henke, J. Šrogl, Gas-phase studies of copper catalyzed aerobic cross coupling of thiol esters and arylboronic acids, J. Phys. Org. Chem. 2014, 27, 198 – 203.
- A. Tsybizova, L. Rulíšek, D. Schröder, T. A. Rokob, Coordination and Bond Activation in Complexes of Regioisomeric Phenylpyridines with the Nickel(II) Chloride Cation in the Gas Phase. J. Phys. Chem. A., 2012, 117, 1171-1180
- A. Gray, A. Tsybizova, J. Roithová, Carboxylate-Assisted C-H Activation of Phenylpyridines: A Mechanistic Study, submitted

Chapter 2

Instrumentation and methods

This dissertation covers research that was done using a wide range of techniques, both experimental and theoretical. Existing literature provides a great depth of information, regarding these methods. Therefore, this chapter will only briefly summarize the most important aspects.

2.1 Electrospray ionization

Electrospray ionization (ESI) is probably the most widely used ionization method in mass spectrometry [39]. Since its introduction by Fenn [7,9] in 1984, its use has grown rapidly, especially for the analysis of macromolecules that do not usually survive hard ionization conditions. There are two major theories that explain ion formation during ESI: the ion evaporation model (IEM) and the charge residue model (CRM).

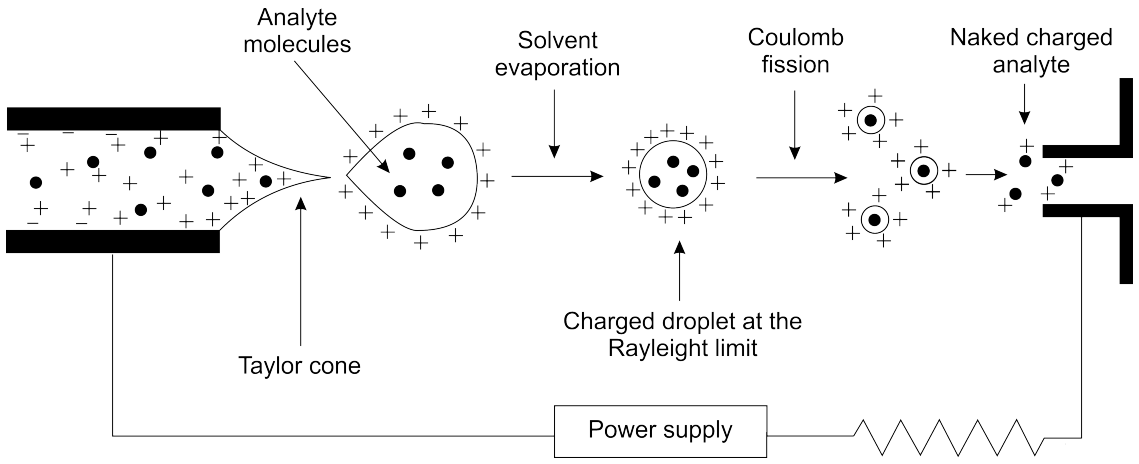

Figure 2.1: Schematic representation of the CRM for the ESI process. Adapted from [38].

In the CRM the process of ion formation can be divided into 3 major steps (Figure 2.1): i) formation of charged droplets (aerosol) from the solution exiting of the electrospray capillary, ii) shrinkage of the charged droplets due to the solvent evaporation, and finally iii) release of the naked ions into the gas phase.

The investigated solution is transferred to the electrospray capillary, which has a high voltage (usually 3-5 kV) applied to it. At the edge of the capillary tip the liquid becomes charged and briefly forms a cone shape (Taylor cone). The droplets then burst away from each other, creating a highly charged aerosol. Then, charged droplets are led into the evaporation chamber, where the solvent from the droplets is evaporated with assistance of a gas (usually nitrogen). When charges are pushed close together they repel each other (Coulombic repulsion) dividing the droplets into smaller pieces. The process of the gradual shrinking/repulsion is repeated until the point when no solvent is left.

The major difference of the IEM when compared with the CRM is that the final ion is produced by desorption rather than by solvent evaporation from the droplet [40,41]. There is evidence that smaller ions prefer to be delivered to the gas phase by the ion evaporation model, while larger ions as, for example, proteins, are liberated by the charge residue model [41–43].

It should be taken into the account that ESI conditions can dramatically affect the speciation of the investigated mixture. Thus, typical ESI-MS operational conditions that were optimized for the investigation of large multiply charged biomolecules are of limited use for organometallic complexes. An example of such an effect was shown by Schröder *et al.* in studies of $[Cu(urea)]^+$ complexes [44]. At low capillary voltages the multimeric clusters were preferred, whereas high voltages caused cluster breakage (so-called source fragmentation) leading to the formation of monomers.

2.2 Quadrupole ion trap mass spectrometer

The ESI quadrupole ion trap (QIT) mass spectrometer represents the combination of two Nobel Prize winning technologies: electrospray ionization and the quadrupole ion trap [9,46,47].

Most of the experiments for this dissertation were performed on a Finnigan LCQ Classic ion trap mass spectrometer (Figure 2.2) bearing a conventional ESI source that consisted of a spray unit connected to a syringe pump (typical applied flow rates: 0.3-0.7 mL/h).

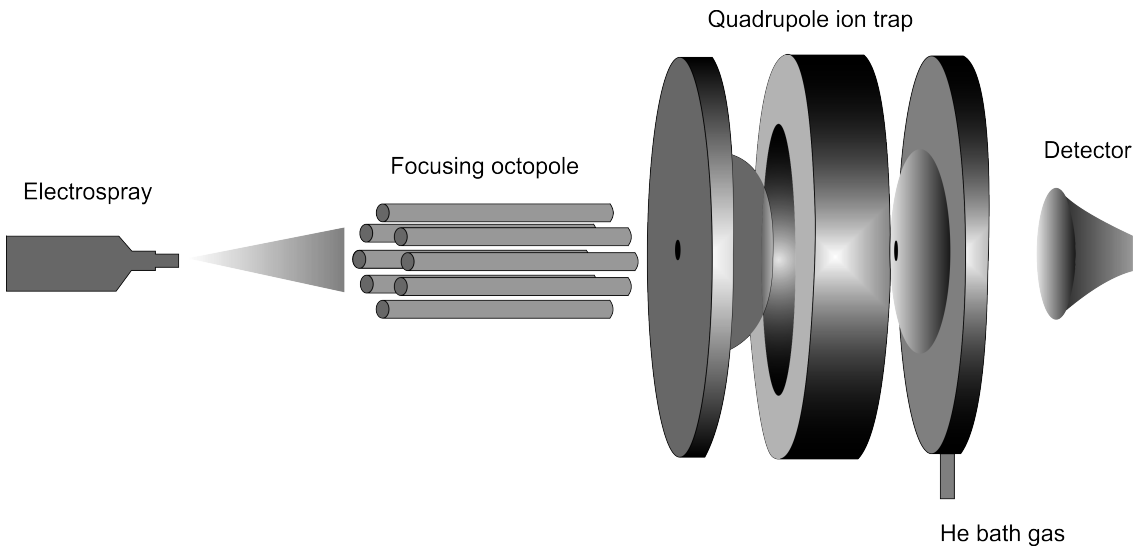

Figure 2.2: Simplified schematic diagram of the ESI-QIT mass spectrometer. The figure is adapted from [45].

Nitrogen was used as a sheath and, when required, auxiliary gas. After the ESI the ions are directed into a heated transfer capillary, usually kept in the range 100-200°C, and then through the first set of lenses that determined the ionization conditions (hard or soft by varying the degree of collisional activation in the medium-pressure regime) [44, 48]. After exiting from the lenses the ions travel through two transfer octopoles and end in a Paul ion trap [47, 49]. The ions are stored in the ion trap in the presence of the bath gas (usual He, 10^{-3} mbar) and ejected from the ion trap to an electron multiplier for detection.

For ion isolation in MS^n experiments, where possible, the isolation width was adjusted to select a single nominal mass and the lightest isotope (*e.g.* ^{1}H, ^{12}C, ^{32}S, ^{63}Cu). We found an isolation width of 1-2 amu to be sufficient for that purpose. The whole isotopic range (typically, m/z 10-15) for a selected ion was used when the mass-selection of a single isotope did not provide an intensity sufficient for further MS^n experiments. Instrument control and data analysis were performed with Xcalibur software version 2.0 (Thermo Fisher Scientific, Waltham, MA, USA)

It should be mentioned in passing that mass spectrometric experiments are usually affected by the presence of solvent molecules (acetonitrile, water, *etc.*) in the ion trap and their ability to attach to the investigated ion. This happens due to the relatively short distance between the inlet system and the trap. Moreover, memory effects from previous measurements can be quite disruptive, as previously used compounds as well as solvents can stay in the instrument for a long time.

2.3 Ion mobility mass spectrometry

In early 60's McDaniel and co-workers introduced the idea of gaseous ion separation in a drift tube, by attaching a low-field ion mobility drift cell to a sector mass spectrometer. At that time it was done for the study of ion-molecule reactions [50]. However the potential of such separation was not fully realized until it was demonstrated for protein conformers by Clemmer *et al.* [51].

Ion mobility spectrometry (IMS) seperates ions in accordance with their shape, and is often called "chromatography in the gas phase" [52,53]. During this analysis, the investigated ions are directed into a chamber with a weak electric field, filled with an inert gas. While traversing the chamber, the ions reduce their speed by undergoing a number of collisions with the neutral gas molecules. Larger ions undergo more collisions and therefore require more time to elute from the chamber than the smaller ions.

The result of coupling IMS with mass spectrometry is often called ion mobility mass spectrometry (IM-MS). These two analytical methods perfectly complement one another and therefore IM-MS has become one of the most rapidly developing techniques in analytical chemistry. Although IM-MS is mostly used for the analysis of complex biological mixtures, the separation of small molecules is also possible [54]. For example, IM-MS of the *p*-hydroxybenzoic acid solution is capable of tautomer separation in the gas phase [55]. The IM-MS results discussed in this dissertation were obtained with a SYNAPT G2 mass spectrometer (WATERS, Manchester, U.K.), equipped with an ESI source (see Figure 2.3). The instrument consists of four main regions: ion generation, ion selection, ion mobility separation and ion mass analysis. After the ions are generated in the ESI source, a traveling waveguide transfers them to the quadrupole analyzer (capable of detecting ions up to 32000 m/z). After being selected, the ions are transferred into the ion mobility cell. When the ion mobility mode is switched on, the ions are collected in the linear argon filled ion trap from which they are emitted in a single pulse to the ion mobility cell filled with $\sim$2 mbar of nitrogen. After the mobility cell, the ions pass a transfer cell and end up in the reflectron time-of-flight mass spectrometer. The absolute values of the arrival times (t_a) in the SYNAPT G2 depend on the voltage and pressure settings. Therefore, any comparison between different arrival times should be done under identical conditions [56]. Also, different options exist for energizing the ions in the SYNAPT instrument [57]. As such, the ionization conditions (soft to hard) can be modified by changing the cone voltage (U_C) in

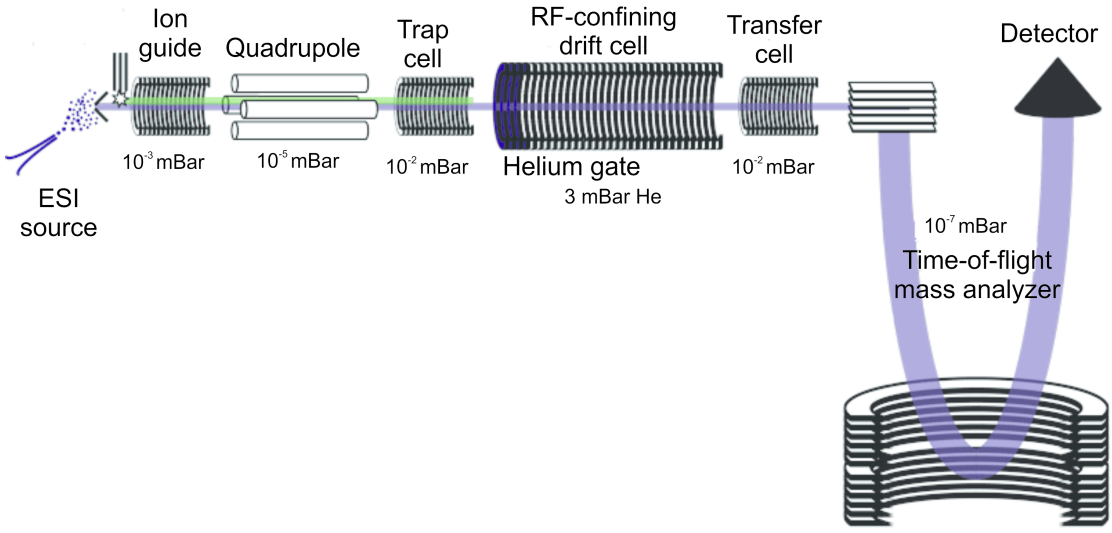

Figure 2.3: General scheme describing the SYNAPT G2 ion mobility mass spectrometer. The scheme is adapted from [59].

the ion source. Larger cone voltages can sometimes induce source fragmentation [44,58].

2.4 Quantum chemical calculations

Density functional theory calculations were performed with the Gaussian 09 suite [60] and Turbomole 6.3 [61]. For the project focused on the investigation of Ni(II)-PhPy complexes, geometry optimizations were done at the B3LYP-D3/def2-SVP level [62–66], which includes version 3 of Grimme's empirical dispersion correction [67]. For all optimized structures, frequency analysis was performed at the same level of theory in order to assign them as genuine minima or transition structures on the potential energy surface (PES), as well as to calculate zero-point vibrational energies (ZPVEs). Subsequently, single-point energy calculations were performed using the M06 functional [68] and the def2-TZVPP basis set [66], where no empirical dispersion is added because the functional itself accounts for dispersion in the vicinity of equilibrium geometries. The energies in the thesis refer to a temperature of 0 K in the gaseous state; singlet−triplet state splittings are adiabatic and include ZPVE. Singlet states were calculated with broken-symmetry [69] open-shell wave functions that were lower in energy than the closed-shell solutions.

In the project focused on carboxylate assisted C-H activation, B3LYP method was used for all calculations. Two different combinations of basis sets were applied. With the acetate counter ion, the cc-pVTZ basis set was used for O, N, C and H and where appropriate

the cc-pVTZ-pp basis set was applied for the metals. With benzoate and 4-nitrobenzoate counter ions, the 6-31G* basis set was used for O, N, C and H and the SDD basis set was applied for Ru, Cu and Pd. All of the structures have been fully optimized and established as genuine minima or transition states on the appropriate potential energy surfaces as confirmed by analysis of the corresponding Hessian matrices. Frequency analysis also enabled calculation of thermochemical corrections and energies are subsequently reported as zero point energies. D2 and D3 versions of Grimme's dispersion [67,70] were also enabled for certain calculations. Corrections for the basis set superposition error were included for dissociations. The theoretical IR spectra were corrected with a scaling factor of 0.985.

The geometries of all optimized structures can be found in the electronic supporting information attached to the current dissertation thesis.

2.5 Infrared multiphoton dissociation spectroscopy

Ion spectroscopy represents yet another dimension for ion structure investigations. The basic principle of such studies lies in the comparison of experimentally obtained infrared or ultraviolet ion spectra with theoretical spectra of different possible isomeric structures of the investigated ion. Therefore the exact structure of the experimentally observed ion can be determined.

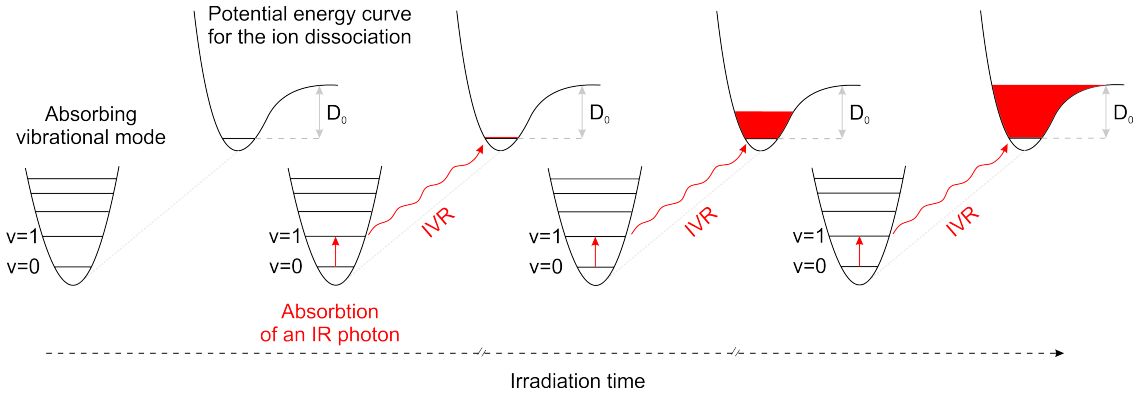

Figure 2.4: Sequential excitation–relaxation cycles during infrared multiphoton dissociation spectroscopy. This figure is adapted from [28].

The spectra discussed in this dissertation were achieved with multiple photon absorption, ion fragmentation is induced by the sequential absorption of several IR photons (Figure 2.4). The method is therefore called infrared multiphoton dissociation spectroscopy (IRMPD). As the experimental spectra are multiphotonic in nature, they do not always

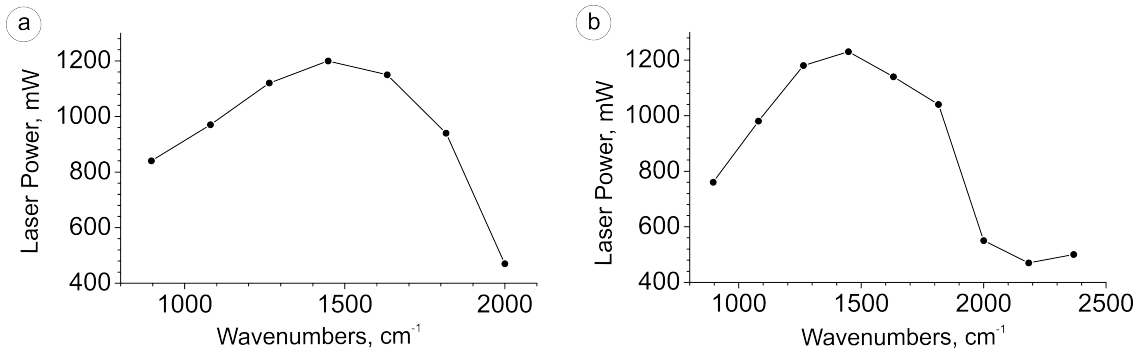

Figure 2.5: Dependence of the free electron laser power on the wavelength during measurement of the IRMPD spectra reported in this thesis shown in a) Figure 3.36a; b) Figure 3.37a and Figure 3.38a

match with the calculated IR spectra [71,72].

Sequential processes of photon absorption are best achieved with free-electron lasers (FELs, on the order of 40MeV). In a FELs an accelerated beam of electrons travels through a periodic magnetic structure (undulator) that forces electrons to oscillate around the axis. This results in emission of light from the electron beam , which is stored in an optical cavity and can again interact with the electrons. This interaction leads to the growth of the intensity of emitted light and to the modulation of its electronic density. Changing the energy of the electron beam and the parameters of the undulator produces a wide range of wavelengths. The IRMPD spectra for this dissertation were obtained at CLIO (Centre Laser Infrarouge Orsay, France), which is operating in the finger-print region (800–1800 cm^{-1}). The experimental signal intensity is affected by laser power. The laser power dependence is shown in Figure 2.5.

2.6 Determination of activation energies

Fragmentation of the mass-selected ions in the Finnigan LCQ IT-MS is induced by resonance excitation processes that are achieved by the application of an AC voltage to the end caps of the trap. This increases the kinetic energy of the ions and induces collisions between the ions stored in the trap and the helium buffer gas. During the collision process, the kinetic energy of the ion can be partially transformed into internal energy which, when large enough, results in ion fragmentation. This process is called collision induced dissociation (CID).

The collision energy needed to induce an optimal amount of fragmentation was shown to be linearly dependent on the m/z of the mass-selected ion (Figure 2.6). In other words,

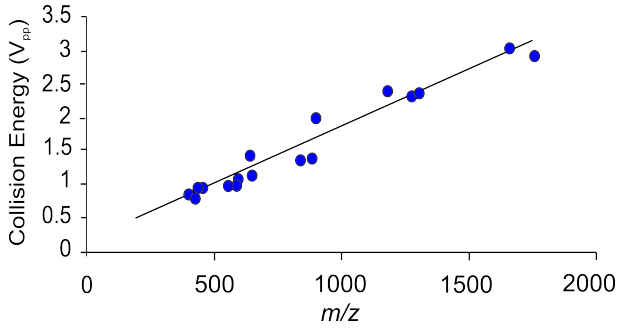

Figure 2.6: *NCE* technology in Finnigan instruments. The figure was adapted from [73].

lighter ions require less energy to induce fragmentation, and heavier ions require more. To compensate for this mass dependency, Finnigan IT mass spectrometers use an approach called normalized collision energy (NCE) thus roughly making it mass-independent. In the *NCE* technology the range of collision energies is given in percentage values and the peak-to-peak voltage is described as $V_{pp} = NCE/30 \cdot (a \cdot \frac{m}{z} + b)$, where a and b are variable parameters [73].

However the use of *NCE*s to determine the appearance energies (AEs) of fragment ions is disadvantageous as it gives little information about real energetic demands for fragmentation. Therefore a calibration method was desired that would transform the manufacturer's *NCE*s into an approximate energy scale. Thus in 2010 the group of Detlef Schröder developed a method that allowed for this conversion [74].

Briefly, a series of benzylpyridinium salts was used as calibrants. A correlation was established between their phenomenological $AE's$ determined with LCQ and the theoretically calculated activation energies. The fragmentation of benzylpyridinium salts is well-studied, both computationally and experimentally [75,76], as they were frequently used as "thermometer ions" for the evaluation of internal energy distributions [77–80]. During CID experiments most of the benzylpyridinium salts fragment with the loss of the neutral pyridine molecule and the formation of a benzylium ion.

The energy dependent CID experiments result in a breakdown curve with a sigmoid shape. Quantitative analysis of this shape allows determination of the appearance energy of the ion. Then, an approach suggested by Bouchoux *et al.* can be used to model experimentally obtained curves [81]. The modeling is performed with sigmoid functions of the type $I_i(E) = a_i/(1 + e^{(E_{1/2,i} - E)b_i})$ using a least-squares criterion. For the parent ion M, the dependence could be rewritten as:

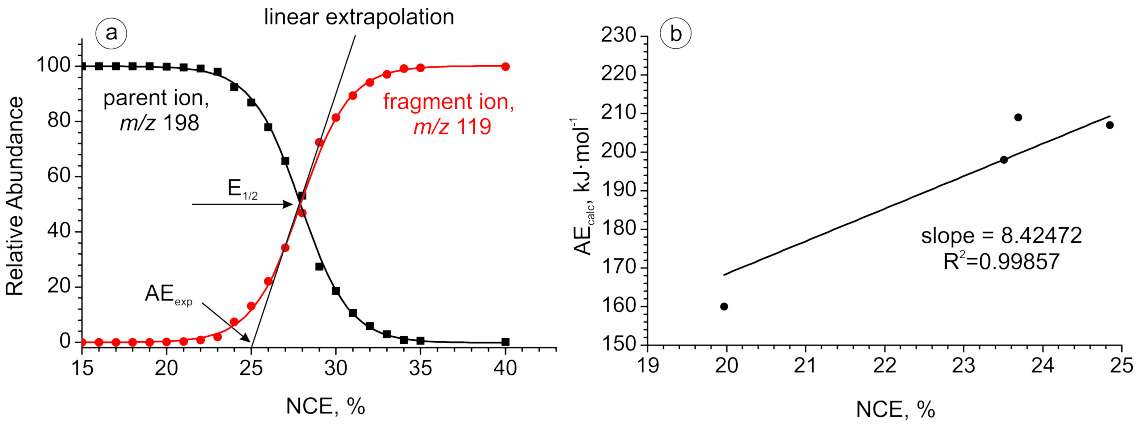

Figure 2.7: a) Breakdown diagram of mass-selected [3,5-dimethylC_6H_3-CH_2-NC_5H_5]$^+$ as a function of the relative collision energy. The dots represent the experimental data; the solid lines - the sigmoid functions used for analysis; b) calibration plot of the characteristic experimental parameters AE_{exp} versus the computed values AE_{calc}. The correlation line is forced to cross the origin.

$$I_M(E) = 1 - [a_i/(1 + e^{(E_{1/2,i}-E)b_i})] \tag{2.1}$$

where a_i stands for the branching ratio of a particular product ion ($\sum a_i = 1$), $E_{1/2}$ is the energy at which the sigmoid function has reached half of its maximum, E is the collision energy and b (in eV^{-1}) describes the rise of the sigmoid curve and thus the phenomenological energy dependence. The phenomenological $AE's$ are then derived from a linear extrapolation of the rise of the sigmoid curve at $E_{1/2}$ to the baseline.

To this end, for all of the CID experiments in this dissertation the following calibration dependence was used. The energy-resolved CID experiments were performed for four benzylbyridinium ions (2,5 dimethyl, 3,5-dimethyl, o-CH_3 and m-OCH_3). The obtained curves were modeled with the above mentioned sigmoid functions and the $AE's$ of the fragment ions were obtained (in NCE, Figure 2.7a). Then the experimental NCE values were plotted against calculated AE values for the corresponding ions (Figure 2.7b). The resulting linear dependence was then used for the conversion of the further obtained $AE's$. Note that the line is forced through the origin.

2.7 Chemicals

2.7.1 Copper acetate speciation

Preparation of copper(II) d^3-acetate monohydrate was done according to the literature [82]. Briefly, $Cu(OH)_2 \cdot CuCO_3$ (that was prepared by precipitation of aqueous $CuSO_4 \cdot 5H_2O$ with Na_2CO_3; 1.125 g; 5.088 mmol) was suspended in 20 mL of water with subsequent dropwise addition of d^4-acetic acid. Then, the reaction mixture was stirred at room temperature for 30 minutes, filtered and precipitated by pouring dropwise into 500 mL of acetone. The resulting blue-green precipitate was collected by filtration, washed with acetone (100 mL) and dried under reduced pressure. Copper(II) d^3-acetate was obtained in 66 % yield (1.380 g).

Copper (II) acetate as well as the solvents were purchased from Sigma-Aldrich and used without further purification.

2.7.2 Investigation of copper catalyzed aerobic cross coupling of thiol esters and arylboronic acids

The general procedure for the coupling of thiol esters with boronic acids was described previously [83].

For on-line monitoring experiments the reaction mixture was prepared by mixing thiol ester (0.0016 g, $4.6 \cdot 10^{-6}$ mol, 1.0 equiv) in a 10 mL vial equipped with a magnetic stirrer bar with a catalytic amount (5 mol %) of copper acetate and 4-tolylboronic acid (0.0014 g, $10.6 \cdot 10^{-6}$ mol, 2.5 equiv). Then, 2 mL of dry dimethylformamide was added, and the mixture was stirred at a certain temperature (40, 50, 60 or 80°C). After a given time from the beginning of the reaction, an aliquot (20 μL) of the reaction solution was taken, dissolved in 2 mL of MeOH, and sprayed into the mass spectrometer. For the experiments in methanol only, all three components were mixed in a 1:1:1 ratio with a concentration of 10^{-3} M. The catalyst and HPLC-grade solvents were purchased from Sigma-Aldrich.

2.7.3 Nickel catalyzed C-H activation of phenylpyridines

2-, 3-, and 4-PhPy as well as the solvents were purchased from Sigma-Aldrich and used without further purification.

2.7.4 Investigation of metal-catalyzed carboxylate assisted C-H activation

All of the chemicals used in the experiments were purchased from Sigma Aldrich and used without further purification.

Chapter 3

Results and discussion

This chapter describes results obtained while working towards the current dissertation thesis. Various metal catalyzed reactions and catalytic complexes were chiefly studied in the gas phase. The primary means of the investigation was ESI-MS which was combined with other research techniques (like IRMPD, DFT calculations and EPR spectroscopy). Catalytic species play a large role in the course of organometallic reactions, therefore, in parallel to monitoring by ESI-MS we investigated the behavior of catalytic complexes in more detail.

3.1 Copper acetate speciation

Copper(II) acetate is a cheap catalyst that is frequently used in organic synthesis. For example, it was found to be a cost efficient alternative to expensive palladium catalysts for some cross-coupling reactions [83]. While in the solid state it is present as a dimer $[Cu_2(OAc)_4(H_2O)_2]$ (also called the "paddle-wheel" structure) [84], in solution the situation is different. In aqueous solutions, due to complete hydrolysis of the salt, the solvatized ions $Cu^{2+}(H_2O)_n$ and $AcO^-(H_2O)_m$ are present [85]. Previous electron and chemical ionization mass spectrometry studies on $Cu(OAc)_2$ behavior in organic solvents showed that $Cu(OAc)_2$ prefers to form aggregates [86].

Therefore, prior to investigation of the mechanisms catalyzed by $Cu(OAc)_2$, we decided to study its ESI-MS behavior in methanol and acetonitrile - frequently used solvents in organic synthesis.

3.1.1 ESI-MS studies

We started with the analysis of a methanolic (10^{-3} M) solution of $Cu(OAc)_2$. The positive as well as negative mode ESI-MS experiments revealed the formation of clusters (Figure 3.1) with highest degree of clusterization noted with the positive ESI-MS.

The suggested peak assignments in Figure 3.1 are supported by the subsequent high-resolution MS measurements (on SYNAPT G2) and the experiments with deuterated copper acetate. Both positive and negative mode spectra in Figure 3.1 show copper trimers to be the most abundant species.

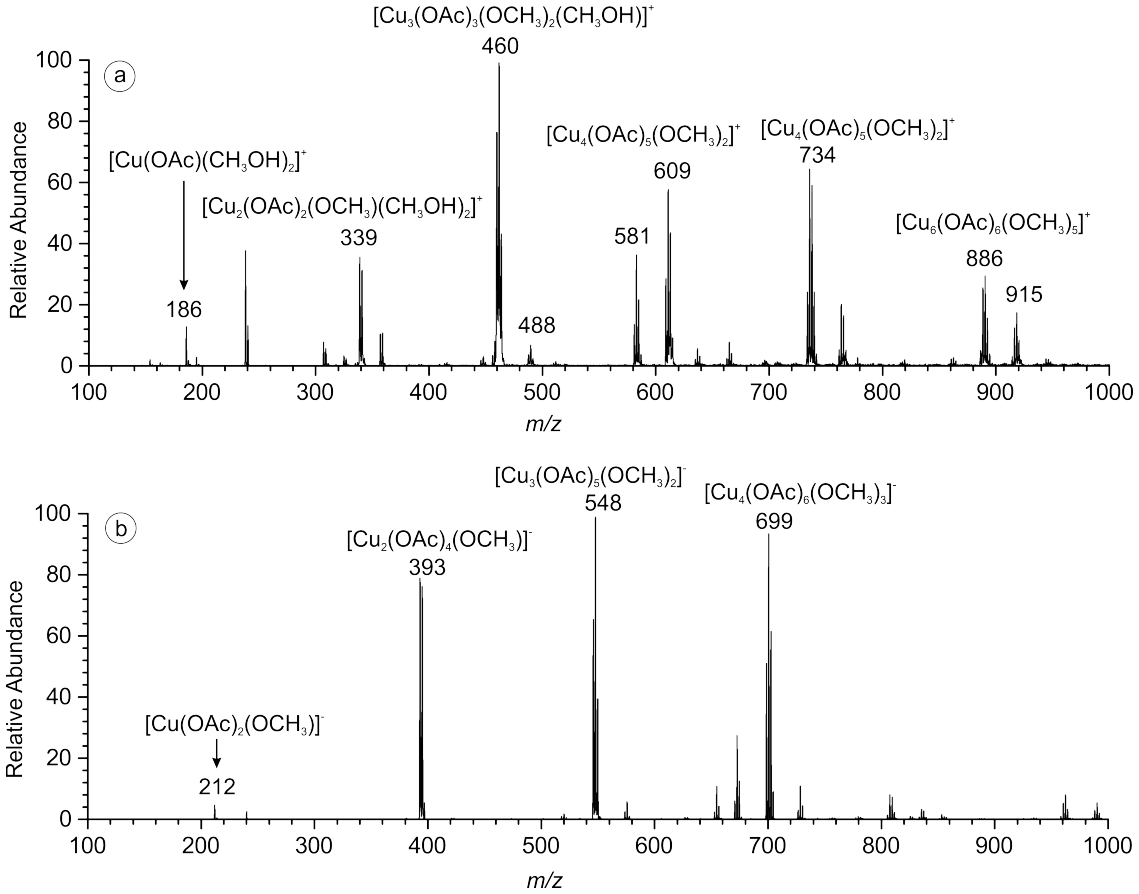

Figure 3.1: ESI mass spectra of a methanolic solution of $Cu(OAc)_2$ (10^{-3} M) in (a) positive-ion mode and (b) negative-ion mode.

The acetonitrile spectrum also demonstrated a significant clustering ability (Figure 3.2). However, in a big contrast to the methanolic solution, we have observed a large abundance of the monomer copper(I) species. Previous ESI-MS studies on copper salts have shown that the appearance of Cu(I) species while spraying Cu(II) solution can happen either due to reduction of Cu(II) already in solution, or within the electrospray course due

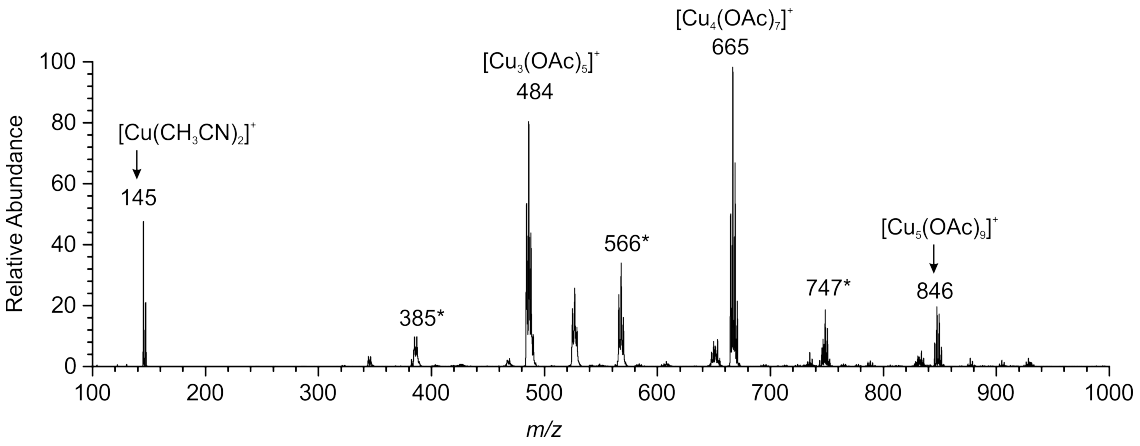

Figure 3.2: Positive-ion ESI mass spectrum of a $Cu(OAc)_2$ solution (2 mM) in acetonitrile. The signals marked with asterisks are due to a sodium contamination of acetonitrile and these correspond to the series sodiated copper(II) acetate clusters, $[Cu_n(OAc)_{2n}Na]^+$.

to the desolvation process [44, 87, 88]. We believe the latter option to be correct in this case. Thus, during the desolvation process a Cu(II) ion of the form $[Cu(OAc)(CH_3CN)_n]^+$ can lose an acetoxy radical to form a Cu(I) species.

In order to better understand the process of cluster formation we have analyzed concentration series (Figure 3.3) for both solvents. Even with the limited number of points, we can clearly see a decrease in the abundance of mononuclear species (although more pronounced in the acetonitrile case) with an increase of concentration. In detail, Figure 3.3a shows that the increasing concentration of salt leads to an increase in the abundances of hexa- and heptanuclear species, whereas the abundance of other multimers slowly decreases. In contrast, the acetonitrile case (Figure 3.3b) does not show an increasing abundance of the largest clusters (n=6).

Next, we have studied cluster degradation processes by CID. Scheme 3.1 shows that two pathways are possible for the fragmentation of copper clusters: degradation or reduction. The question of which of these processes is going to prevail is strongly dependent on the cluster contents and size. Thus, the fragmentation of ions where the number of acetate ligands exceeds the number of methoxy ligands by two or more is dominated by the loss of neutral $Cu(OAc)_2$ (*e.g.* clusters with m/z 1040, and 762). For clusters where the number of acetate ligands is only larger by one, the elimination of $Cu(OAc)_2$ competes with the elimination of $(MeO)_2$ (*e.g.* m/z 609), which is probably formed by the reduction of two Cu(II) centers into Cu(I). The dominance of one of the competing channels depends on the cluster size. For the clusters with $n = 5$ or more, the loss of $Cu(OAc)_2$ prevails, whereas for the smaller clusters only the elimination of $(MeO)_2$ is observed. Therefore, the

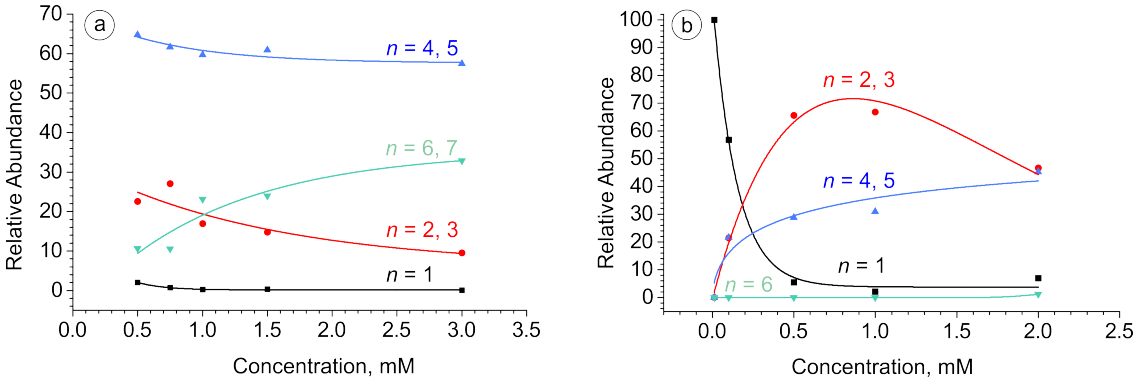

Figure 3.3: a) Normalized abundances ($I_i = 100$) of $[Cu_n(OAc)_{2n-1-m}(CH_3O)_m(CH_3OH)_o]^+$ and b) $[Cu_n(OAc)_{2n-1}(CH_3OH)_o]^+$ cations with various cluster sizes n as a function of the solution concentration in pure a) methanol, b) acetonitrile. For the sake of simplicity, the intensities for groups of clusters were summed.

occurrence of either the reductive or degradation channel depends on the coordination at the copper atoms. The greater the number of acetate ligands (bidentate counterions), the more pronounced is the cluster degradation. The reduction processes are feasible for the smaller clusters with the greater number of monodentate methoxy ligands.

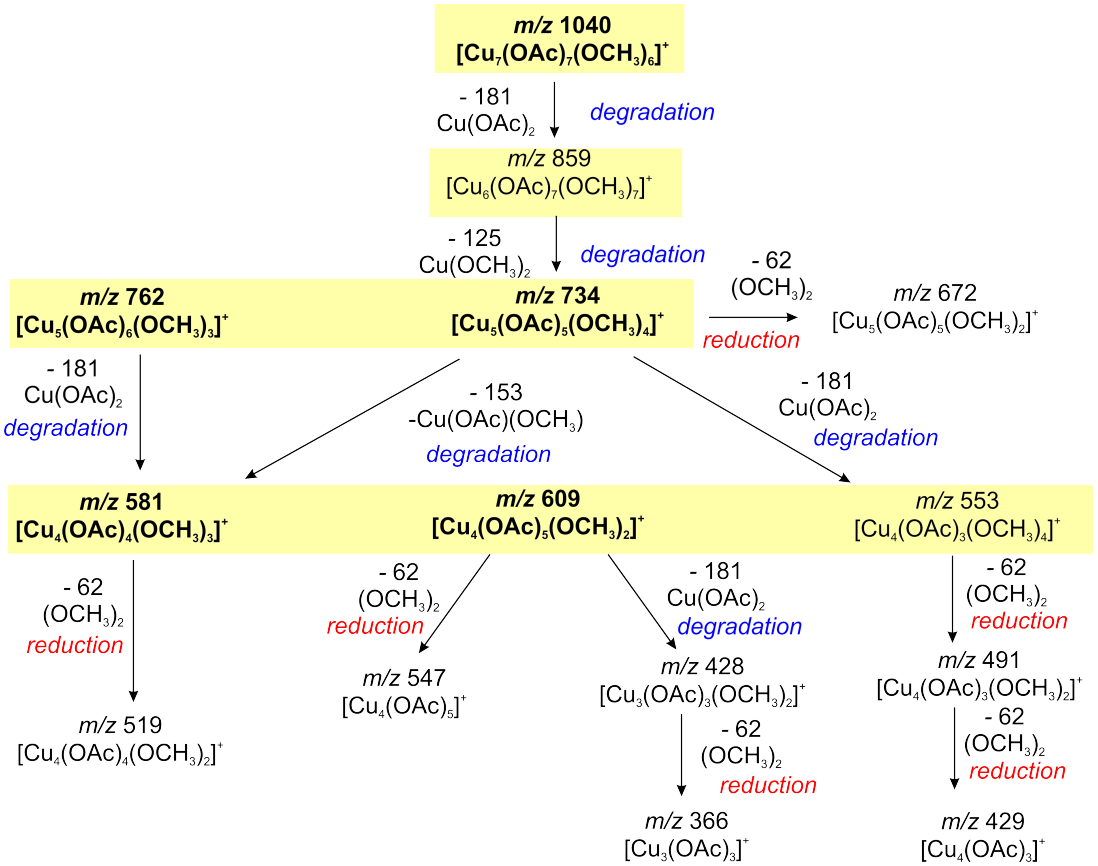

Scheme 3.1: Cluster degradation studied with CID.

During our experiments we have experienced some difficulties with the reproducibility of our results. Later it turned out to be connected with the small amount of moisture present in the inlet system of the mass spectrometer from the previous experiments. To our surprise we have observed that small amounts of water dramatically increased the abundance of the mononuclear clusters, while at the same time, the abundance of larger clusters decreased. We decided to study this water effect in greater detail and the result is shown in Figure 3.4.

Figure 3.4a shows that in a pure methanol solution mononuclear species only correspond to a few percent of the total signal abundance, whereas after the addition of 5 vol. % of water the mononuclear species become the most abundant in the spectrum. A similar, although not as dramatic effect is observed for the acetonitrile solution (Figure 3.4b).

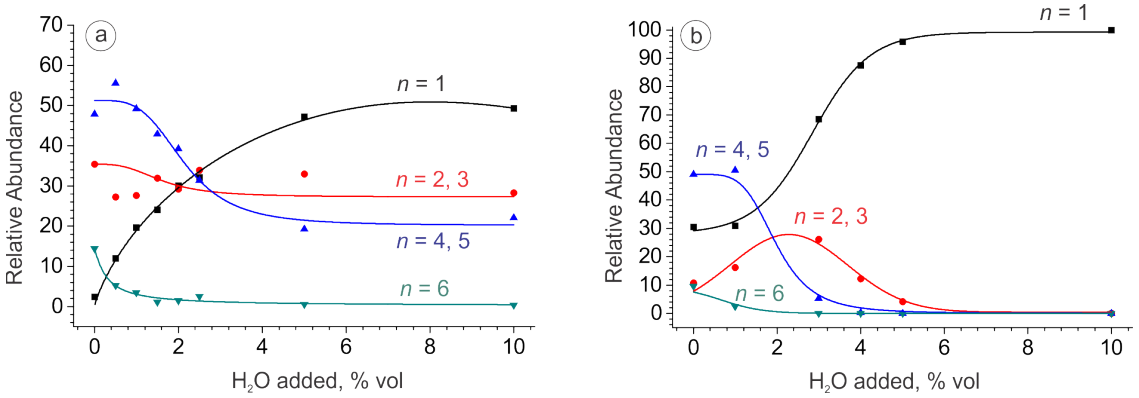

Figure 3.4: a) Normalized abundances ($I_i = 100$) of $[Cu_n(OAc)_{2n-1-m}(CH_3O)_m(CH_3OH)_o]^+$ and b) $[Cu_n(OAc)_{2n-1}(CH_3CN)_o]^+$ cations as a function of the water content in the feed solution of $Cu(OAc)_2$ (1 mM) in a) methanol and b) acetonitrile.

This water effect can have at least two explanations: either cluster breakage happens in solution, or it is an artifact of the ESI-MS process. In order to distinguish between these options we have performed a series of solution-phase experiments.

3.1.2 Solubility determination of $Cu(OAc)_2$ in the methanol-water mixture with different amount of water

The solubility was determined for eleven solutions with different amounts of added water (Table 3.1). For each solvent mixture, the supersaturated solutions of $Cu(OAc)_2$ were prepared. The resulting solutions were filtrated from the excess of copper salt and the solvent evaporated under reduced pressure. The mass of the dry residue was estimated.

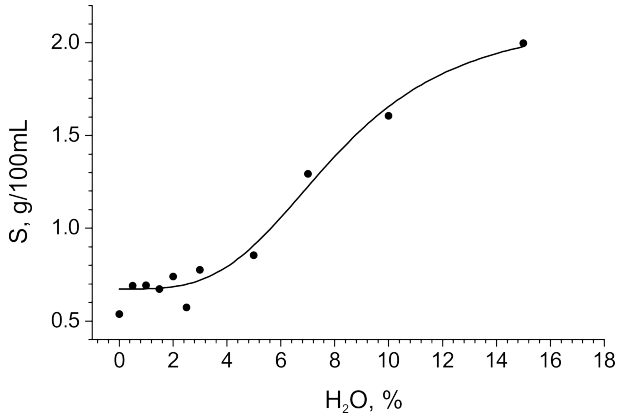

Figure 3.5: Dependence of the determined solubility for each sample on the amount of added H_2O.

As $Cu(OAc)_2$ is hydrophilic, an elemental analysis of the samples (including the $Cu(OAc)_2$ starting material) was carried out, the percentage of absorbed water was determined and taken into account during the solubility calculations. The results are presented in Table 3.1 and Figure 3.5.

Table 3.1: Data for the solubility determination of $Cu(OAc)_2$ in the methanol-water mixture with the different amounts of water.

H_2O, %	$m_{dry\ residue}$, g	formula	$m_{Cu(OAc)_2}$	S, g/(100 mL)
0	0.06	$Cu(OAc)_2 \cdot 0.5\ H_2O$	0.05	0.54
0.5	0.08	$Cu(OAc)_2 \cdot H_2O$	0.07	0.69
1	0.08	$Cu(OAc)_2 \cdot H_2O$	0.07	0.69
1.5	0.04	$Cu(OAc)_2 \cdot H_2O$	0.03	0.67
2	0.04	$Cu(OAc)_2 \cdot H_2O$	0.04	0.74
2.5	0.03	$Cu(OAc)_2 \cdot H_2O$	0.03	0.57
3	0.04	$Cu(OAc)_2 \cdot H_2O$	0.04	0.78
5	0.05	$Cu(OAc)_2 \cdot H_2O$	0.04	0.86
7	0.07	$Cu(OAc)_2 \cdot H_2O$	0.07	1.29
10	0.09	$Cu(OAc)_2 \cdot H_2O$	0.08	1.61
15	0.10	$Cu(OAc)_2 \cdot H_2O$	0.10	2.00

It can be seen that solubility of $Cu(OAc)_2$ in methanol increases with increasing amounts of water, added to the solution.

3.1.3 EPR measurements

Additional EPR measurements were performed to complement our solubility studies. Figure 3.6 shows that the pure methanol solution of copper (II) acetate is almost EPR inactive,

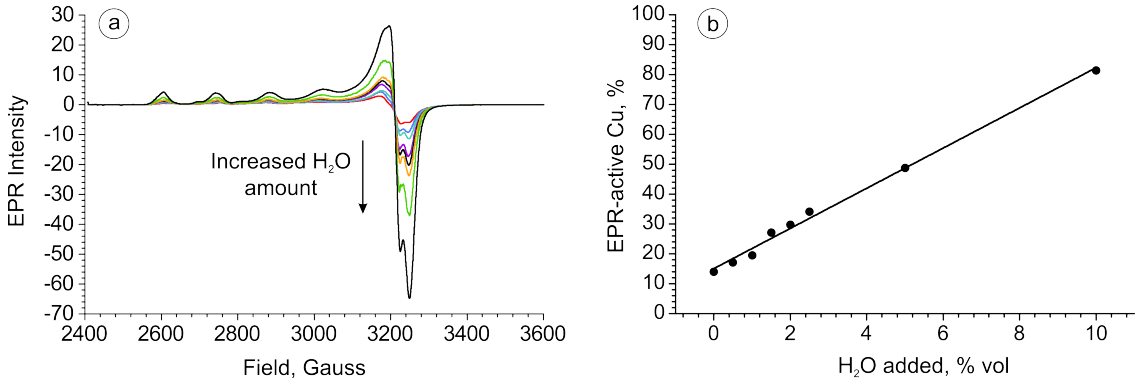

Figure 3.6: a) EPR spectra of $Cu(OAc)_2$ solutions, 3.75 mM in methanol with variable water content. b) Fraction of EPR-active Cu(II) species in $Cu(OAc)_2$ solutions in methanol with variable water content, obtained *via* double integration of spectra relative to an external standard.

producing a small EPR signal. However, addition of water increases the signal, with the EPR parameters (A and g) remaining unchanged. This suggests that the signal growth corresponds to the concentration increase of monomers in the solution. The dependence of EPR signal growth on the amount of water is linear (Figure 3.6b) and shows that at 10% of added water 80% of copper acetate became EPR active. These observations suggest that the mononuclear species are formed after the addition of water. We also assume that, similar to the solid paddle-wheel dimer, high order $[Cu(OAc)_2]_n$ species exhibit antiferromagnetic properties when n is even, or produce a small EPR signal when n is odd. Therefore, these results support the hypothesis of water leading to cluster breakage in solution.

When directly comparing the EPR and ESI dependencies, we can see that they do not agree quantitatively. This is easily explained as ESI does not accurately sample concentration in the solution. Thus, while obvious correlation exists between ESI mass spectra and solution properties, the match is not 1:1. We suggest that during the ESI process, methanol is preferentially evaporated from the droplets, (due to its lower boiling point) and the water concentration in the droplets increases. Thus, ESI-MS experiments reflect a somewhat larger water content than the one in the solution.

In general, the results show that the addition of small quantities of water significantly influences the speciation of copper (II) acetate in organic solvents. The speciation is shifted towards the formation of monomers, suppressing the formation of larger clusters. We believe that this finding is important for future mechanistic studies of various copper(II) acetate catalyzed reactions.

3.2 Investigation of copper catalyzed aerobic cross coupling of thiol esters and arylboronic acids

In 2007 Villalobos *et al.* found a convenient method for the synthesis of non-symmetrical ketones (Scheme 3.2a) [83]. The reaction is a modification of the Liebeskind–Šrogl coupling reaction [89]. All of the previous synthetic procedures based on the cross-coupling of thioorganic compounds and boronic acids required the presence of a palladium catalyst and a stoichiometric amount of a Cu(I) salt [90–96]. However, the procedure suggested by Villalobos *et al.* only uses a copper catalyst, which makes the reaction much more financially appealing (Scheme 3.2a). The authors reasoning behind the procedure's design was that the second equivalent of boronic acid, added to the reaction mixture, would recover the copper catalyst from the Cu-SR intermediate, and therefore a second catalytic species would not be needed for the reaction to proceed. This was indeed the case, however a concrete mechanism of the reaction was not clear: the authors suggested several possible pathways, including transmetallation, ligand exchange, or the involvement of oxidated copper clusters [97].

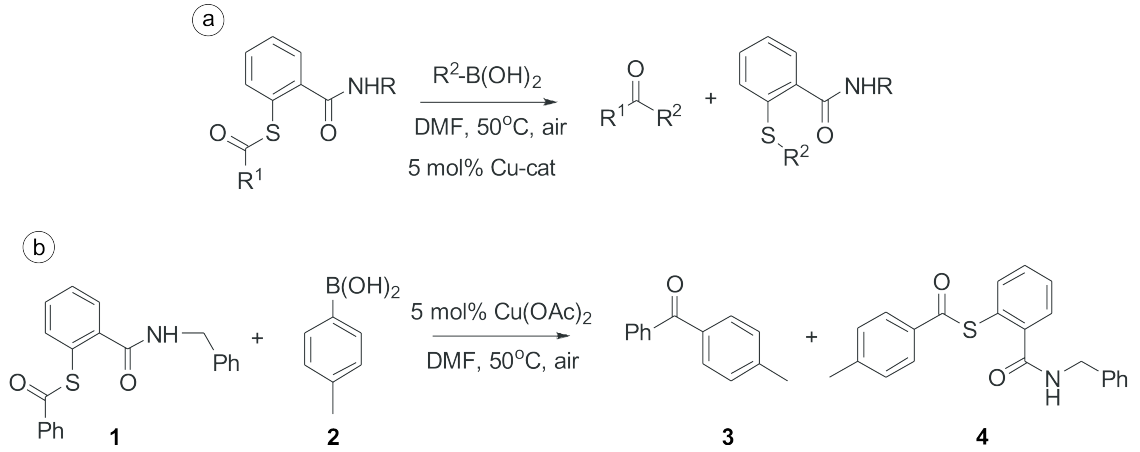

Scheme 3.2: a) Aerobic coupling of thiol esters and boronic acids and b) specific reaction investigated here.

Therefore we decided to investigate the mechanism using ESI-MS and tandem mass spectrometry, for the particular reaction described in Scheme 3.2b. We began with the off-line monitoring, investigating the reaction mixture in steps, starting from less complicated systems. Subsequent addition of the reagents and comparison of the spectra obtained for different mixtures allowed easier identification of reaction intermediates.

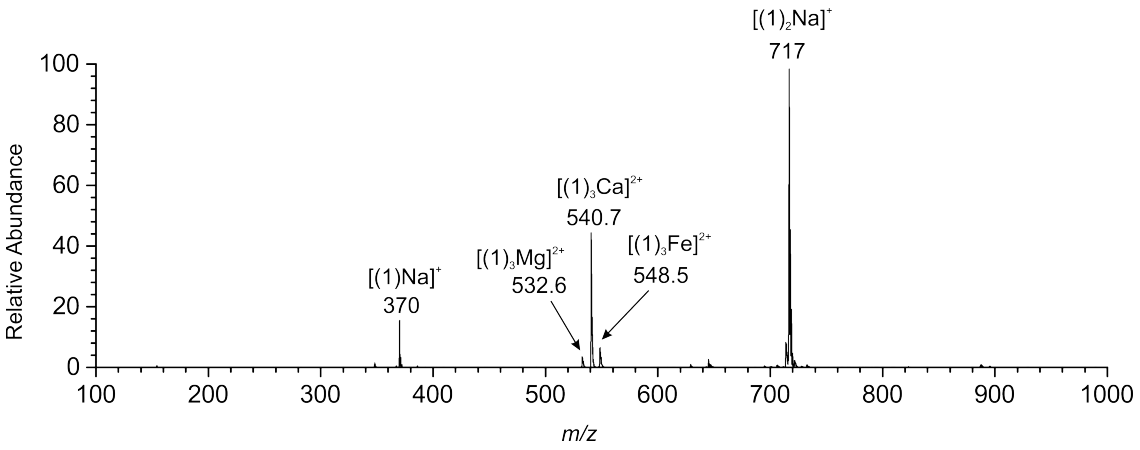

Figure 3.7: Positive mode ESI-MS of the solution of thiol ester (1) in methanol recorded under mild ionization conditions.

3.2.1 Off-line monitoring *via* ESI-MS

Accordingly, we investigated the behavior of thiol ester **1** solution in methanol with ESI. The positive mass spectrum (Figure 3.7) shows a large abundance of singly charged sodiated complexes (m/z 370 and 717), and also signals of doubly charged magnesium, calcium and iron complexes (m/z 540.7, 532.6, 548.5 respectively).

Next, we studied the behavior of 4-tolyl boronic acid in methanol. Negative ESI mass spectrum of the boronic acid solution shows the formation of 4-tolylbronic esters at m/z 149, 195 and 385 (Figure 3.8). Possible mechanisms for the ester anions formation are shown in Scheme 3.3. We have also observed the [4-TolO]$^-$ anion at m/z 107, which could be formed upon deborylation of an ester. Similar observations were reported by Wang *et al.* [98] in their detailed study of the ESI-MS behavior of different boronic acids. They have also accounted for the deborylation mechanism leading to the formation of [4-TolO]$^-$ anions. As the peaks at m/z 221 and 299 do not correspond to the isotope pattern associated with the boron atom, we consider them to be the result of impurities.

The mixture of 4-tolylboronic acid with $Cu(OAc)_2$ in methanol was also investigated. Neither positive nor negative ESI mass spectra show the formation of any species containing both boron and copper atoms. Most likely, we don't see them under these conditions as boronic acid rapidly undergoes reaction with methanol leading to *p*-methylanisol as is shown for the case of boronic esters (Scheme 3.4) [99].

Next we analyzed the mixture of thiol ester with $Cu(OAc)_2$. The spectrum in Figure 3.9a shows the formation of the complexes with both copper(I) and copper(II) species with the starting thiol ester **1** at m/z 410, 469 and 757. CID analysis of the complex at m/z

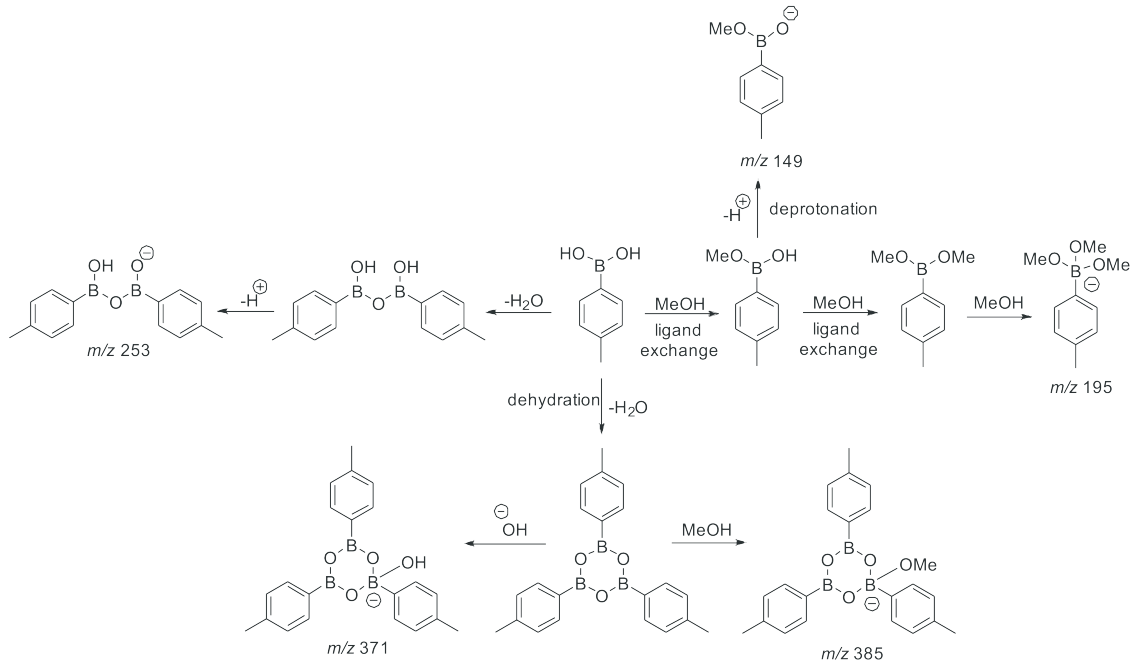

Scheme 3.3: The proposed formation mechanisms for some of the observed ions present in the negative ESI-MS of the boronic acid solution.

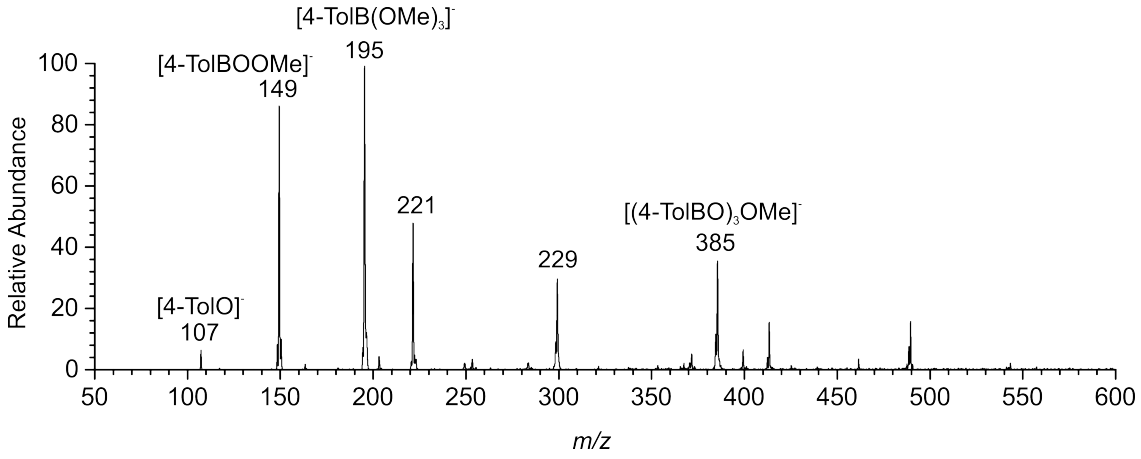

Figure 3.8: Negative mode ESI-MS of 4-tolylboronic acid in methanol.

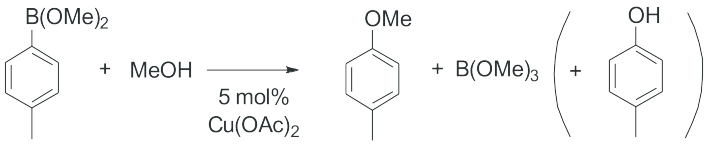

Scheme 3.4: Cu-catalyzed methoxylation of tolylboronic ester.

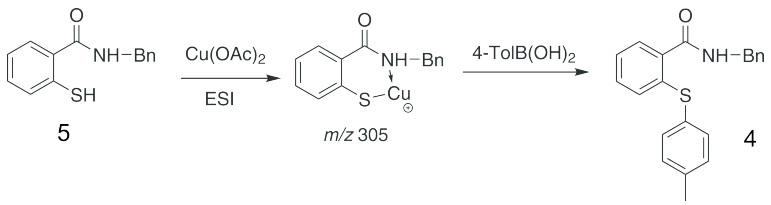

Scheme 3.5: Proposed reactivity scheme of thiol **5** with tolylboronic acid investigated here.

469 (Figure 3.10) showed the elimination of a mixed anhydride of benzoic and acetic acid (*e.g.* Ph-CO-O-CO-CH_3). The fragment ion at m/z 305 (assigned as $[(\text{int})\text{Cu}]^+$) was also observed in the source spectrum (see Figure 3.9). We found that the appearance energy for $[(\text{int})\text{Cu}]^+$ corresponds to 121 ± 3 kJ·mol^{-1}. The structure of the ion at m/z 305 was checked in MS^n experiments. MS^2 spectra of m/z 305 from the source spectrum were compared with MS^3 spectra of the fragment m/z 305 by activation of m/z 469. The spectra appeared to be identical. Also, the most pronounced fragmentation channel of m/z 305 is the elimination of a CO molecule . Therefore we suggest that the intermediate has a cyclic structure as shown in Figure 3.10.

Next we have analyzed the mixture of all the reaction components (thiol ester **1**, boronic acid and copper catalyst) in methanol. In addition to the previously observed complexes with Cu(I/II) and the starting thiol **1** Figure 3.9b shows the formation of the complexes of the product **4** with Cu(I/II) and sodiated complexes of **4**.

Although the signals containing product **4** were observed in the recorded spectra, we have not observed any complexes of ketone **3** in the mixture. Although ketone complexes are usually easily detectable with ESI-MS we suppose that their absence can be explained by the presence of the better ligand **4**.

3.2.2 Experiments with thiol 5

In order to test the rationality as to whether the intermediate complex $[(\text{int})\text{Cu}]^+$ is participating in the reaction mechanism (possible pathway shown in Scheme 3.5), we have carried out experiments with thiol **5** in order to simulate the conditions for the formation of the complex at m/z 305.

Figure 3.11a shows the positive ESI mass spectrum obtained for the mixture of thiol **5** and copper acetate (1:1) in methanol. Although we have not observed the formation of the desired intermediate, we have detected the ion with m/z 304 which can be associated with the oxidated thiol-Cu complex. Nevertheless, the spectrum of the mixture of all three

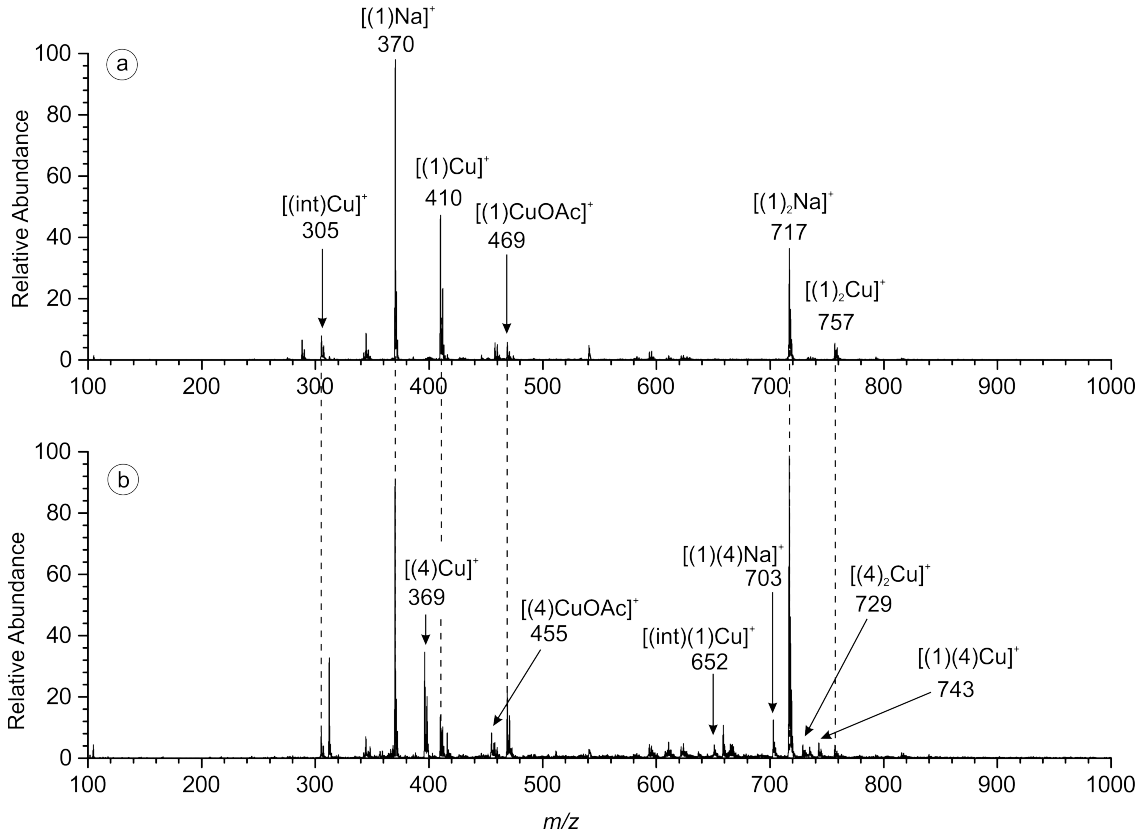

Figure 3.9: Positive mode ESI mass spectra of a) the mixture of thiol ester **1** and $Cu(OAc)_2$ in methanol; b) the mixture of thiol ester **1**, 4-tolylboronic acid and $Cu(OAc)_2$ in methanol, taken at room temperature and after 1h after mixing the reagents.

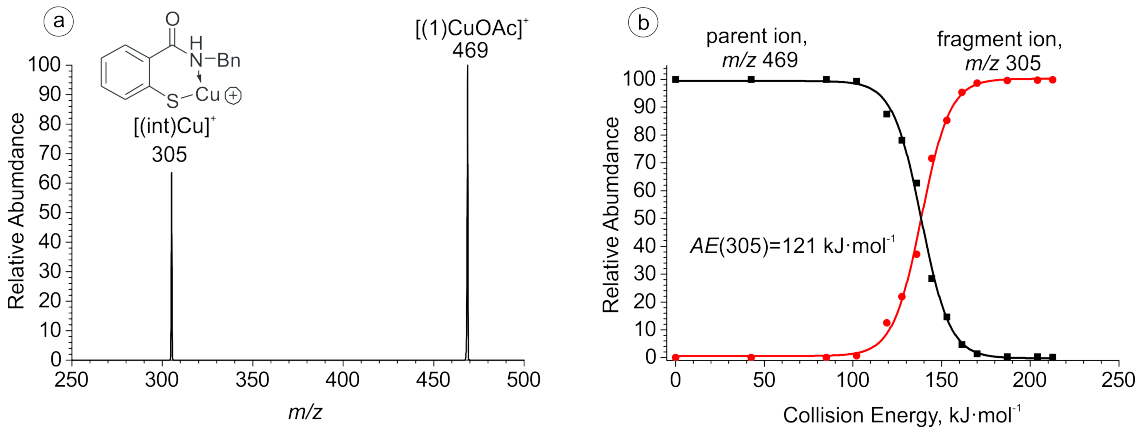

Figure 3.10: a) CID spectrum of the mass-selected m/z 469 and b) its breakdown curve.

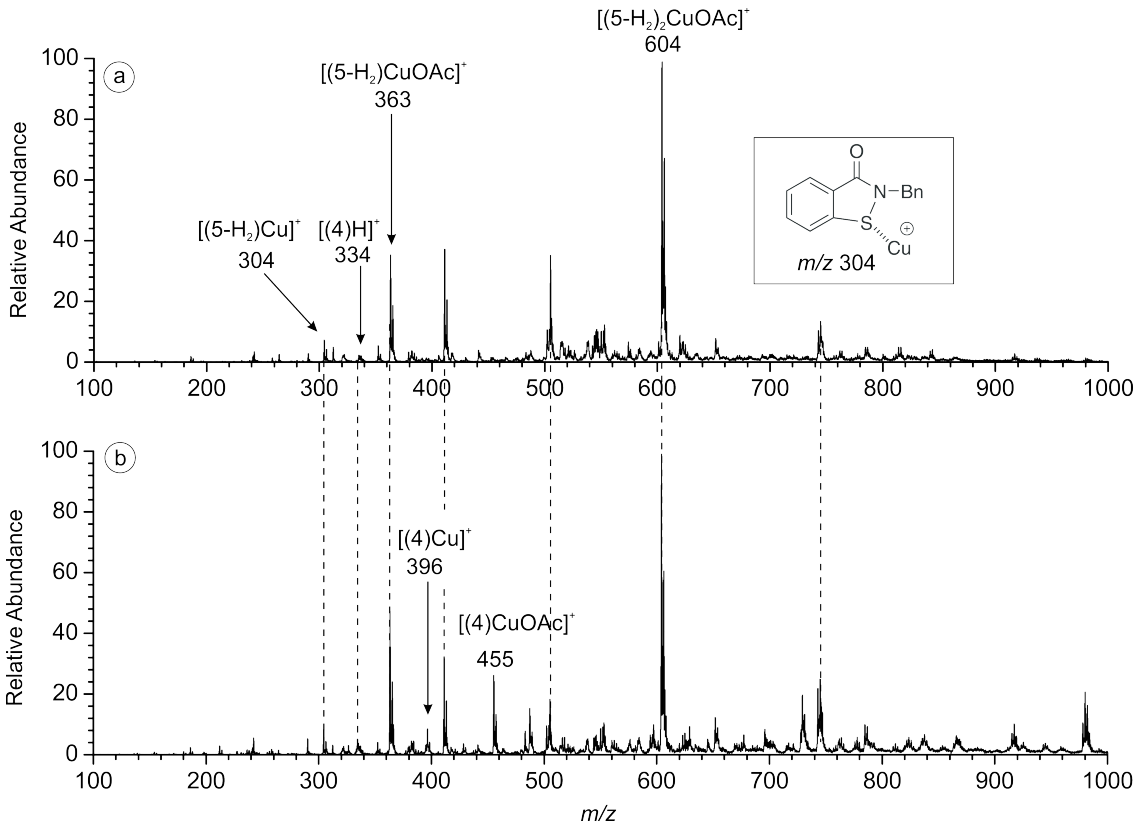

Figure 3.11: Positive mode ESI mass spectra of a) the mixture of thiol **5** and $Cu(OAc)_2$ in MeOH and b) the mixture of thiol **5**, 4-tolylboronic acid and $Cu(OAc)_2$ in MeOH.

components (thiol **5**, 4-tolylboronic acid and $Cu(OAc)_2$, Figure 3.11b) shows that product **4** is formed. Therefore we believe that the complex at m/z 305 is not formed during the course of the reaction and rather is produced during the ESI process.

3.2.3 On-line monitoring and kinetic studies

We next performed on-line monitoring of the reaction mixture under identical conditions as was used for synthesis (*e.g* 5 mol % of $Cu(OAc)_2$, 1 eq. of thiol ester **1**, 2.5 eq. of 4-tolylboronic acid, DMF). Monitoring was performed by repetitive sampling of portions of the reaction mixture at given time intervals. The small portions of the reaction mixture (*e.g.* 10 μL) were diluted in MeOH (2 mL) and the resulting solutions sprayed into the mass spectrometer. Table 3.2 shows the intensity changes for the most abundant ions in the spectrum over time. The product complex could already be detected 15 minutes after the beginning of the reaction. Due to the small amounts of copper catalyst in the reaction mixture and the dominance of sodiated complexes, the detection of Cu complexes was very limited.

Table 3.2: Relative intensities of the major complexes observed in the reaction mixture performed in DMF at 50°C.

Time, h	m/z 356	m/z 370	m/z 396	m/z 689	m/z 703	m/z 717
0.3	0.3	19.6	0.0	0.6	10.5	69.0
0.5	0.6	14.3	0.4	1.4	13.1	70.2
1.0	0.7	10.3	0.3	2.6	21.4	64.7
2.0	0.9	7.9	0.4	7.8	31.3	51.7
3.3	1.7	7.7	1.1	11.3	38.2	40.0
5.3	2.0	5.0	0.0	21.2	43.9	27.9
6.7	3.3	5.7	0.0	26.6	42.3	22.1
8.2	3.7	5.6	0.0	32.2	42.0	16.5
23.0	4.7	0.7	0.0	71.9	20.8	1.9

Table 3.3: Data obtained from linearization.

t, °C	T, K	1/T, K^{-1}	k, $L \cdot mol^{-1} \cdot s^{-1} \cdot 10^5$	ln(k)
40	313.15	0.0032	0.85	-11.39
50	323.15	0.0031	1.81	-9.40
60	333.15	0.0030	8.04	-9.02
80	353.15	0.0028	27.80	-8.23

On-line monitoring performed at different temperatures (40, 50, 60 and 80°C) resulted in the creation of kinetic curves (see Figure 3.12). Treating the reaction as pseudo first order gives the linear dependencies shown in Figure 3.13, and the rate constant can be determined from the slope of the resulting lines. Linearization of the kinetic curves shown in Figure 3.12 was done with the equation 3.1. The final data obtained upon linearization are presented in Table 3.4. It can be seen that increasing the temperature of the reaction increases its rate. The temperature dependency of the rate constants can be further investigated using the Arrhenius and Eyring equations (3.2, 3.3) for the determination of thermodynamic parameters of the reaction. Analysis of the Arrhenius equation gave us $E_a = 81 \pm 5$ $kJ \cdot mol^{-1}$. The Eyring equation gave an activation enthalpy of 76 ± 5 $kJ \cdot mol^{-1}$, and an activation entropy -100 ± 5 $J \cdot mol^{-1} \cdot K^{-1}$. The Gibbs energy according to equation 3.4 was found to be 103 ± 5 $kJ \cdot mol^{-1}$ at 298 K.

$$\frac{dI}{dt} = k(T) \cdot [1]^n \cdot [2]^m \tag{3.1}$$

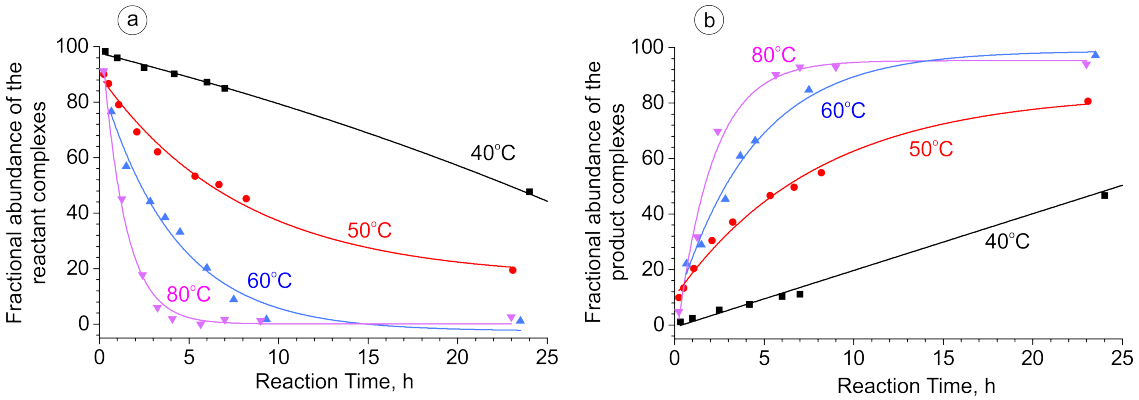

Figure 3.12: Dependence of the abundances of (a) reagent and (b) product complexes on the reaction time at different temperatures.

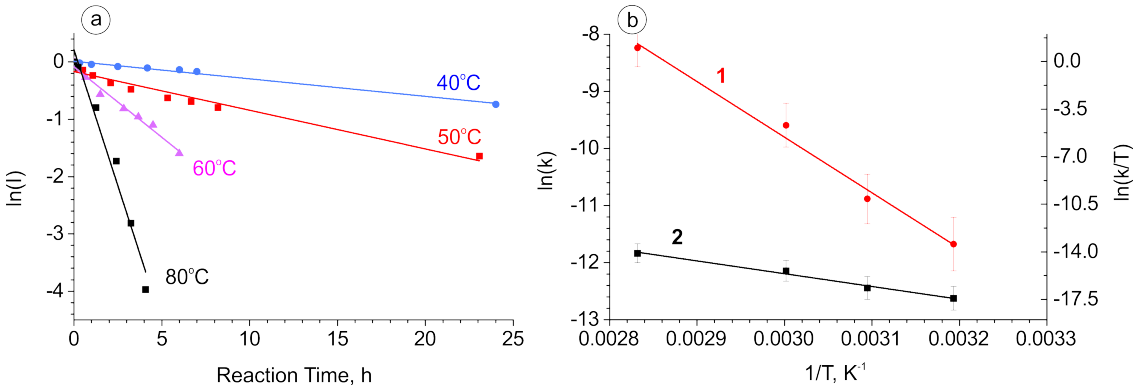

Figure 3.13: (a) Logarithmic plot of the abundance of reactant complexes in dependence of the reaction time at different temperatures; (b) Arrhenius (1) and Eyring (2) plots for thiol ester **1** coupling with 4-tolylboronic acid. The resulting values were determined from two independent measurements (I represents the sum of the abundances of $[(\mathbf{1})\mathrm{Na}]^+$, $[(\mathbf{1})(\mathbf{4})\mathrm{Na}]^+$, and $[(\mathbf{1})(\mathbf{2})\mathrm{Na}]^+$ divided by the sum of the abundances of all complexes in Table 3.2).

$$ln(k) = -\frac{E_a}{R} \cdot \frac{1}{T} + ln(A) \tag{3.2}$$

$$ln\frac{k}{T} = \frac{-\triangle H^{\ddagger}}{R} \cdot \frac{1}{T} + ln\frac{k_B}{h} + \frac{\triangle S^{\ddagger}}{R} \tag{3.3}$$

$$\triangle G^{\ddagger}(T) = \triangle H^{\ddagger} - \frac{T \cdot \triangle S^{\ddagger}}{1000} \tag{3.4}$$

In conclusion, although ESI-MS experiments did not resolve the mechanism of the investigated reaction, we profited from the formation of highly abundant sodiated complexes. These species allowed us to follow the kinetics of the investigated reaction. The kinetic

experiments enabled determination of the rate constants and thermodynamic parameters.

3.3 Nickel catalyzed C-H activation of phenylpyridines

Pyridine derivatives are a common class ligands in organometallic chemistry. Thus, phenylpyridine (PhPy) isomers, especially 2-phenylpyridine, are frequently used in the mechanistic studies of metal-catalyzed C-H activation [100–102]. It was shown that a metal catalyst can coordinate to the nitrogen atom of 2-phenylpyridine and facilitate activation of the C-H bond in the position 2' of the phenyl ring.

In order to account for other regioisomers, we have theoretically compared the bond dissociation energies of the phenyl- C-H bonds of 2- 3- and 4-PhPy (Scheme 3.6). It can be seen that the C-H bond in the 2' position of 2-PhPy is only by a small extent weaker than those in the 3- and 4- regioisomers. Therefore, it cannot be considered "pre-activated" in the 2-PhPy molecule. However, once the metal is coordinated to the nitrogen atom, the metal is in close proximity to the 2' position of the phenyl ring, making the C-H bond in this position easily activated.

In this project we decided to investigate mixtures of 2,- 3- and 4-phenylpyridines ($3 \cdot 10^{-4}$ M) with nickel(II) chloride (10^{-4} M) in methanol/water (1:1) by means of ESI-MS, IMS and tandem mass spectrometry.

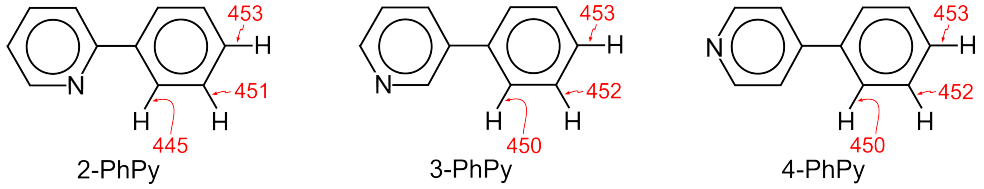

Scheme 3.6: Computed C−H bond dissociation energies (M06/def2-TZVPP//B3LYP-D3/def2-SVP, in kJ·mol^{-1} at 0 K) of the phenyl substituent in 2-PhPy, 3-PhPy and 4-PhPy.

3.3.1 ESI-MS studies

Positive ESI mass spectra revealed the formation of two types of nickel complex: dications $[Ni(PhPy)_n]^{2+}$ and monocations $[Ni(PhPy)_m]^{+}$, where n and m are dependent on the electrospray conditions [44,58,103,104]. A typical mass spectrum obtained for such a solution is shown in Figure 3.14.

For all of the investigated phenylpyridines, the major signal observed at m/z 156 corresponds to the protonated phenylpyridine ($[PhPyH]^{+}$). For clarity, further discussion is

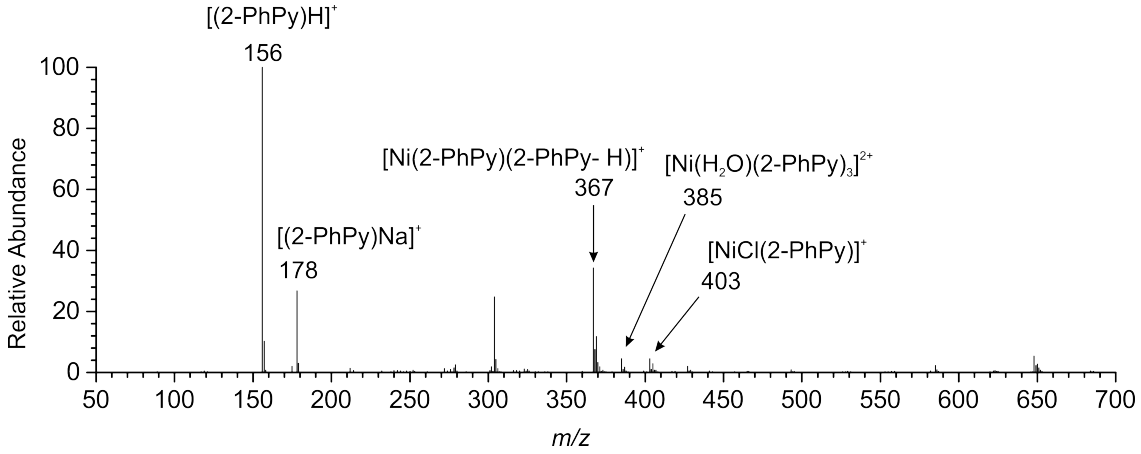

Figure 3.14: Positive ESI-MS of the solution of $NiCl_2$ and 2-PhPy in $MeOH/H_2O$ recorded with a cone voltage U_C= 10 V.

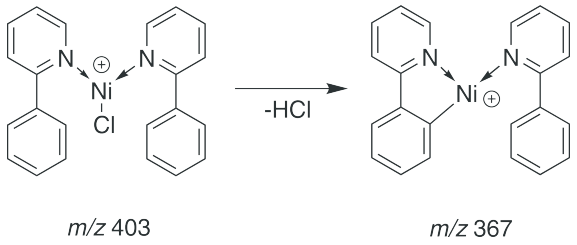

Scheme 3.7: C-H activation reaction we study here.

focused on the spectra recorded within the range 200 - 700 m/z. When this is taken into account, the major signal for the 2-PhPy solution appears at m/z 367 ($[Ni(2\text{-}PhPy)_2\text{-}H]^+$, Table 3.4). On the other hand, this activated complex is absent in the case of both 3- and 4-PhPy solutions. These observations suggest a strong preference for the C-H activation of 2-PhPy. For 3- and 4-PhPy a dication at m/z 339 is the most abundant ion, whereas it is hardly seen in the case of 2-PhPy due to large steric demands.

Table 3.4: Relative intensities of the major nickel complexes in the ESI mass spectra of $NiCl_2$- PhPy solutions with the isomeric PhPy's ($\sim 3\times10^{-4}$ M) in water/methanol (1:1) under soft ionization conditions in the ESI source. The column $[Ni(PhPy)_3]^{2+}$ includes a signal for $[Ni(H_2O)(PhPy)_3]^{2+}$, which is formed by association of the $[Ni(PhPy)_3]^{2+}$ dication with water.

	$[Ni(PhPy)_3]^{2+}$	$[Ni(PhPy)_4]^{2+}$	$[Ni(PhPy)_2\text{- H}]^+$	$[Ni(PhPy)_2]^+$	$[Ni(PhPy)_3]^+$
2-PhPy	2	<1	100	30	2
3-PhPy	2	100	<0.1	<1	6
4-PhPy	12	100	<0.1	3	10

As is implied in Scheme 3.7, the ion at m/z 403 might be the precursor for the activated complex $[Ni(2\text{-}PhPy)_2\text{-}H]^+$. In order to test this possibility we have isolated the

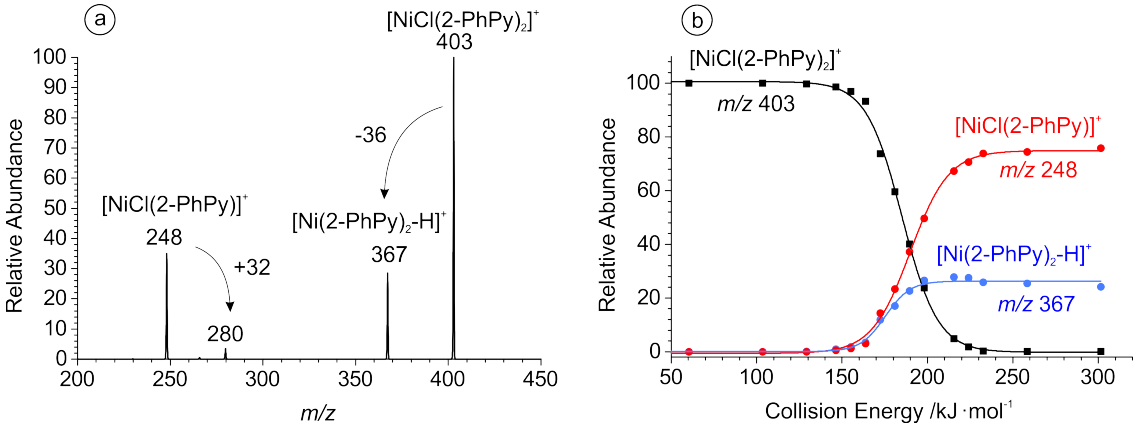

Figure 3.15: a) CID spectrum of the mass-selected $[NiCl(2\text{-}PhPy)_2]^+$ (m/z = 403) leading to two fragmentation channels: the loss of HCl (product ion with m/z = 367) and 2-PhPy (product ion with m/z = 248); b) its breakdown curve.

Table 3.5: Fragment ions appearance energies (in kJ·mol^{-1}) and relative fragment intensities upon CID of mass-selected m/z 403 and m/z 332.

	$[Ni(PhPy)_2]^+$		$[NiCl(PhPy)(D_5\text{-}Py)]^+$			
	-HCl	-PhPy	-HCl	-DCl	-(D_5-Py)	-PhPy
2-PhPy	160 (27%)	170 (73%)	160 (6%)	-	160 (94%)	-
3-PhPy	215 (13%)	215 (87%)	200 (4%)	205 (1%)	205 (91%)	205 (4%)
4-PhPy	220 (5%)	230 (95%)	200 (1%)	215 (<1%)	205 (98%)	215 (1%)

corresponding ion in the collision cell and subjected it to the CID experiments. Figure 3.15 shows that two fragmentation channels are present for the ion at m/z 403: either elimination of HCl (which corresponds to collision induced C-H activation) or elimination of the neutral 2-PhPy ligand. We experimentally found that the HCl elimination channel, although being the minor one, requires 160 ± 5 kJ·mol^{-1} of energy, whereas the elimination of 2-PhPy needs about 10 kJ·mol^{-1} more.

By comparison with those for the other regioisomeric complexes, the AE's of both losses are significantly lower in energy for the case of 2-PhPy, consistent with the observations described in Table 3.4. The smaller ligand binding energy for the 2-PhPy complex is associated with bigger steric hindrance and thus with more facile C-H activation channel.

Likewise, mixed complexes of the form $[NiCl(PhPy)(D_5\text{-}Py)]^+$were generated in the gas phase and their CID behavior was compared to that of the $[Ni(PhPy)_2]^+$ complexes. In all of the mixed complexes the elimination of the perdeuterated pyridine ligand prevails. However the ligand loss AE's are again the smallest in case of 2-PhPy complexes. The PhPy ligand is bigger than Py, thus elimination of PhPy occur in only small amounts.

Table 3.6: Arrival times (in ms) of the ions generated upon ESI of various $NiCl_2$ - PhPy solutions, [a]the species did not survive mobility sampling.

	m/z	2-PhPy	3-PhPy	4-PhPy
$[NiCl(PhPy)]^+$	248	2.98	3.80	3.80
$[NiCl(PhPy)_2\text{-}H]^+$	367	4.83	5.32	5.97
$[NiCl(PhPy)_2]^+$	403	4.94	6.08	6.35
$[NiCl(PhPy)_3]^+$	558	*a*	8.90	9.77
$[Ni(PhPy)_3]^{2+}$	261.5	*a*	3.09	3.20
$[Ni(PhPy)_4]^{2+}$	339	*a*	3.74	4.07

C-H bond activation, on the other hand, is largely suppressed for the mixed pyridinium complexes, which suggests that the barrier associated with the formation of HCl is close to the binding energy of D_5-Py. Furthermore, for the mixed complexes, significant amounts of DCl elimination are observed. While in the case of 2-PhPy we selectively observe HCl elimination, the corresponding loss for 3- and 4-PhPy complexes is consistent with larger thresholds for these channels.

3.3.2 Ion mobility studies

In the next step, we studied the above mentioned ions by ion mobility mass spectrometry. Initially, we were interested whether the mobilities of isomeric Ni- complexes would be different. An example of a typical mobilogram obtained for the ion at m/z 403 from the 1:1 mixture of 2- and 3-PhPy is shown in Figure 3.16a. At low cone voltage (U_C= 20 V) all three features (*e.g.* $[NiCl(2\text{-}PhPy)_2]^+$, $[NiCl(2\text{-}PhPy)(3\text{-}PhPy)]^+$, and $[NiCl(3\text{-}PhPy)_2]^+$) are detectable and observed in an approximately 1:2:1 ratio. This is expected from the 1:1 concentration ratio of the isomers. When the cone voltage is increased, $[NiCl(2\text{-}PhPy)_2]^+$ starts to disappear first, followed by the depletion of the mixed $[NiCl(2\text{-}PhPy)(3\text{-}PhPy)]^+$ ion. This observation is in agreement with the predicted steric effects in the complexes: in the case of 2-PhPy the energy of the ligand binding is lower than for the 3-PhPy (Table 3.5), therefore at higher cone voltages it eliminates easier.

We have compared the arrival times of various complexes generated by ESI-MS and summarized the obtained data in Table 3.6. I note that the meaning of the absolute arrival times that can be determined in a SYNAPT is limited, because they strongly depend on the settings (gas pressure, voltage, *ect.*) of the mobility unit. Therefore, they only can be compared for the species measured under identical conditions.

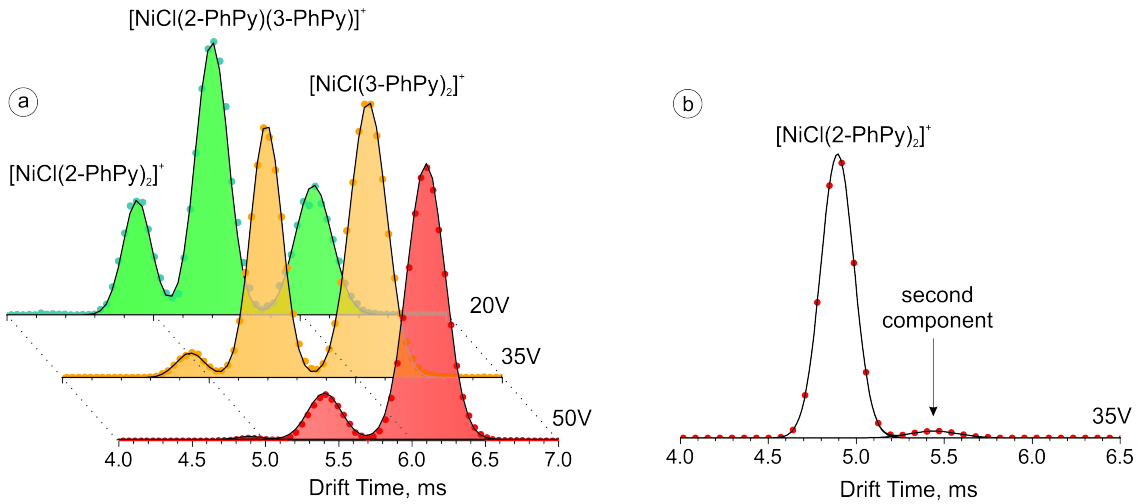

Figure 3.16: a) Arrival time distributions of the mass-selected complex $[NiCl(PhPy)_2]^+$ (m/z = 403) generated upon ESI of a methanolic solution of $NiCl_2$ in the presence of a 1:1 mixture of 2- and 3-PhPy at cone voltages of U_C = 20, 35, and 50 V; b) arrival time distribution of the mass-selected complex $[NiCl(2\text{-}PhPy)_2]^+$ (m/z = 403) generated with a cone voltage of U_C = 35 V. The second component appears at about 5.45 ms. The dots represent the experimental data, black lines - modeled Gaussian curves.

Naturally, the data in Table 3.6 show that the more compact ions have lower arrival times. Namely, the observed arrival times are drastically smaller for dications, increase with the number of ligands and are also smaller for ions containing 2-PhPy. Thus the arrival times of the isomeric complexes confirm the differences in ligand coordination to the cationic metal center, and can be a measure of the structural properties of gaseous ions.

When we looked closely at the arrival time distributions of the isolated ions, we faced a challenge in the interpretation of the second feature on the mobilogram for the $[NiCl(PhPy)_2]^+$ cation (Figure 3.16b). In addition to the major component with an arrival time t_a = 4.94 ms, we have observed a second component arriving at 5.45 ms. A careful check of the exact masses for both species revealed that both of them correspond to the same structure of $[NiCl(PhPy)_2]^+$. Therefore we have performed a series of quantum chemical calculations, in order to unravel the nature of the second feature.

3.3.3 Quantum chemical calculations

The quantum chemical calculations for this section were performed by Dr. Tibor András Rokob. Density functional theory (DFT) was used for the theoretical calculations as it gives a reasonable theoretical treatment for the ions of the size of the investigated

$[NiCl(PhPy)_2]^+$ cation. The situation is complicated by the fact that the investigated ion can exist in two spin states. Bare $NiCl^+$ has a high-spin, triplet ground state, whereas coordination to neutral ligands makes the low-spin ground state more favorable. These two spin states can become less distinguishable with partial coordination. Therefore both the singlet and triplet state structures were calculated for $[NiCl(PhPy)_2]^+$ and were optimized using the BP86 and B3LYP methods. More accurate subsequent single-point calculations were performed using the M06 method. For clarity, in the discussion below only results obtained with the M06 functional will be presented.

Possible isomeric structures of $[NiCl(PhPy)_2]^+$ optimized for both spin states are shown in Figures 3.17-3.18. The coordinational differences in calculated structures arise from the two sources. Firstly, either trigonal bipyramidal or square-planar coordination is possible at the nickel center leading to either *cis*- or *trans* orientations of the two 2-PhPy ligands. Secondly, steric hindrance within the investigated complexes could lead to additional interactions. The located isomeric structures are labeled with reference to the position of the two N-atoms which can be *trans* (*N,N* axial,axial), or *cis* (*N,N* axial,equatorial or *N,N* equatorial,equatorial). Further classification is based on the position of the pendant phenyl ring. Each of the phenyl rings may be oriented so that both C–H and Ni-Cl bonds are pointing in the same direction ("edge" isomer). On the other hand, the C–H and Ni–Cl bonds could be roughly perpendicular or even antiparallel ("face" isomer).

The triplet state structures adopt 5-coordinate trigonal bipyramidal geometries, with a Cl,N,N,C,C coordination. Both carbon atom coordinations to the nickel are loose and their distance from the nickel atom is more or less the same. In the three most stable triplet structures shown in Figure 3.17, the two nitrogen atoms are coordinated in a *cis*-type geometry to the nickel center, with varying phenyl ring coordination. A *trans*-coordinated isomer (*N,N* ax,ax; edge,edge) follows in the stability order among the triplets.

In the singlet state of $[NiCl(2\text{-}PhPy)_2]^+$, the trigonal bipyramidal structure is somewhat distorted towards a square-planar coordination, however the labeling nomenclature remains the same as for the triplet structures (Figure 3.18). The singlet state with the smallest energy has the *trans* configuration (E_{rel} = 5.1 kJ·mol^{-1}). The small relative energy differences for the analyzed structures, as well as the analysis of the transition state structures, shows that the interconversion between edge/face type isomers can proceed with the low barrier, requiring no more than 10-20 kJ·mol^{-1} of energy. And the transition between various *N,N* coordinations requires no more than 25−50 kJ·mol^{-1}. Therefore,

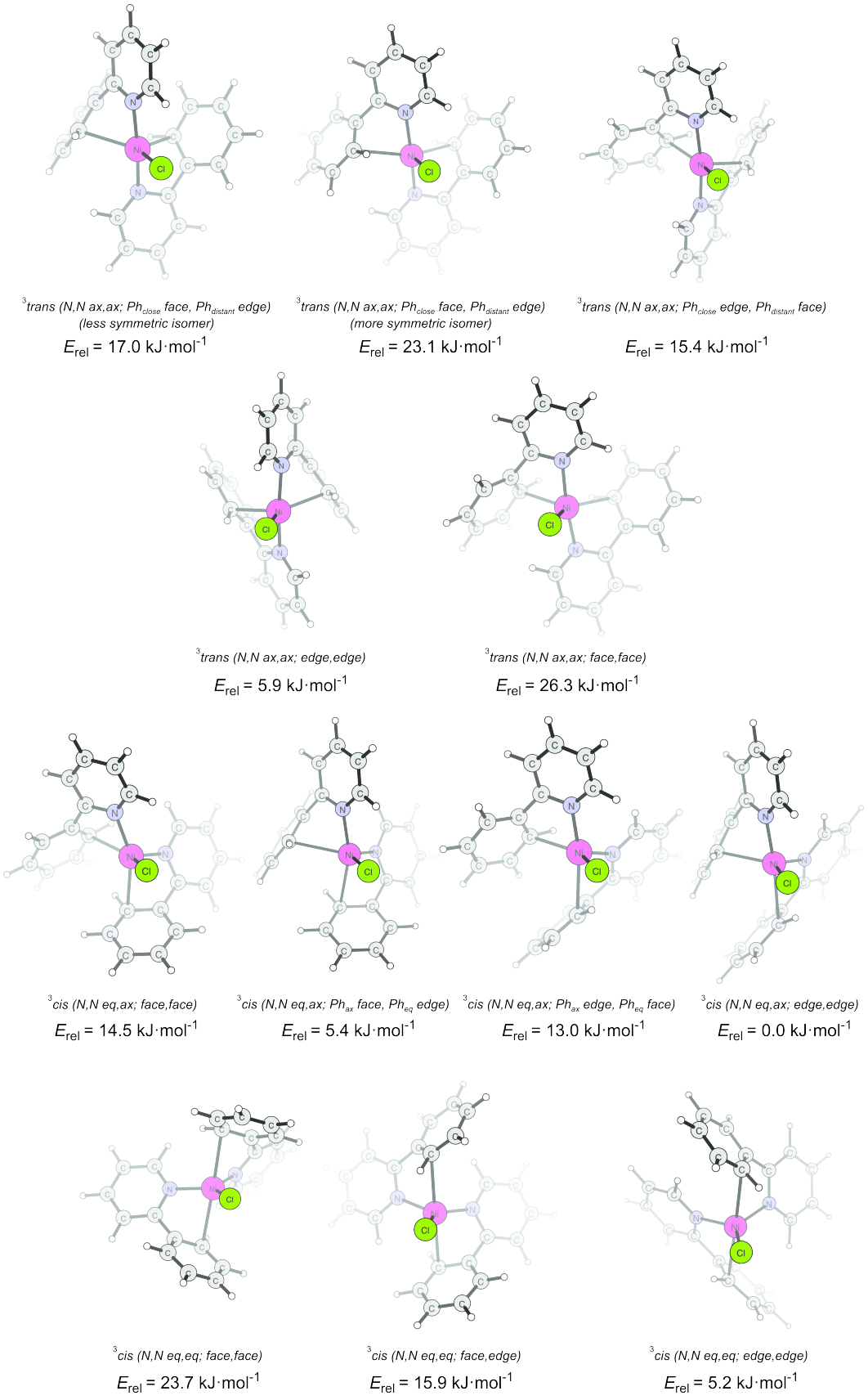

Figure 3.17: Optimized geometries for the triplet isomers of $[NiCl(2\text{-}PhPy)_2]^+$, together with their relative energies with respect to the most stable triplet structure.

the interconversion between various structures proceeds with minor barriers and should be facile.

The calculations also show that the triplet state is slightly more stable than the singlet (5.1 kJ·mol^{-1}). Comparison of the geometries for these two states shows that they largely do not differ. Moreover the spin-state changes are faster with respect to the millisecond scale of the IM-MS module [105].

Furthermore, we have theoretically analyzed the cross sections of the calculated structures (Figure 3.19). The most stable structure has a cross section of about 150 Å^2, however several other low-energy isomers (within 20 kJ·mol^{-1}) exist in the region from 148 up to 156 Å^2. Taking into account the small barriers to interconversion and changes in spin-states, the analysis does not provide a logical explanation for the existence of the second feature in the ion mobility trace of [NiCl(2-PhPy)$_2$]$^+$.

We have further analyzed the geometries of the 3- and 4-PhPy complexes together with those for some of the mixed 2,3- and 2,4- complexes (Figure 3.20). The main difference with respect to the 2,2- isomers is that neither 3- nor 4-PhPy can provide a C-H bond where a carbon would be coordinated to the nickel center, allowing for easy activation. Therefore, both 3,3- and 4,4-isomers are three-coordinated (N,N,Cl). Due to their lower coordination numbers, the triplet states for these structures were found to be favorable. We have found that the triplet structures for the 2,3- and 2,4- isomers were also more stable than the singlet structures, and also slightly more preferred than for the 2,2-isomer.

We have also analyzed the cross sections of the calculated structures. The most stable 2,3-isomers have cross sections of around 158 Å^2, and 2,4-isomers - 163-167 Å^2.

The possible structures of the ion [NiCl(PhPy)]$^+$ that could be formed after the loss of phenylpyridine ligand were also analyzed. For all of the calculated structures, the triplet state was found to be preferable. The energies for the lowest-lying structures and the respective dissociation channels are summarized in Table 3.7. The data show that, as was found in the experiment, the energy required for ligand loss is significantly smaller in the case of 2-PhPy. When we take into account the error values for the experiment as well as for the DFT method, good agreement can be found between experimentally obtained appearance energies for the phenylpyridine loss and the corresponding calculated values (*e.g.* 198 kJ·mol^{-1} *vs.* 170 kJ·mol^{-1} for 2-PhPy, 222 kJ·mol^{-1} *vs.* 215 kJ·mol^{-1} for 3-PhPy, and 220 kJ·mol^{-1} *vs.* 230 kJ·mol^{-1} for 4-PhPy derivatives).

With respect to the experimental findings, the complete reaction pathway for the loss

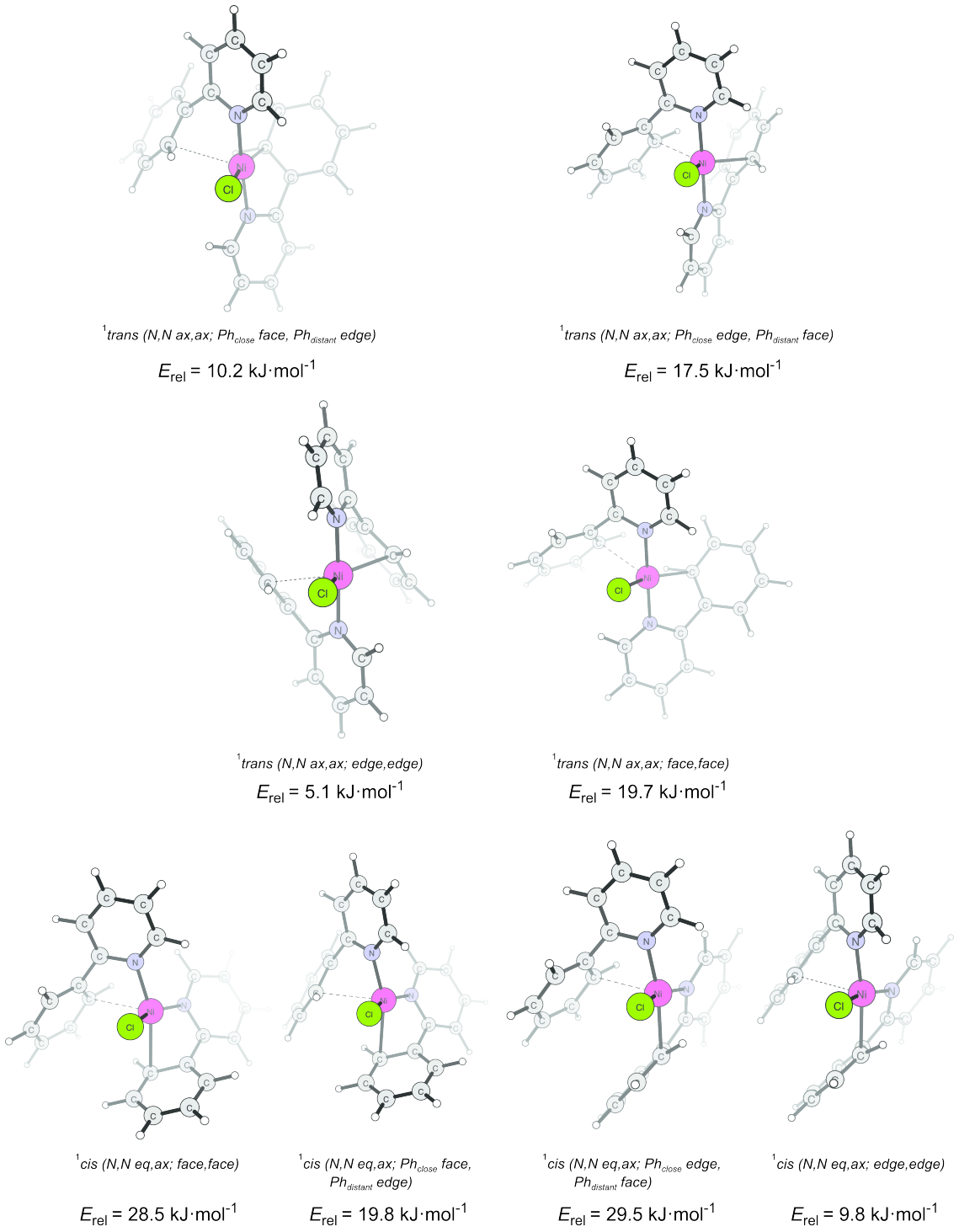

Figure 3.18: Optimized geometries of the singlet $[NiCl(2\text{-}PhPy)_2]^+$ isomers, together with their relative energies with respect to the most stable triplet structure shown in Figure 3.17.

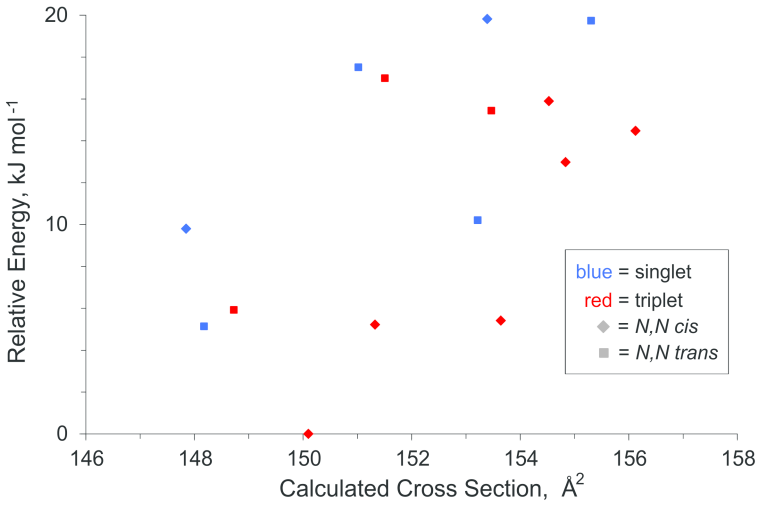

Figure 3.19: Calculated cross sections of the isomeric structures of $[NiCl(2\text{-}PhPy)_2]^+$ within an energy range of 20 kJ·mol^{-1}.

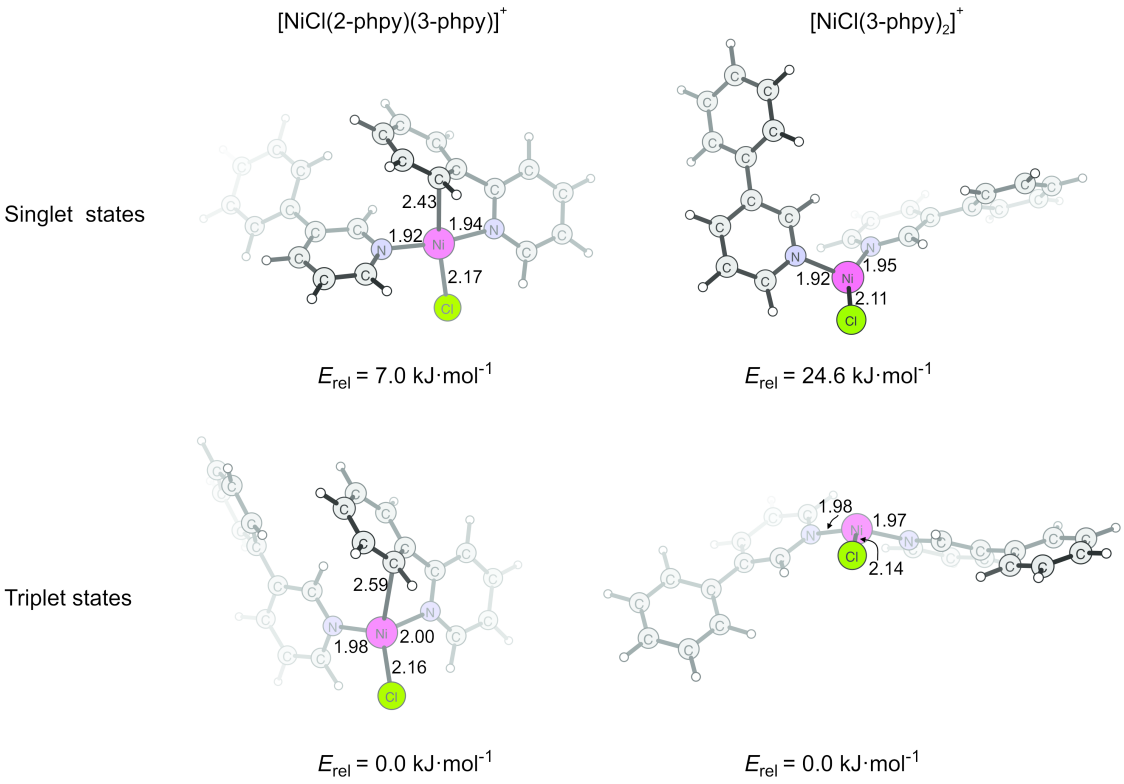

Figure 3.20: Computed structures of the energetically most stable singlet and triplet isomers of $[NiCl(2\text{-}PhPy)(3\text{-}PhPy)]^+$ and $[NiCl(3\text{-}PhPy)_2]^+$. The 2,4- and 4,4-complexes have closely related structures and therefore are not shown.

Table 3.7: 0 K relative energies (in kJ·mol^{-1}) of the various complexes at the M06/def2-TZVPP// B3LYP-D3/def2-SVP level of theory. [a]The energy necessary to initiate a reaction leading to this species exceeds the relative energy of the most stable product; this energy requirement is shown in parentheses. [b]Not calculated.

	$[NiCl(PhPy)_2]^+$		$[NiCl(PhPy)]^+$ + PhPy		$[NiCl(PhPy)]^+$ + HCl	
	singlet	triplet	singlet	triplet	singlet	triplet
2-PhPy	5.1	0	227.5	197.9	109.4 (128.7)[a]	163.3
3-PhPy	84.6	60.1	326.3	281.9	*b*	*b*
4-PhPy	70.8	46.1	310.5	265.2	*b*	*b*

of HCl, was only considered for the ion $[NiCl(2\text{-}PhPy)_2]^+$ (Figure 3.21). We found that the ion $[Ni(2\text{-}PhPy)_2{-}H]^+$, formed after the HCl loss, has a strong preference for the singlet state. No significant difference can be found in the behavior of *N,N-cis* and *N,N-trans* complexes for the triplet state, therefore we have chosen the lower-energy triplet *cis* case for further discussion (red dashed curve).

The pathway that requires the lowest energy for HCl elimination starts from the ^{3}*cis N,N* eq,eq; edge,edge isomer, and goes through the transition state denoted as ^{3}*cis*-**TS**$_1$ with the relative energy 142.6 kJ·mol^{-1} (structures shown in Figure 3.22). The resulting HCl complex (^{3}*cis*-**A**) is only 16 kJ·mol^{-1} below the TS. The HCl ligand can be lost in a barrierless endothermic process to give a triplet $[Ni(2\text{-}PhPy)_2{-}H]^+$ isomer. The product is the highest point along the reaction pathway, with the relative energy of 163.3 kJ·mol^{-1}.

On the singlet surface *trans*-$[NiCl(2\text{-}PhPy)_2]^+$ has similar features to the triplet case. The more favorable singlet *trans* reaction starts from the ^{1}*trans N,N* ax,ax; edge,edge isomer at 5.1 kJ·mol^{-1}. Hydrogen abstraction from the phenyl ring by the chlorine atom goes *via* the transition state ^{1}*trans*-**TS**$_1$ (Figure 3.23) which has a relative energy of 149.6 kJ·mol^{-1}. In the resulting product complex ^{1}*trans*-**A** the HCl ligand is bound to the nickel center by an ion-dipole interaction. The subsequent dissociation of HCl requires an additional 13 kJ·mol^{-1} resulting in the formation of singlet *trans*- isomer of $[Ni(2\text{-}PhPy)_2{-}H]^+$. HCl elimination is notably different in the case of the^1*cis*-$[NiCl(2\text{-}PhPy)_2]^+$ isomer (see Figure 3.24 for computed structures). The initial structure (^{1}*cis N,N* eq,ax; edge,edge) lies at 9.8 kJ·mol^{-1} and is preorganized for the H-abstraction step which might explain the lower barrier for the C-H activation step in this case. Unlike other cases, the resulting product ^{1}*cis*-**B** does not lose HCl in a barierless process. It must first undergo ligand-exchange *via* ^{1}*cis*-**TS**$_2$. The resulting intermediate for this step is ^{1}*cis*-**A**, which is analogues to ^{1}*trans*-**A** as it contains weakly bound HCl that can easily dissociate. The

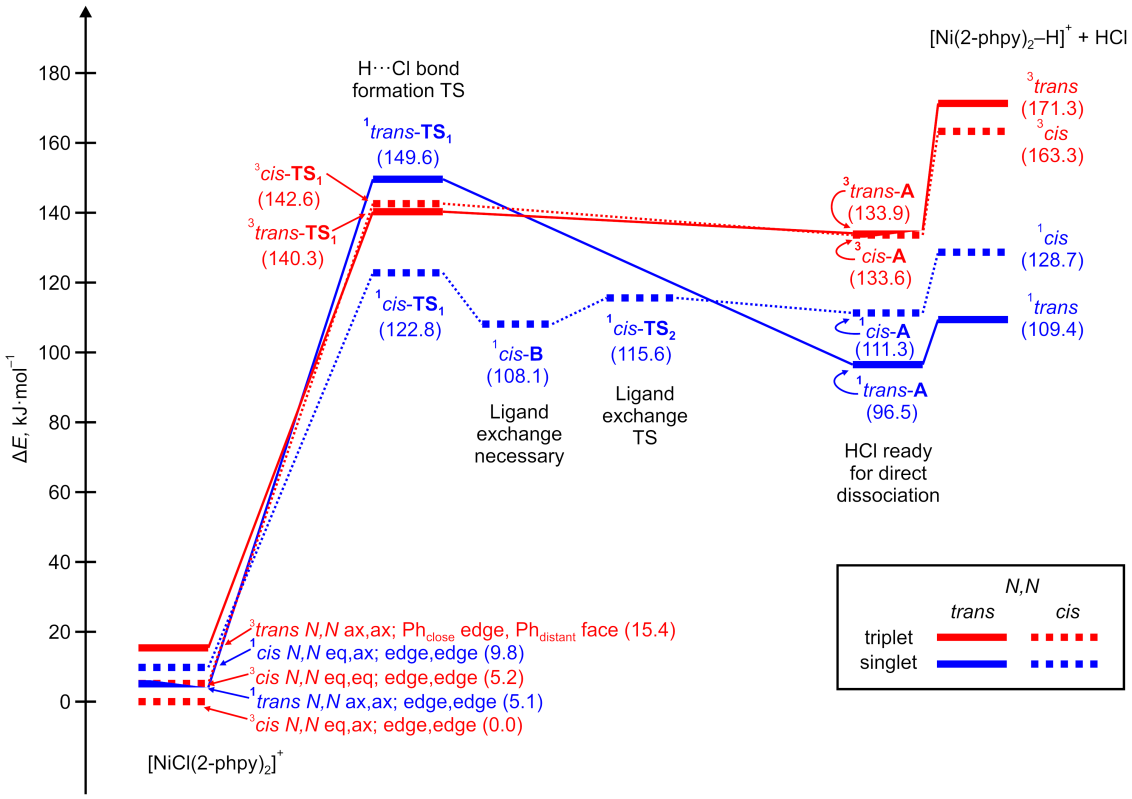

Figure 3.21: 0 K energy profiles for the HCl loss reaction from *cis*/*trans* singlet/triplet $[NiCl(2\text{-}PhPy)_2]^+$ at the M06/def2-TZVPP// B3LYP-D3/def2-SVP level of theory. In all cases, multiple reaction pathways involving energetically close-lying conformers were located, however only the ones having the smallest overall energy demand are shown.

product ion again lies at the highest point along the energy surface (128.7 kJ·mol^{-1}).

The stability order of the products (*i.e.* ^{1}*cis*- and ^{1}*trans*-$[Ni(2\text{-}PhPy)_2{-}H]^+$) does not agree with that of the TSs for H−Cl bond formation (^{1}*cis*-**TS**$_1$ and ^{1}*trans*-**TS**$_1$). Therefore we may ask whether it is possible to arrive at the more stable product (^{1}*trans*) *via* the more stable transition state (^{1}*cis*-**TS**$_1$). We have checked that possibility and indeed found a direct connection between ^{1}*cis*-**B** and ^{1}*trans*-**A**. However the transition state for that transformation lies at ∼150 kJ·mol^{-1} and therefore is unlikely to contribute to the reaction.

Moreover, we have considered an alternative mechanism that involves an oxidative addition step (*via* the formation of the intermediate ion $[Ni(Cl)(H)(2\text{-}PhPy)(2\text{-}PhPy{-}H)]^+$). However, all of the calculated structures for such an intermediate lie above 200 kJ·mol^{-1} in the scale of Figure 3.21, and therefore are considered unlikely to be formed.

The theoretical results also agree with experiment in finding that the elimination of HCl requires less energy than phenylpyridine loss (data in Table 3.7). For the triplet case 163.3 kJ·mol^{-1} is necessary for C-H activation which lies in a very good agreement with the

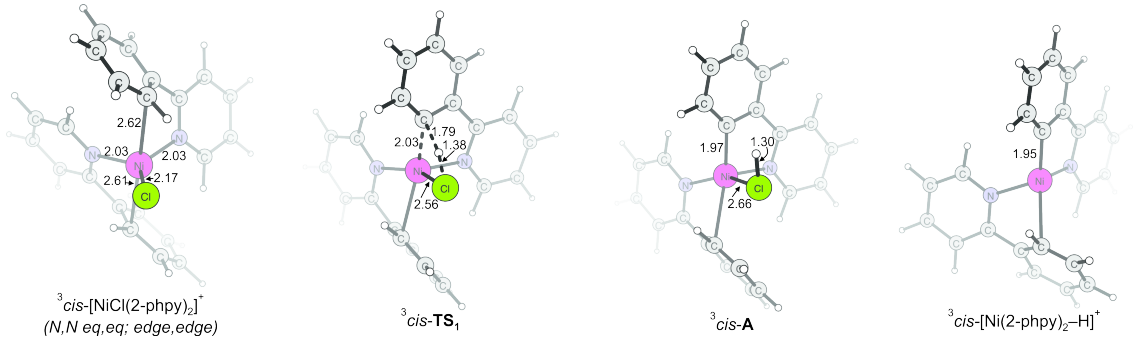

Figure 3.22: Computed structures of the stationary points along the HCl loss reaction of ^{3}*cis*-[NiCl(2-PhPy)$_2$]$^+$.

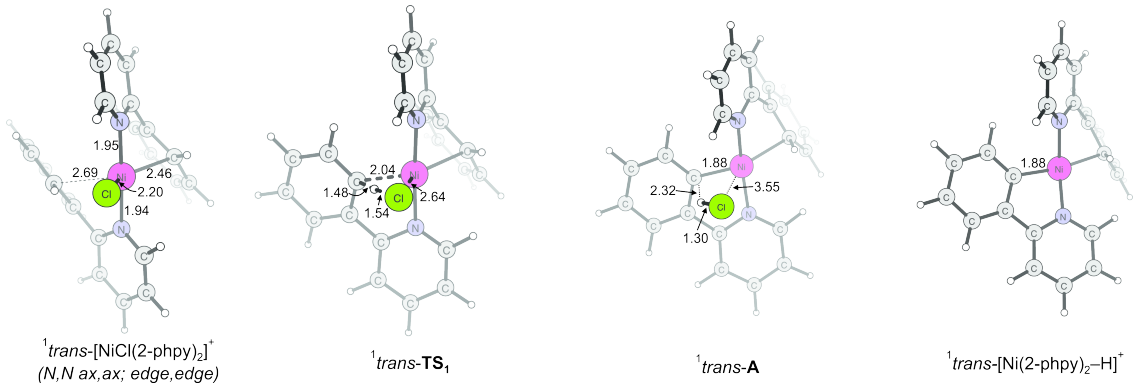

Figure 3.23: Computed structures of the stationary points along the HCl loss reaction of ^{1}*trans*-[NiCl(2-PhPy)$_2$]$^+$.

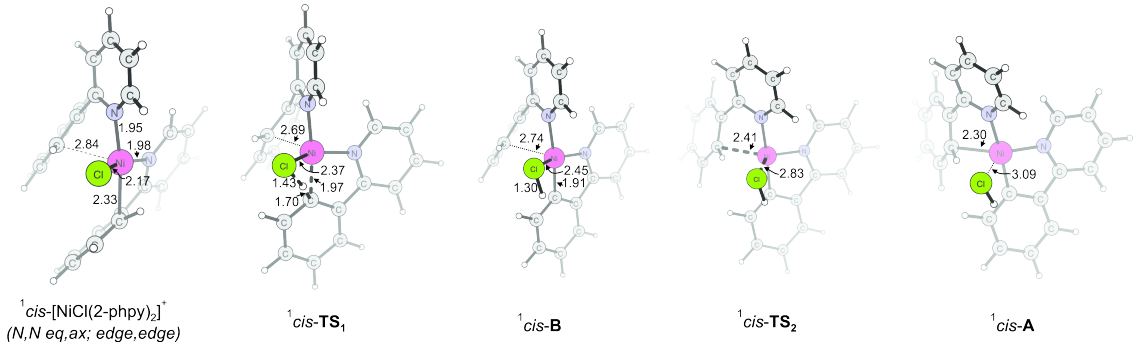

Figure 3.24: Computed structures of the stationary points along the HCl loss reaction of ^{1}*cis*-[NiCl(2-PhPy)$_2$]$^+$.

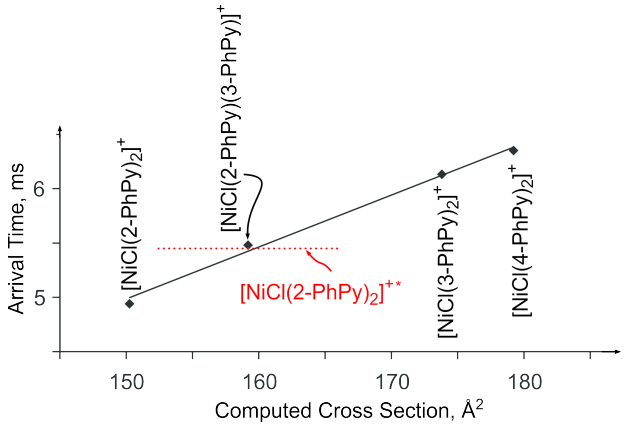

Figure 3.25: Measured arrival times in IM-MS versus computed cross sections of selected $[NiCl(PhPy)_2]^+$ complexes. The red horizontal line denotes the arrival time of the second feature from the $[NiCl(2\text{-}PhPy)_2]^+$sample.

experimentally obtained value of 160 kJ·mol^{-1}. The reaction however may also proceed along the more favorable singlet pathway with an overall energy demand of only 128.7 kJ·mol^{-1}. In that case the experimental appearance energy might be overestimated due to the higher kinetic shift associated with the rearrangements happening along the *cis*- singlet pathway. In that case the agreement between theory and experiment might be considered as reasonable.

As can be seen from the discussion above, our theoretical investigations exclude several possibilities that might explain the existence of the second feature in the ion mobility trace of $[NiCl(2\text{-}PhPy)_2]^+$. The theory confirms the existence of several possible structures with different cross sections, however all of them were predicted to interconvert under the conditions of IM-MS experiments.

As the computational data did not succeed in finding a suitable explanation for the observation of the second feature in the $[NiCl(2\text{-}PhPy)_2]^+$ mobillogram, we returned from theory back to experiment. Comparison of the arrival times of the various $[NiCl(PhPy)_2]^+$ ions with the computed cross sections (Figure 3.25) revealed a good linear correlation.

Moreover, the arrival time of the second feature of $[NiCl(2\text{-}PhPy)_2]^+$ agrees well with the computed cross section of the mixed complex $[NiCl(2\text{-}PhPy)(3\text{-}PhPy)]^+$. Therefore we have checked the commercial sample of 2-PhPy for possible impurities. Selected ion monitoring GC/MS has indeed confirmed a contamination of the commercial sample of 2-PhPy with about 0.2% of 3-PhPy. The presence of this impurity explains the appearance of the second component in Figure 3.16b.

3.4 Investigation of metal-catalyzed carboxylate assisted C-H activation

It was shown that C-H activation reactions can proceed more efficiently *via* so-called ligand direction, especially with ligands acting as bases [106]. Recent mechanistic investigations have shown that ligand assisted C-H bond activation can proceed via a simultaneous metalation and intramolecular deprotonation: the so-called concerted metalation-deprotonation (CMD) mechanism [107–109].

In this study we have chosen to investigate the role of carboxylate, as a directing ligand for C-H activation, and compare the behavior of three metal catalysts: ruthenium, palladium and copper. It was shown that these types of reaction proceed smoothly with unsaturated heterocycles. For example, copper acetate is capable of activating a C-H bond in the C-2 position of 2-phenylpyridine, enabling subsequent nucleophilic substitution [110,111]. Therefore, for our mechanistic study, we have chosen 2-phenylpyridine as the main substrate for C-H activation (Scheme 3.8).

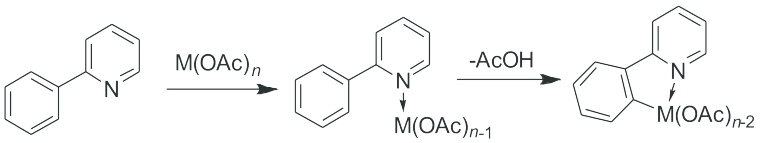

Scheme 3.8: The carboxylate assisted C-H activation investigated here; M corresponds to Ru, Cu and Pd.

3.4.1 ESI-MS studies

C-H activation catalyzed by ruthenium carboxylate

For ruthenium catalysis, we have generated the catalytic LRuOAc species *in situ* using the commercially available complex $[(C_6H_6)RuCl_2]_2$. This was possible upon addition of carboxylic acid and a base to a solution of ruthenium chloride dimer [106]. To this end, we have added 1 equivalent of the acetic acid and thriethylamine to a 0.1 mM solution of the corresponding ruthenium dimer in acetonitrile. The use of triethylamine was motivated by the fact that it is soluble in acetonitrile and therefore suitable for ESI-MS experiments. The spectrum of the resulting mixture is shown in Figure 3.26a (mixture A). It indeed shows the formation of the desired catalytic ruthenium carboxylate species at m/z 400. After that, we added 1 equivalent of 2-PhPy to mixture A and observed the ion at m/z 394 that could correspond to the formation of the $[(C_6H_6)Ru((2\text{-}PhPy)OAc)]^+$ complex. When

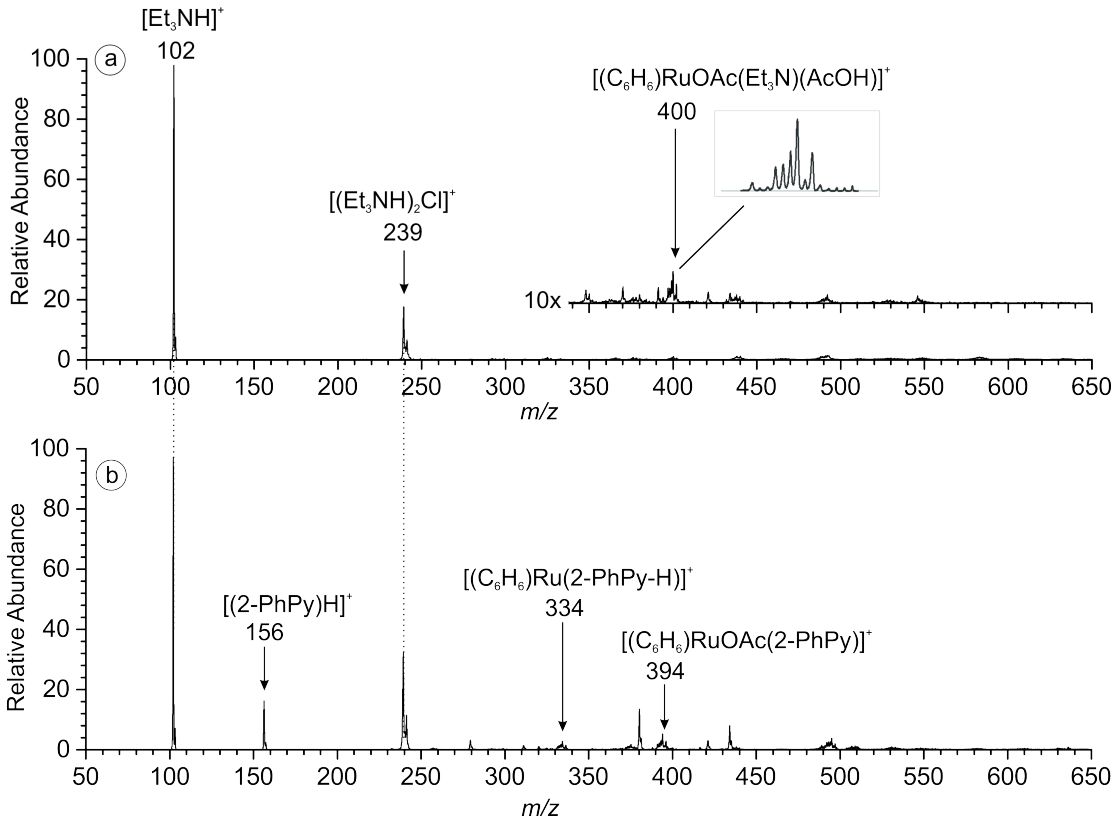

Figure 3.26: a) ESI-MS spectrum of Ru-dimer complex, acetic acid and triethylamine in acetonitrile (mixture A); b) ESI-MS spectrum of Ru-dimer complex, acetic acid, triethylamine and 2-phenylpyridine in acetonitrile.

subjected to CID, the ion at m/z 394 loses acetic acid, forming the ion at m/z 415 with the probable formula $[(C_6H_6)Ru((2\text{-}PhPy)\text{-}H)]^+$. Hence, fragmentation of the ion at m/z 394 could either correspond to C-H activation of the ion $[(C_6H_6)Ru((2\text{-}PhPy)OAc)]^+$, or to elimination of the loosely bound AcOH ligand from the already activated phenylpyridinium complex ($[(C_6H_6)Ru((2\text{-}PhPy)\text{-}H\ (HOAc))]^+$). The energy for the loss of acetic acid was determined as 113 $\pm$ 3 kJ·mol^{-1}.

In order to better understand the behavior of the reaction mixture for ruthenium catalysis and its speciation under ESI-MS conditions, we have studied the dependence of 2-phenylpyridine concentration on the formation of ions in the gas phase. The experiment showed that increasing the concentration of 2-phenylpyridine increases the abundance of both non-activated and activated (m/z 394 and m/z 344) ruthenium complexes (Figure 3.27).

We have also compared the ability of *L*RuOAc catalyst to activate 3-PhPy. To this end, we prepared solutions with 3-PhPy identically to those with 2-PhPy and subjected

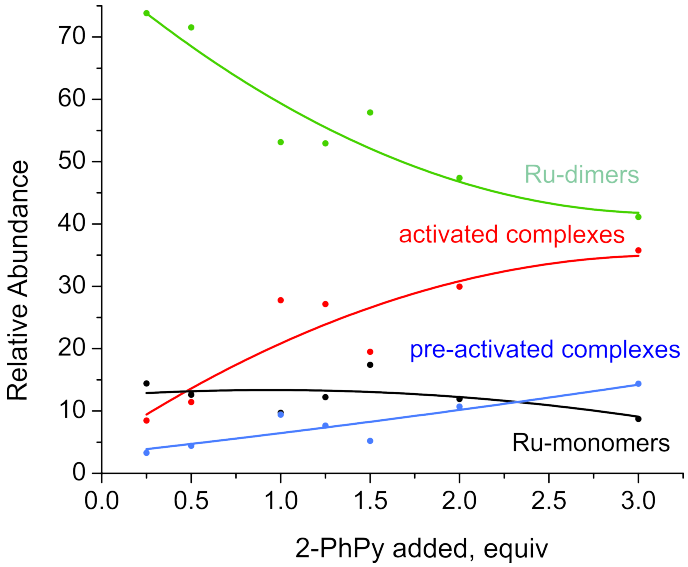

Figure 3.27: Dependence of the relative abundance of various Ru-clusters on the amount of 2-PhPy in the solution.

them to ESI-MS and CID analysis. CID of the ion at m/z 394 showed that although the C-H activation of 3-PhPy is still possible, the major fragmentation pathway is the loss of the neutral 3-PhPy ligand (Figure 3.28a, blue). The energy required for elimination of acetic acid was determined as 173 ± 3 kJ·mol^{-1}.

C-H activation catalyzed by copper acetate

ESI-MS of a copper acetate/2PhPy solution (1:1) in acetonitrile is shown in Figure 3.29. We observed the formation of complex at m/z 432 that can be formally described as a $CuOAc^+$ core bearing two 2-PhPy moieties. CID of this complex showed the appearance of two elimination channels: acetic acid and 2-PhPy losses (Figure 3.30a). We determined the appearance energies for the losses as: 138 ± 5 kJ·mol^{-1} for acetic acid and 147 ± 5 kJ·mol^{-1} for 2-phenylpyridine. As is shown in Figure 3.30, the loss of 2-PhPy is more abundant although it has a higher appearance energy. Hence, elimination 2-PhPy is favored kinetically, whereas elimination of AcOH most likely demonstrates C-H *via* a tight transition state. Therefore, the structure of the ion at m/z 432 corresponds to the non-activated $[Cu(OAc)(2\text{-}PhPy)_2]^+$ rather than activated $[Cu(2\text{-}PhPy)(2\text{-}PhPy\text{-}H)(AcOH)]^+$.

C-H activation catalyzed by palladium acetate

ESI-MS of a palladium acetate-2-PhPy solution (1:1) in acetonitrile is shown in Figure 3.31. The spectrum shows the appearance of ions with a Pd-C bond (*e.g.* m/z 415 and

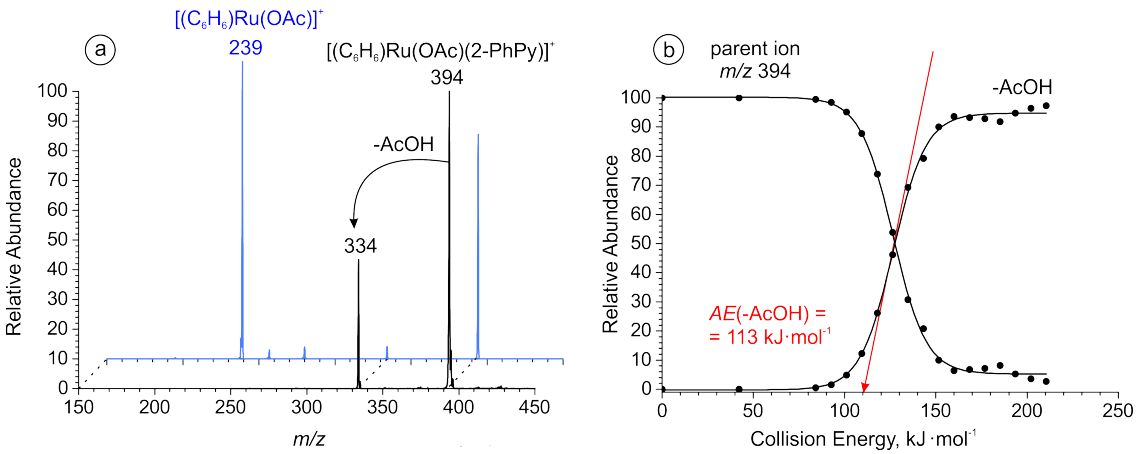

Figure 3.28: a) CID spectra of the mass selected peak at m/z 394 for 2-PhPy (black) and 3-PhPy (blue); b) the breakdown curve for m/z 394 (2-PhPy). The appearance energy for acetic acid loss was determined to be AE(-AcOH) = 113 ± 3 kJ·mol^{-1}.

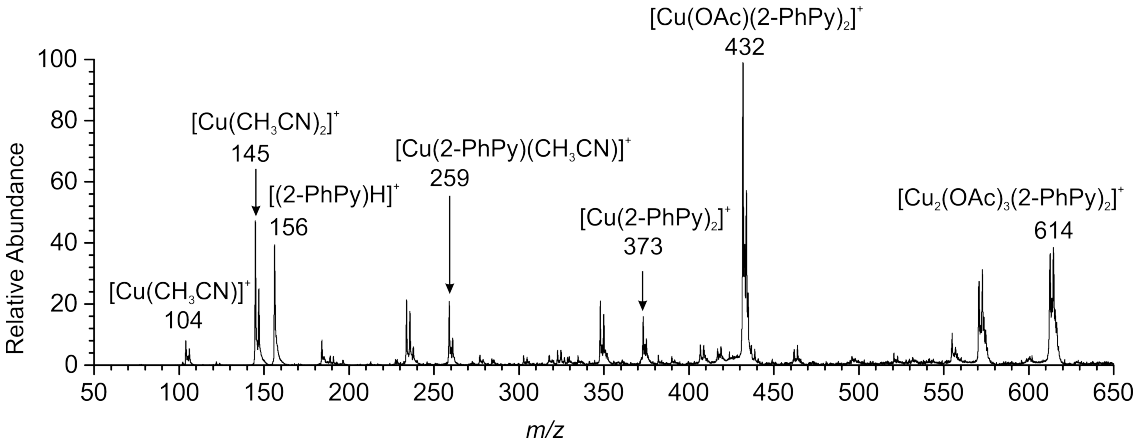

Figure 3.29: ESI-MS spectrum of the mixture of $Cu(OAc)_2$ and 2-PhPy in acetonitrile.

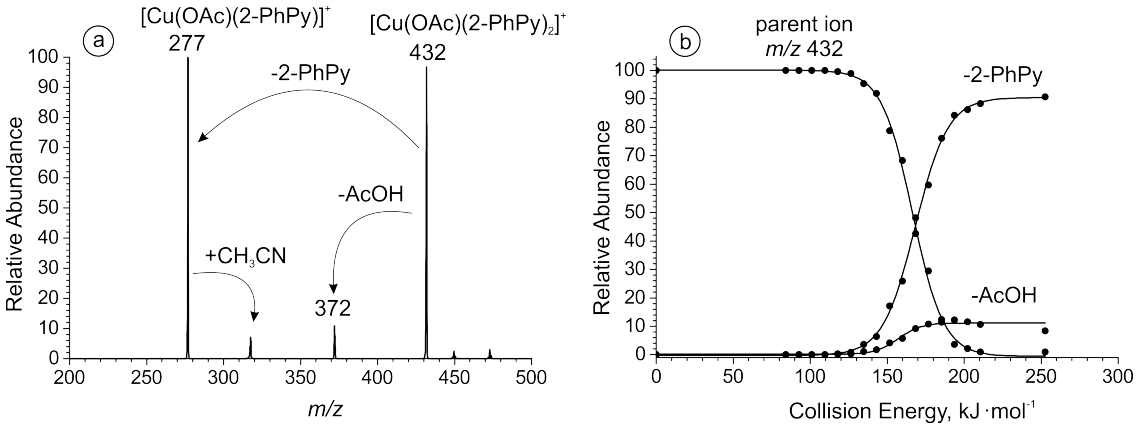

Figure 3.30: The CID spectrum and the breakdown curve for the mass selected peak at m/z 432. AE for the AcOH loss: 138 ± 5 kJ·mol^{-1}, AE for the 2-PhPy loss: 147 ± 5 kJ·mol^{-1}.

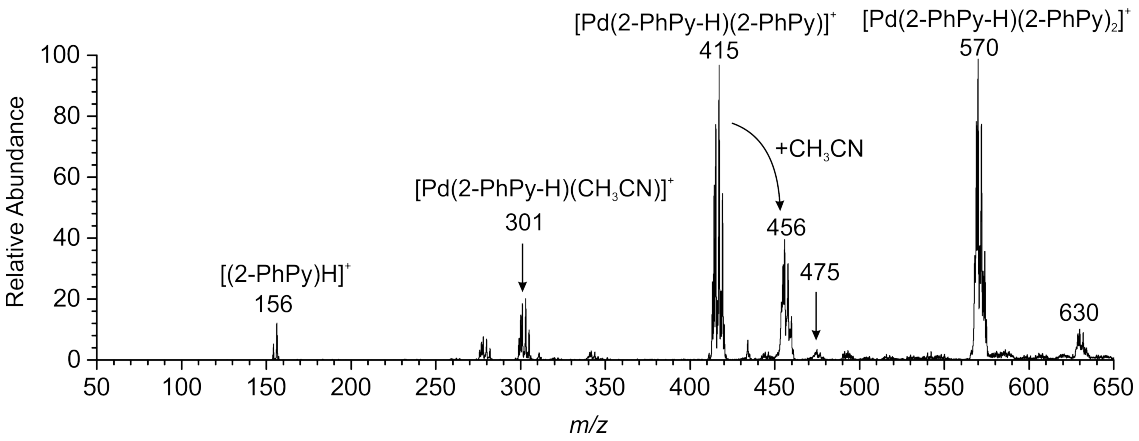

Figure 3.31: ESI-MS spectrum of $Pd(OAc)_2$ and 2-PhPy in acetonitrile.

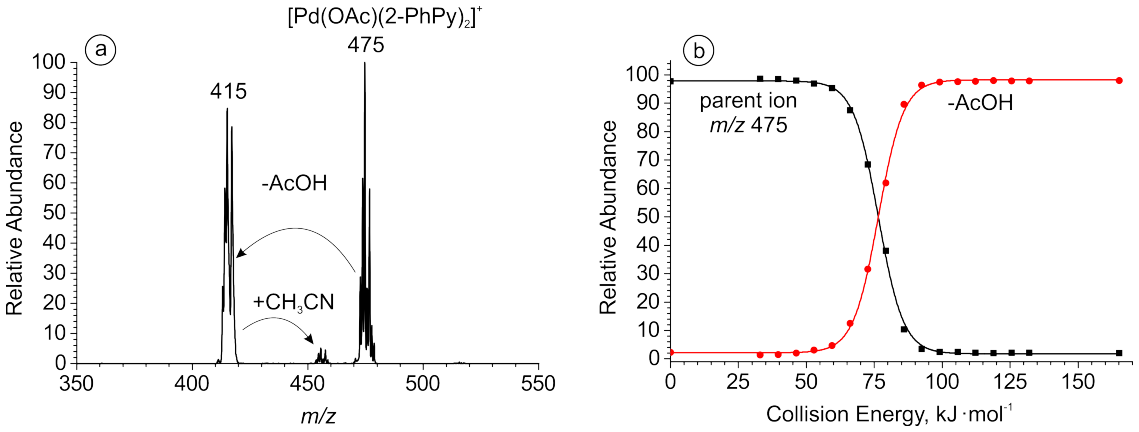

Figure 3.32: The CID spectrum of the mass selected peak at m/z 475 and its breakdown curve. AE for AcOH loss: 65 ± 3 kJ·mol^{-1}.

m/z 570) and possibly pre-activated complexes containing an acetoxy ligand (m/z 475 and 630). The latter are present in small abundances which means that most of the 2-PhPy is already activated. Similar to the copper catalysis, the ion at m/z 475 may correspond to the non-activated Pd-complex: ($[Pd(OAc)(2\text{-}PhPy)_2]^+$).

CID activation of the complex at m/z 475 leads to the exclusive elimination of acetic acid (Figure 3.32), and the appearance energy for this loss is 65 ± 3 kJ·mol^{-1}(this experiment was performed with the mass selection width of 10 m/z with the calibration prepared specifically for this case). The AE for acetic acid loss is much lower than for the previously investigated complexes, therefore the ion at m/z 475 may correspond to the already activated complex $[Pd(2\text{-}PhPy)(2\text{-}PhPy\text{-}H)(AcOH)]^+$.

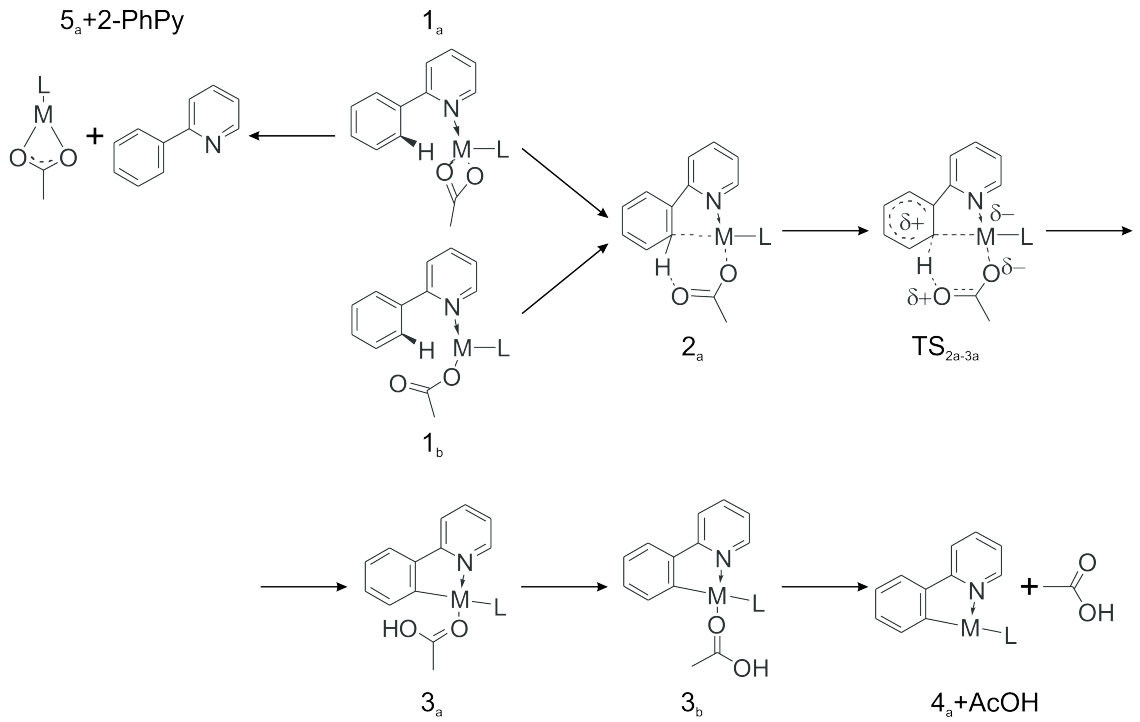

Scheme 3.9: Structural representations of the different calculated species involved in the C-H activation reactions; *M* corresponds to Ru, Cu and Pd.

3.4.2 Theoretical investigations of reaction pathways

The quantum chemical calculations for this section were performed by Dr. Andrew Gray. Three complexes (*m/z* 394, *m/z* 432 and *m/z* 475) investigated with ESI-MS were further subjected to DFT calculations to study the mechanism of acetate assisted C-H activation. The mechanisms have common steps and therefore similar labeling is used to enable their comparison. The progression of the investigated reactions is described in Scheme 3.9.

The individual potential energy surfaces shown below are labeled in accordance with Scheme 3.9. For Ru catalysis *L* represents the π-bonded benzene ligand, while in the Cu or Pd complexes *L* stands for 2-PhPy ligand. Labeling is consistent for all metal complexes; the metal is indicated in the text using superscript prefixes as follows: $^{Ru}1_a$, $^{Cu}1_a$ and $^{Pd}1_a$.

Potential energy surface for ruthenium complexes

The calculated reaction pathway for $[(2\text{-PhPy})Ru(C_6H_6)(OAc)]^+$ is shown in Figure 3.33. It includes the transfer of a proton from the 2-PhPy to the acetate ligand. The reaction starts at the lowest energy intermediate $^{Ru}1_a$ where acetate is bound to Ru as a bidentate ligand. Next, it interconverts to $^{Ru}2_a$with an energy barrier of 60 kJ·mol^{-1}, where Ru is

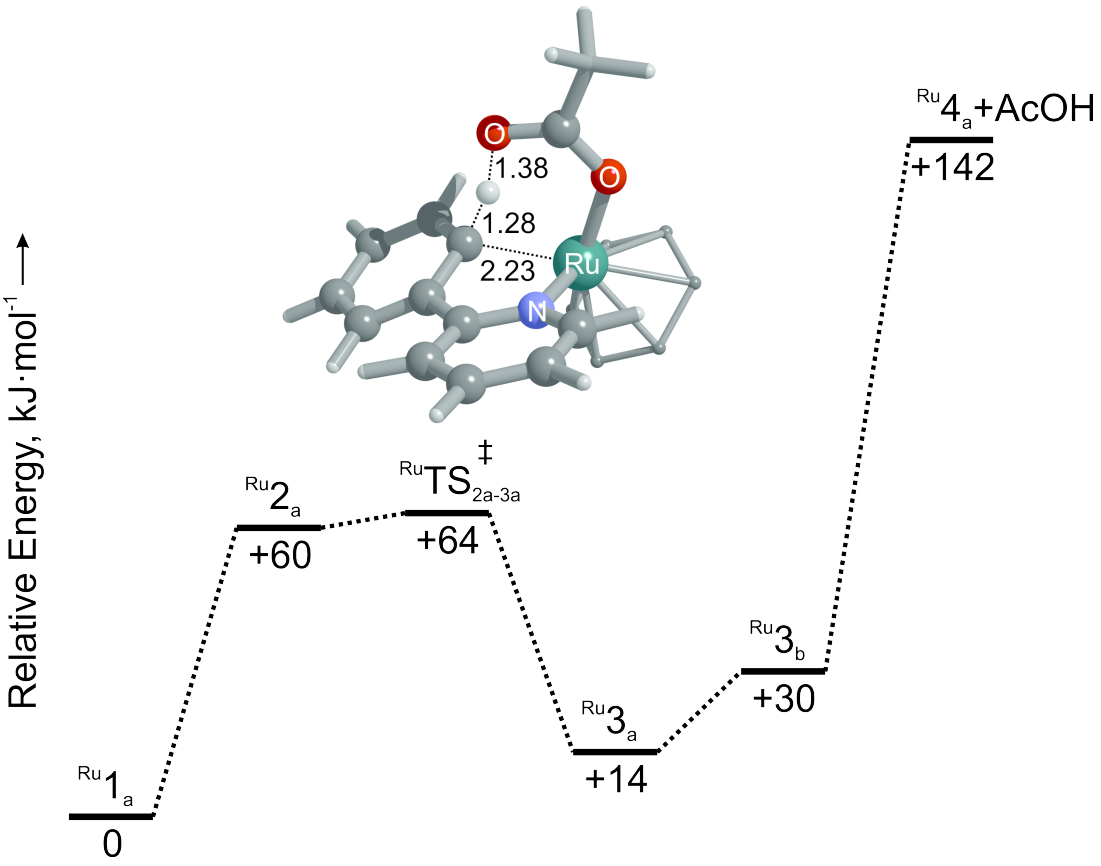

Figure 3.33: Zero point potential energy surface (B3LYP/cc-pVTZ:cc-pVTZ-pp(Ru)) for the Ru assisted C-H activation of 2-PhPy. Representations of the structures are presented in Scheme 3.9. Distances are in Å.

bearing acetate monodentally. The second oxygen atom is now weakly coordinated to the C-2 proton of 2-PhPy, where activation will take place. In addition, a weak interaction is present between the ruthenium and carbon atoms. We will be referring to this structure as pre-activated, as it allows easy proton transfer to take place. The hydrogen transfer from this complex requires only 4 kJ·mol^{-1} forming the transition state $^{Ru}TS_{2a\text{-}3a}$. The transition state leads to the activated intermediate $^{Ru}3_a$ with acetic acid bound to Ru and is 14 kJ·mol^{-1} less stable than the non-activated initial structure. In intermediate $^{Ru}3_a$ a weak interaction between the OH group and 2-PhPy is present that can be removed with an energy cost of 16 kJ·mol^{-1}. Acetic acid is only bound to the metal ion in the resulting intermediate ($^{Ru}3_b$). From this point, dissociation of the acetic acid ligand can take place with an energy cost of 112 kJ·mol^{-1} giving an overall energy increase for this transformation of 142 kJ·mol^{-1}.

Potential energy surface for copper complexes

The calculated potential energy surface for Cu-catalyzed C-H activation is shown in Figure 3.34. Although the reaction steps follow a similar progression, the mechanism has some differences compared to that of ruthenium (Figure 3.33). In spite of the change of supporting ligand *L* from benzene to 2-PhPy, the reaction still proceeds *via* similar structures: $^{Cu}1_a$, $^{Cu}TS_{1a\text{-}3b}$, $^{Cu}1_b$ and $^{Cu}4_a$. However, energy differences for each step are very different compared to those for Ru-catalysis. Two additional initial structures ($^{Cu}1_{a*}$ and $^{Cu}1_b$) are listed in Figure 3.34. In the $^{Cu}1_b$ structure the metal bears a monodentate acetate ligand. This structure lies 94 kJ·mol^{-1} higher in energy and is strongly disfavored. An alternative structure ($^{Cu}1_{a*}$) with bidentally coordinated acetate featuring a less favored 2-PhPy ligand arrangement is also shown. They are included for comparison to show the favorability of the $^{Cu}1_a$ initial structure. Hydrogen transfer from 2-PhPy to acetate now requires 139 kJ·mol^{-1} which is considerably greater than the 64 kJ·mol^{-1} for the equivalent ruthenium process.

The distances in the transition structure are also changed. Now, the distance between Cu and H is 2.24 Å, whereas for Ru-H it was 2.22 Å. If we take into account the relative size of the two metal ions (first row *vs* second row) the observed uniformity in the M-H distances is striking. It shows that the larger Ru has a greater influence on the transition state, perhaps even supporting this transfer, and helps to explain the increased activation barrier in the Cu case. The energy gap between the activated and non-activated complexes (*i.e.* 3_b and 1_a) for copper and ruthenium is also considerably different. With copper it is 96 kJ·mol^{-1} while with ruthenium it was only 30 kJ·mol^{-1}. Next, the energy requirement for the elimination of AcOH from $^{Cu}3_b$ is only 60 kJ·mol^{-1} and the overall energy demand is 156 kJ·mol^{-1}.

The large initial activation barrier suggests that we observe and excite the initial $^{Cu}1_a$ isomer in the mass spectrometry experiments. The 2-PhPy dissociation pathway proceeded theoretically at 179 kJ·mol^{-1} which is 23 kJ·mol^{-1} higher than AcOH elimination.

Potential energy surface for palladium complexes

The calculated reaction pathway for Pd-catalyzed C-H activation is shown in Figure 3.35. Of particular note is the high activation energy relative to the dissociation energy of acetic acid and also the large stability associated with the activated product. The monodentate version of the starting conformation is 88 kJ·mol^{-1} less stable than the bidentate isomer

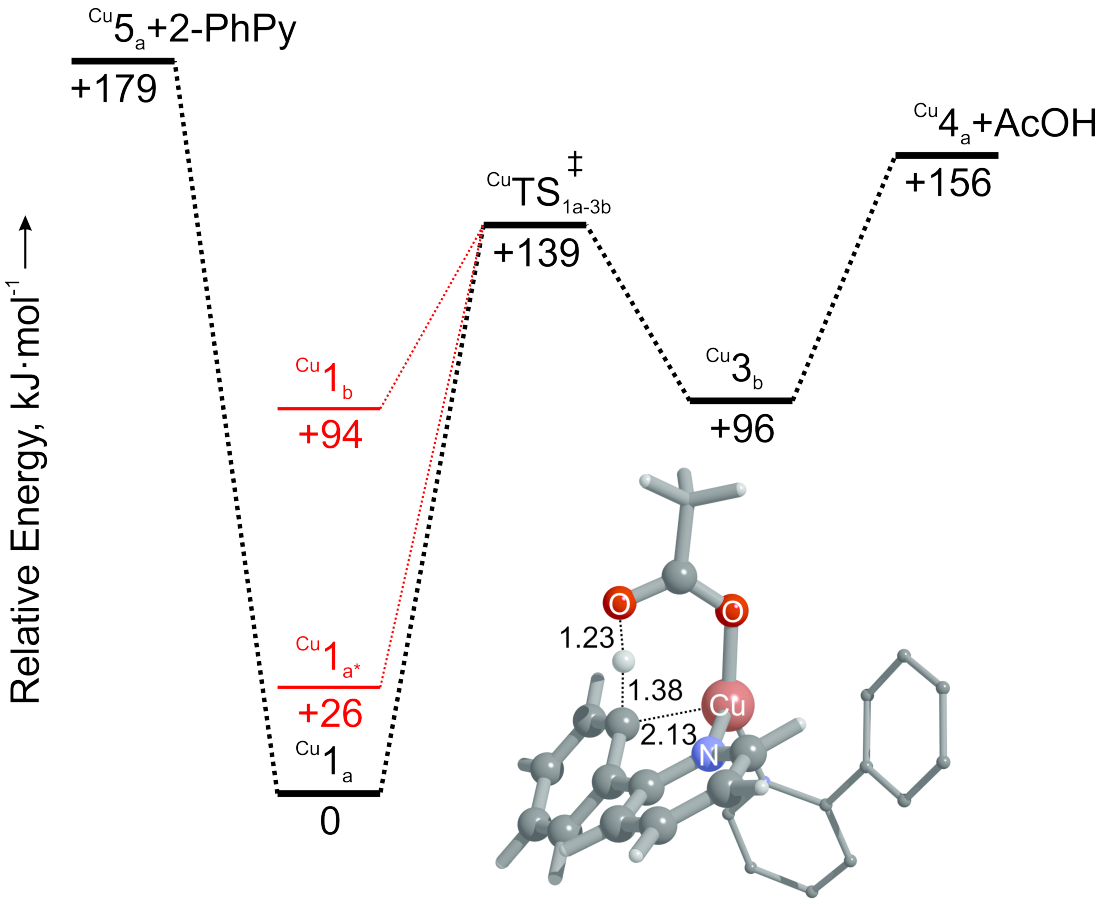

Figure 3.34: Zero point potential energy surface (B3LYP/cc-pVTZ:cc-pVTZ-pp(Cu)) for the Cu assisted C-H activation of 2-PhPy. Representations of structures are shown in Scheme 3.9. Distances are in Å.

which is similar to the copper case (94 kJ·mol^{-1} difference). Therefore the change of metal does not play a big role in this step. Next, a distorted bidentate isomer ($^{Pd}2_a$) was optimized, whose conformation allows the C-2 site of 2-PhPy to be brought into the vicinity of the metal. The calculated distances between the metal and other atoms are rather short (Pd-O 3.00 Å, Pd-H 2.67 Å and Pd-C 3.14 Å). However in the equivalent ruthenium structure, the metal to carbon association is stronger (Ru-O 3.27 Å, Ru-H 2.34 Å and Ru-C 2.48 Å). The TS has an activation energy of 83 kJ·mol^{-1} which is higher than the one for Ru (64 kJ·mol^{-1}), but lower than for Cu (139 kJ·mol^{-1}). The Pd-H distance in the TS was found to be the smallest (1.97 Å) of the three metals which points to the strong influence from the metal. The difference in the relative energy of structures $^{Pd}3_{a/b}$ is probably the most significant. These structures, still bearing AcOH ligand, actually appeared to be more stable than the non-activated $^{Pd}1_a$ structure. This observation may find reasoning in the ability of the structures to adopt square planar conformations. The

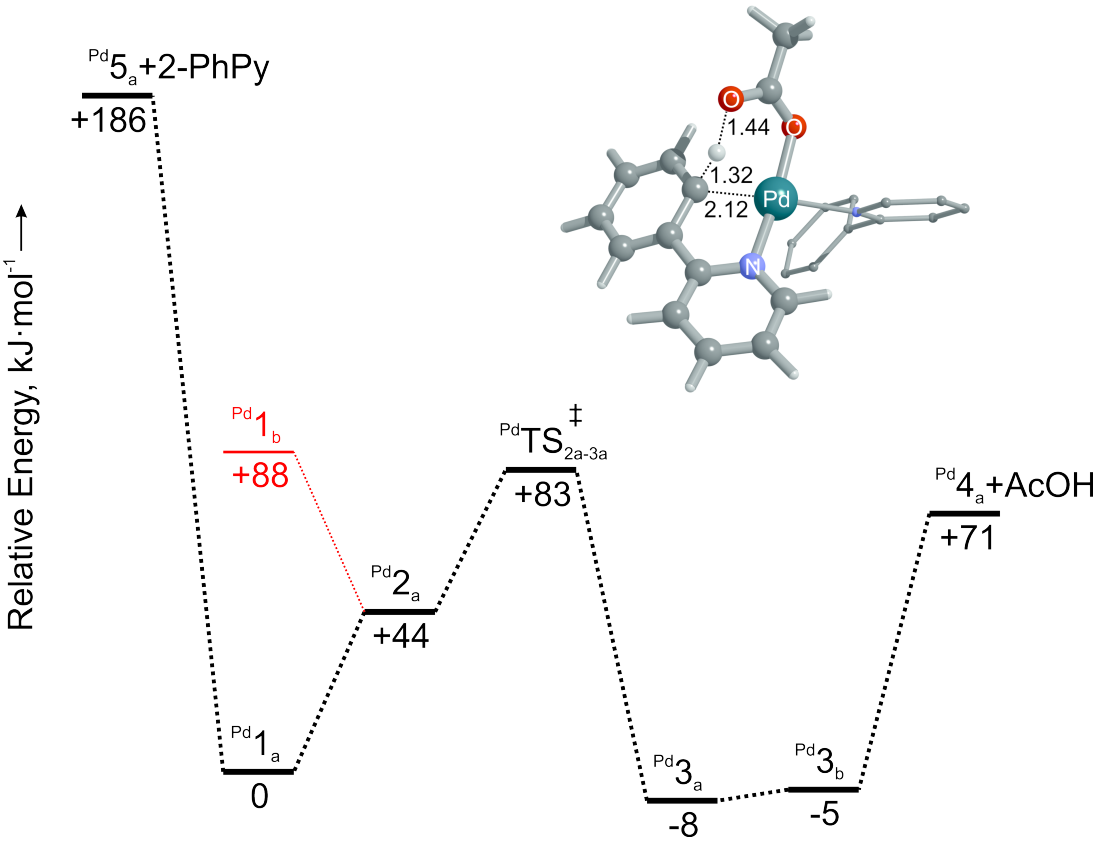

Figure 3.35: Zero point potential energy surface (B3LYP/cc-pVTZ:cc-pVTZ-pp(Pd)) for the Pd assisted C-H activation of 2-PhPy. Representations of structures are shown in Scheme 3.9. Distances are in Å.

equivalent ($^{Cu}3_b$) structure is close to tetrahedral and very unstable compared to $^{Cu}1_a$. The energy of acetic acid dissociation from $^{Pd}3_b$ was found to be 76 kJ·mol^{-1}. This value corresponds well with the equivalent dissociation from the Cu complex (60 kJ·mol^{-1}) but it is about half of that found with the ruthenium complex (112 kJ·mol^{-1}). This value is also lower than the reverse C-H activation barrier (88 kJ·mol^{-1}).

The theoretical energy required for elimination of AcOH from $^{Pd}3_a$ (79 kJ·mol^{-1}) is also lower than the proton transfer barrier from $^{Pd}1_a$ (83 kJ·mol^{-1}). Elimination of 2-PhPy from $^{Pd}1_a$ was shown to take place with a fragmentation energy of 186 kJ·mol^{-1}, considerably higher than for AcOH. Therefore this fragmentation channel is not observed experimentally.

3.4.3 Infrared multiphoton dissociation studies

The ions $[(2\text{-PhPy})Ru(C_6H_6)(OAc)]^+$, $[(2\text{-PhPy})_2Cu(OAc)]^+$ and $[(2\text{-PhPy})_2Pd(OAc)]^+$ were further subjected to IRMPD experiments. The band positions on the obtained spectra

reflect their IR properties and, being compared with theoretically calculated spectra can give structural information [112]. Experimental spectra were recorded in the wavenumber range 900 cm^{-1} to 1800 cm^{-1}. As is routine practice, these are individually compared with theoretical IR spectra calculated by DFT calculations for multiple possible isomers. The comparison allowed identification of the isomer that was isolated and analyzed in the gas phase [28,34,113–115].

IRMPD - Ru

The experimental IRMPD spectrum for the complex $[(2\text{-PhPy})Ru(C_6H_6)(OAc)]^+$ is shown in Figure 3.36. It compares well with the theoretical spectrum for the non-activated isomer ($^{Ru}1_a$). 3-D representations of the calculated structures are located next to the theoretical spectra. In structure $^{Ru}1_a$ acetate is bound as a bidentate ligand to the ruthenium atom, which is coordinated to the nitrogen of 2-PhPy and π-bonded to the aromatic system of benzene. This structure was found to have the lowest energy and is therefore the most stable in comparison to the other calculated isomers. The vibration bands of $^{Ru}1_a$ show a strong match to the experimentally observed spectrum: the bands at 1480 cm^{-1} represent symmetric and asymmetric C-O acetate stretching modes, and C-C double bond stretches of the 2-PhPy ligand (1557 and 1605 cm^{-1}). The experimental spectrum also shows bands at 1403 and 1435 cm^{-1} that correspond to C-H bends within the acetate ligand. Figure 3.36c shows a pre-activated complex with the ligands turned to allow for easy proton transfer from 2-PhPy to OAc^-. The IR spectrum of $^{Ru}2_a$ is a poor match with experiment especially for the key experimental C-O and C-C stretches. In addition, we do not see the characteristically shifted C-O vibrations (1284 and 1666 cm^{-1}) in the experimental spectrum. The activated complex (Figure 3.36d) is also a poor match with weak bands present in the key experimental range. As with Figure 3.36c the strong bands at 1250 cm^{-1} (combination of O-C-C antisymmetric stretch and OH bend) and 1665 cm^{-1} (metal coordinated C-O stretch) have no obvious match in the experimental spectrum.

IRMPD - Cu

An IRMPD spectrum for $[(2\text{-PhPy})_2Cu(OAc)]^+$ was also acquired and is presented with theoretical spectra for different isomers in Figure 3.37. Excellent agreement was found between the theoretical spectra for the stable non-activated intermediate ($^{Cu}1_a$) and the experimental spectrum. In particular, a strong correlation was found for the dominant

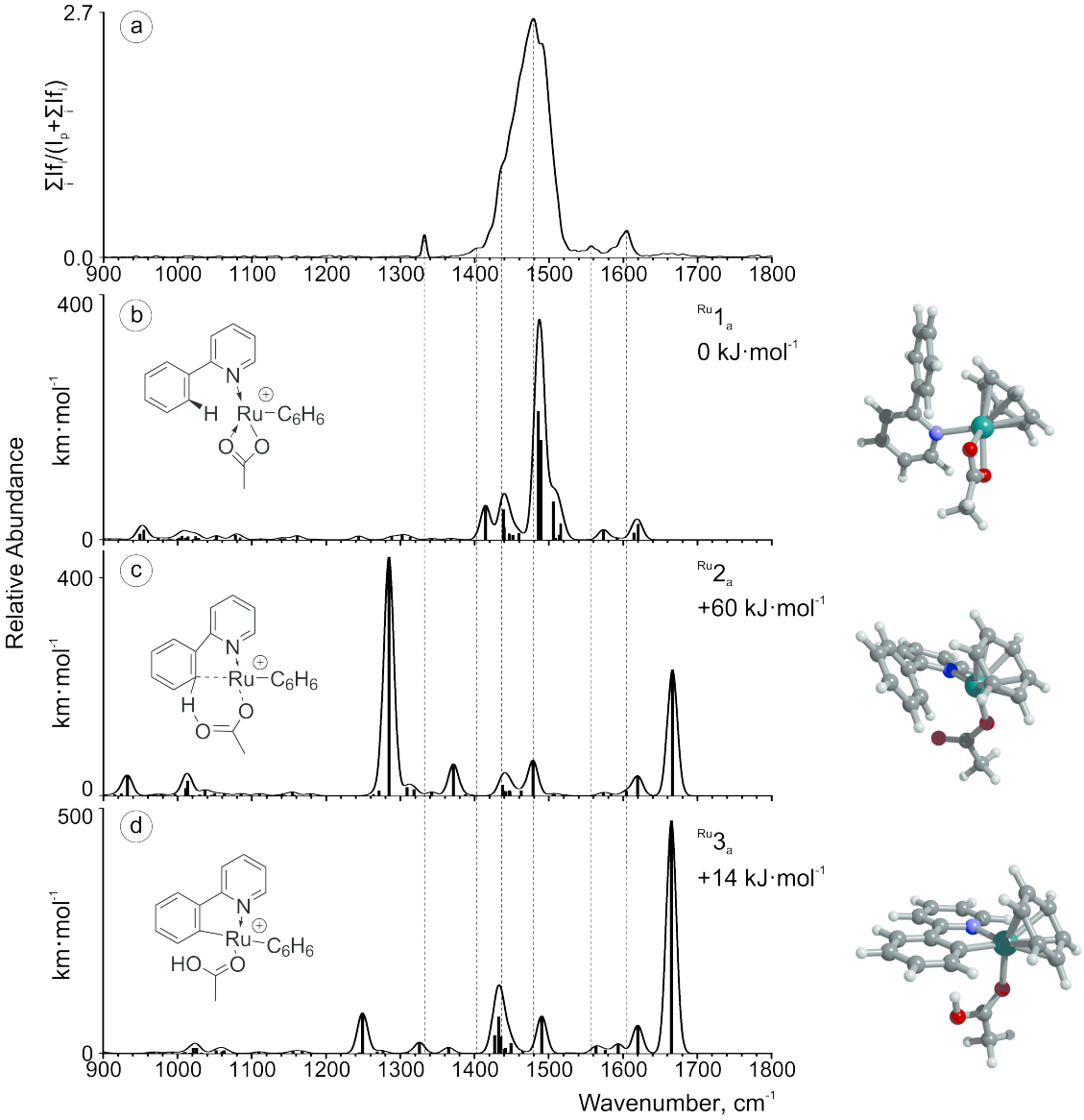

Figure 3.36: (a) IRMPD spectrum of the mass-selected $[(2\text{-PhPy})Ru(C_6H_6)(OAc)]^+$ complex and theoretical IR spectra of (b) $^{Ru}1_a$, (c) $^{Ru}2_a$ and (d) $^{Ru}3_a$. The line spectra are presented along with a Gaussian function with fwhm = 16 cm^{-1}.

peaks centered around 1490 cm^{-1}. In the theoretical spectrum these signals are largely the result of symmetric and asymmetric C-O stretches.

Similar but weaker bands can be found in the other isomers and are largely the result of C-C double bond vibrations within the 2-PhPy ligands. The 1414 and 1438 cm^{-1} bands in Figure 3.37b are from C-H deformations in the acetate ligand. These match the broad shoulder in the experimental spectrum around 1450 cm^{-1} and there are good matches possible for the experimental peaks at 1564 and 1608 cm^{-1} that result from C-C double bond vibrations in the 2-PhPy ligands. Four small experimental noise spikes are present

at 1058, 1146, 1331 and 1784 cm^{-1} that will not be matched with theoretical results. Also of note is the broad region between 900 and 1200 cm^{-1} where low-intense bands can be seen in all Figures 3.37a, 3.37b and 3.37c. Figure 3.37c shows a pre-activated intermediate ($^{Cu}1_b$) where only one oxygen atom is bound to the metal, while Figure 3.37d shows the activated product ($^{Cu}3_b$) where acetic acid is bound to the copper. Both of these structures provide a reasonable match in the 1400 to 1650 cm^{-1} region where the C-C stretches in the 2-PhPy ligands are highly active. However, the key peaks are those resulting from oxygen involvement and these are not represented experimentally. In particular C-O vibrations predicted at 1238 and 1723 cm^{-1} in Figure 3.37c are not found experimentally. While the 1209 cm^{-1} combination O-C-C antisymmetric stretch with an O-H bend and the 1701 cm^{-1} metal bound C-O stretch in Figure 3.37d were also not experimentally observed. The clear experimental observation of $^{Cu}1_a$ is in line with the theoretically predicted potential energy surface where this isomer was by far the most stable. This is the same as what was observed with Ru and strongly indicates the presence of collisionally induced C-H activation of 2-PhPy for these metals.

IRMPD - Pd

The experimental IRMPD spectrum for $[(2\text{-PhPy})_2Pd(OAc)]^+$ is shown in Figure 3.38a and is considerably more complicated than the spectra shown for the earlier examples. Its comparison with the calculated individual theoretical spectra does not provide an ideal match. Therefore it is possible that either a non-considered isomer was observed experimentally or the experimental spectrum represents a contribution from two or more isomers. Analysis of the corresponding potential energy surface (Figure 3.35) reveals that in fact a mixed contribution is possible due to the small energy differences between structures $^{Pd}1_a$ and $^{Pd}3_a$. The relevant theoretical spectra show clear similarities between the Pd complexes and their Cu/Ru equivalents. It seems that the experimental spectrum is dominated by the $^{Pd}1_a$ isomer with the large C-O stretching peak at 1485 cm^{-1}. The peaks at 1401 and 1433 cm^{-1} also match well and correspond to the C-H bending of acetic acid, while the peaks at 1575 and 1621 cm^{-1} correspond to C-C stretching modes of the 2-PhPy ligands.

The experimental bands that do not match with $^{Pd}1_a$ structure could result from the presence of the $^{Pd}3_a$ isomer. This isomer shows particularly good matches with the bands at 1225 and 1695 cm^{-1}, where the former results from a combination of a O-C-C asymmetric stretch and an O-H bend, while the latter corresponds to a C-O stretch involving the

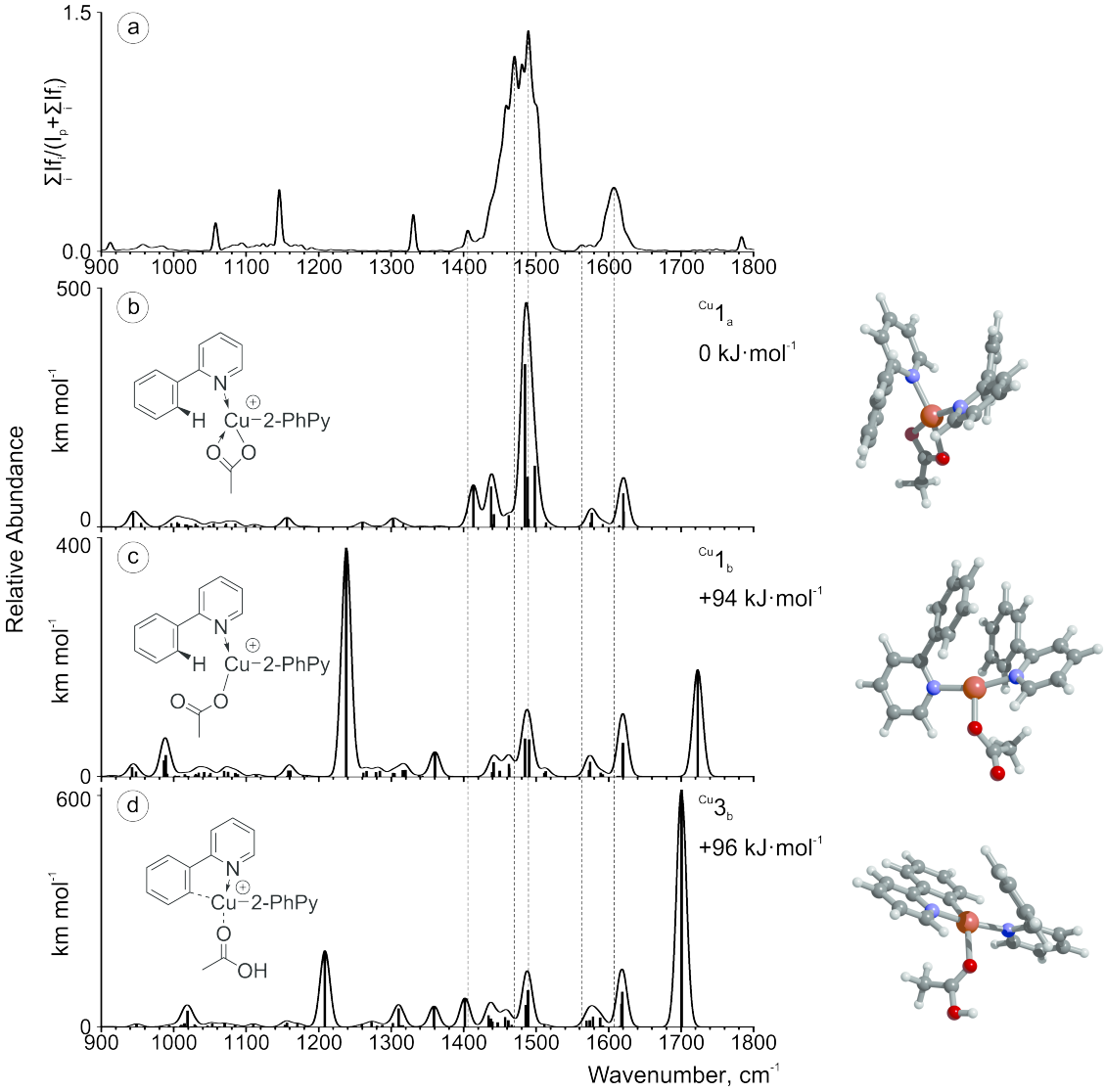

Figure 3.37: (a) IRMPD spectrum of the mass-selected $[(2\text{-PhPy})_2\text{Cu(OAc)}]^+$ complex and theoretical IR spectra of (b) $^{Cu}1_a$, (c) $^{Cu}1_b$ and (d) $^{Cu}3_b$. The line spectra are presented along with a Gaussian function with fwhm = 16 cm^{-1}.

metal coordinated oxygen. The dual contribution as well as energy profile demonstrate an interesting feature of the Pd-catalysis example.

3.4.4 Comparison of the experimental and theoretical results

During our theoretical studies we have applied a number of methods and basis sets in order to better understand and theoretically describe the gas-phase behavior of the investigated ions. Table 3.8 summarizes some of the most important results.

It can be seen that the dispersion correction influences the elimination channel of AcOH dramatically. On the other hand, the activation barriers change only slightly, regardless

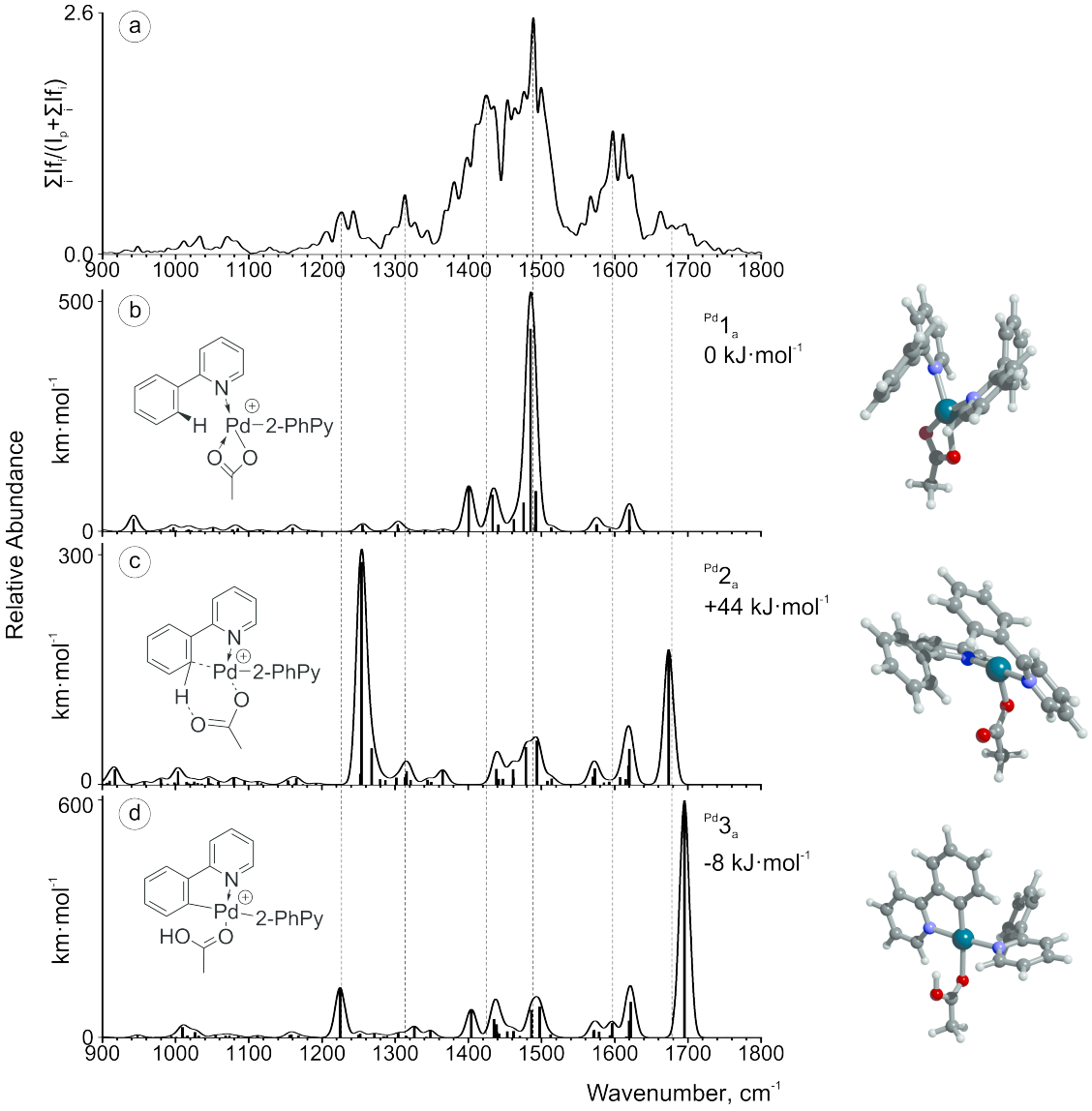

Figure 3.38: (a) IRMPD spectrum of the mass-selected $[(2\text{-PhPy})_2\text{Pd(OAc)}]^+$ complex and theoretical IR spectra of (b) $^{Pd}1_a$, (c) $^{Pd}2_a$ and (d) $^{Pd}3_a$. The line spectra are presented along with a Gaussian function with fwhm = 16 cm^{-1}.

of the chosen method. According to Grimme's recent report [116], dispersion corrections performed on cations are overestimating the dissociation energies, and a similar effect is also reflected in our results. For clarity, the discussion below will be focused only on data obtained with the B3LYP-D2 method.

For the ruthenium case a relatively small activation barrier was observed (64 $kJ{\cdot}mol^{-1}$) and subsequent AcOH elimination required 78 $kJ{\cdot}mol^{-1}$ more energy. Therefore we suggest that the measured *AE* for the AcOH loss reflects its dissociation from the ruthenium complex and not the C-H activation itself.

Table 3.8: Calculated and experimental activation energies for AcOH loss.

Method	Metal					
	Ru		Cu		Pd	
Experimental (CID), kJ·mol^{-1}	113 ± 3		138 ± 5		65 ± 3	
	E_{diss}	E_{TS}	E_{diss}	E_{TS}	E_{diss}	E_{TS}
B3LYP-D2, kJ·mol^{-1}	142	64	156	139	71	83
B3LYP-D3, kJ·mol^{-1}	-	-	152	143	64	82
B3LYP, kJ·mol^{-1}	103	67	111	140	29	74

For the copper complex, the activation barrier (139 kJ·mol^{-1}) matches well with the experimentally obtained value (138 ± 5 kJ·mol^{-1}) and is similar when compared to the energy demand for AcOH elimination from the activated complex. Experiments showed that the elimination of AcOH is less abundant than that of 2-PhPy, and also less energy demanding. This indicates that the C-H activation step is rate limiting and most likely reflects the AE that we observe experimentally.

Interpretation of results for the Pd complex is complicated by the fact that we observe a mixture of isomers. The experimentally observed AE value however is rather small, thus we believe that it is largely dominated by elimination of AcOH from the activated complex $^{Pd}3_a$.

3.4.5 Hammett studies

It has been shown [117] that linear free energy correlations can be studied using mass spectrometry. One of the most commonly used ways to study organic reaction mechanisms, also in the gas phase, is the Hammett equation and subsequent interpretation of the associated Hammett plots. Therefore we decided to study the ions of form $[M(\text{2-PhPy})(\text{acid-H})(L)]^+$ where acid corresponds to the *m*- and *p*- substituted benzoic acids. We generated the ions in the gas phase, mass-selected them, and studied their C-H activation upon CID. In order to obtain a reliable Hammett correlation, five or more benzoic acid derivatives should be studied (*e.g.* *m*-NO_2, *p*-NO_2, *m*-Cl, H, *p*-CH_3, *p*-CH_3O, where *p*-NO_2 and *p*-CH_3O derivatives are included in order to decide what type of σ constants should be used (σ, σ^+ or σ^-)).

To this end we have studied a large series of LCu(OAc)/2-PhPy/acid mixtures in acetonitrile to generate the above-mentioned intermediates. We have turned to the copper catalyzed activation of 2-phenylpyridine, where the measured AE's agree well with theory

Table 3.9: Measured activation energies for two losses and the corresponding Hammett constants.

Substituent	$AE_{\text{-acid}}$, kJ·mol^{-1}	$AE_{\text{-2-PhPy}}$, kJ·mol^{-1}	$\sigma_{m,p}$	$\sigma^{+}_{m,p}$
-H	149	157	0	0
p-NH_2	148	153	-0.66	-1.3
p-NO_2	152	163	0.78	0.78
p-OCH_3	155	157	-0.27	0.778
p-OH	148	156	-0.37	-0.92
p-$N(CH_3)_2$	148	151	-0.83	-1.7
m-OCH_3	152	159	0.12	0.12
m-OH	148	157	0.12	0.12
m-NO_2	157	162	0.71	0.71
m-Br	148	154	0.39	0.39

and reflect the C-H activation step. The results of CID experiments are summarized in Table 3.9.

As the table shows, the correlation between the obtained AE's and Hammett σ constants is rather poor. This is due to the fact that AE's are similar and differ in the range of experimental error which is 3-5 kJ·mol^{-1}. Therefore we decided to investigate the relationships between σ constants and relative cross-sections for each derivative that can be determined with a greater precision [32,118]. To this end, we determined the relative abundances of the fragment ions [Cu(2-PhPy)(acid-H)]$^+$ and [Cu(2-PhPy)((2-PhPy)-H)]$^+$ at a collision energy where the branching ratio has reached the plateau of the energy resolved CID curve. Then the logarithms of the extracted abundances were plotted against the corresponding σ constant.

Figure 3.39 shows the obtained Hammett plot for 2-PhPy loss. The Hammett ρ constant is -0.07 which points to a negligible effect that a substituent on the benzoate counter ion has on the binding energy between copper and 2-PhPy. Therefore we used the 2-PhPy elimination to anchor the substituent effect for the C-H activation step: the logarithms of the branching ratios between the acid and 2-PhPy losses were plotted against the corresponding Hammett σ parameter (Figure 3.40).

Figure 3.40a shows the Hammett plot created for the logarithm of branching ratio between the two elimination channels and the σ constant. The resulting ρ constant obtained form the plot is 0.93.

As the ρ constant for CH activation lies in the region $0<\rho<1$, the reaction is only weakly

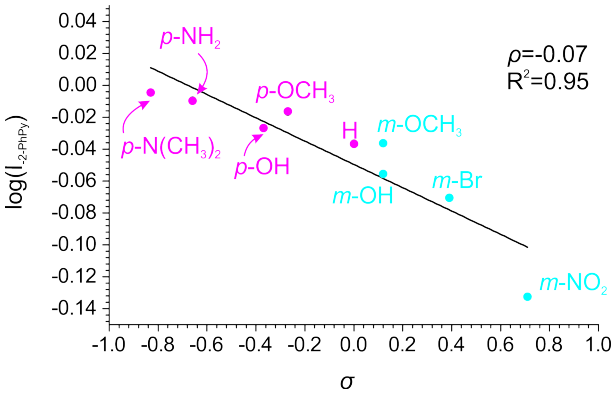

Figure 3.39: Hammett plot for Cu-catalyzed C-H activation of 2-phenylpyridine showing the dependence of the logarithm of the relative intensity of 2-PhPy loss at plateau *vs* σ constant.

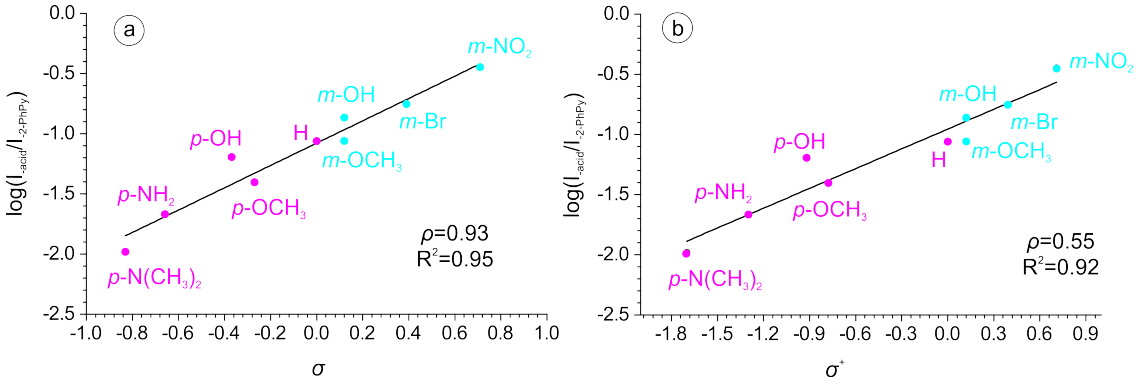

Figure 3.40: a) Hammett plot for the Cu-catalyzed C-H activation of 2-phenylpyridine showing the dependence of the logarithm of the branching ratio between acid and 2-phenylpyridine losses *vs* the σ constant; b) Hammett plot for the Cu-catalyzed C-H activation of 2-phenylpyridine showing the dependence of the logarithm of the branching ratio between acid and 2-phenylpyridine losses vs the σ^+ constant.

dependent on the electronic effects of the substituents, and negative charge is created on the reactive center. The small absolute value of ρ also indicates the low ionic character of the transition state which proves the cyclic character of our reaction. The plot shows that the ρ constant for CH activation is positive, which implies that the reaction can be accelerated by the creation of positive charge on the reactive center. In other words, electron-acceptor substituents (with $\sigma > 0$) can accelerate the reaction.

The use of σ^+ constants did not provide a better correlation (Figure 3.40b) which shows that the resonance effect from the substituent to the reaction center does not play a pronounced role in this reaction.

In order to investigate the role of the metal-carbon bond formation in greater detail, we have reoptimized the structures for C-H activation using benzoate and 4-nitrobenzoate

counter ions. Figures 3.41-3.43 show the potential energy surfaces, calculated for all three investigated metals. Figure 3.44 shows the bond lengths in each of the six-membered transition structures allowing comparison of the electronic effect of the electron withdrawing NO_2 group on the mechanism of C-H activation. With all three of the metals, the metal-carbon distance decreases while the metal-oxygen and carbon-hydrogen distances both increase. These observations are in line with the theorized increasingly electrophilic metal center. In each case, the presence of NO_2 reduced the energy required for 4-nitrobenzoic acid loss in comparison with benzoic acid. This further supports the experimental observation of an increasingly electrophilic metal center.

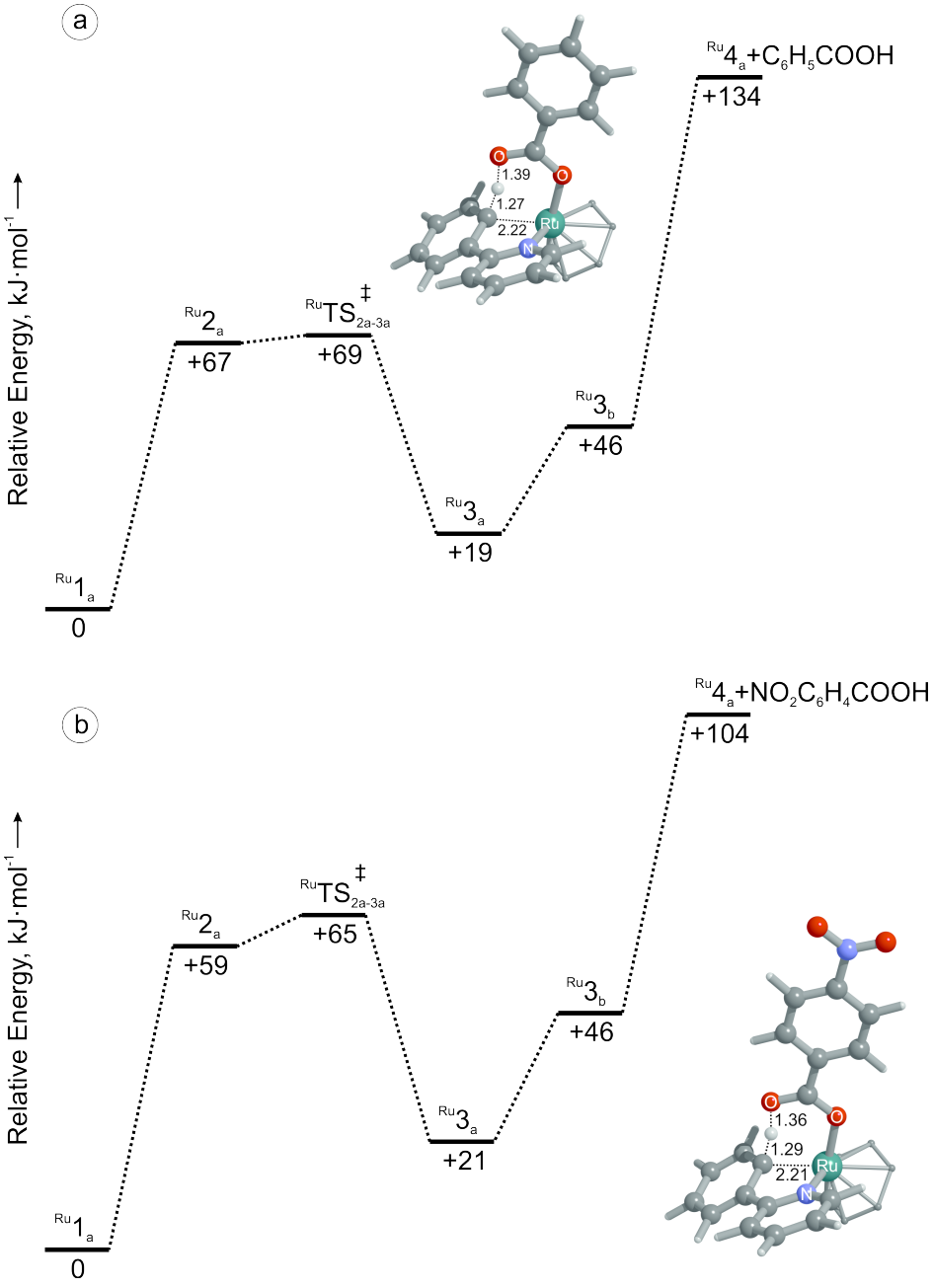

Figure 3.41: a) Zero point potential energy surface (B3LYP/6-31G*:SDD(Ru)) for the Ru assisted C-H activation of 2-PhPy with a $C_6H_5COO^-$ counter ion; b) zero point potential energy surface (B3LYP/6-31G*:SDD(Ru)) for the Ru assisted C-H activation of 2-PhPy with a $NO_2C_6H_4COO^-$ counter ion. Representations of structures are shown in Scheme 3.9. All distances are in Å.

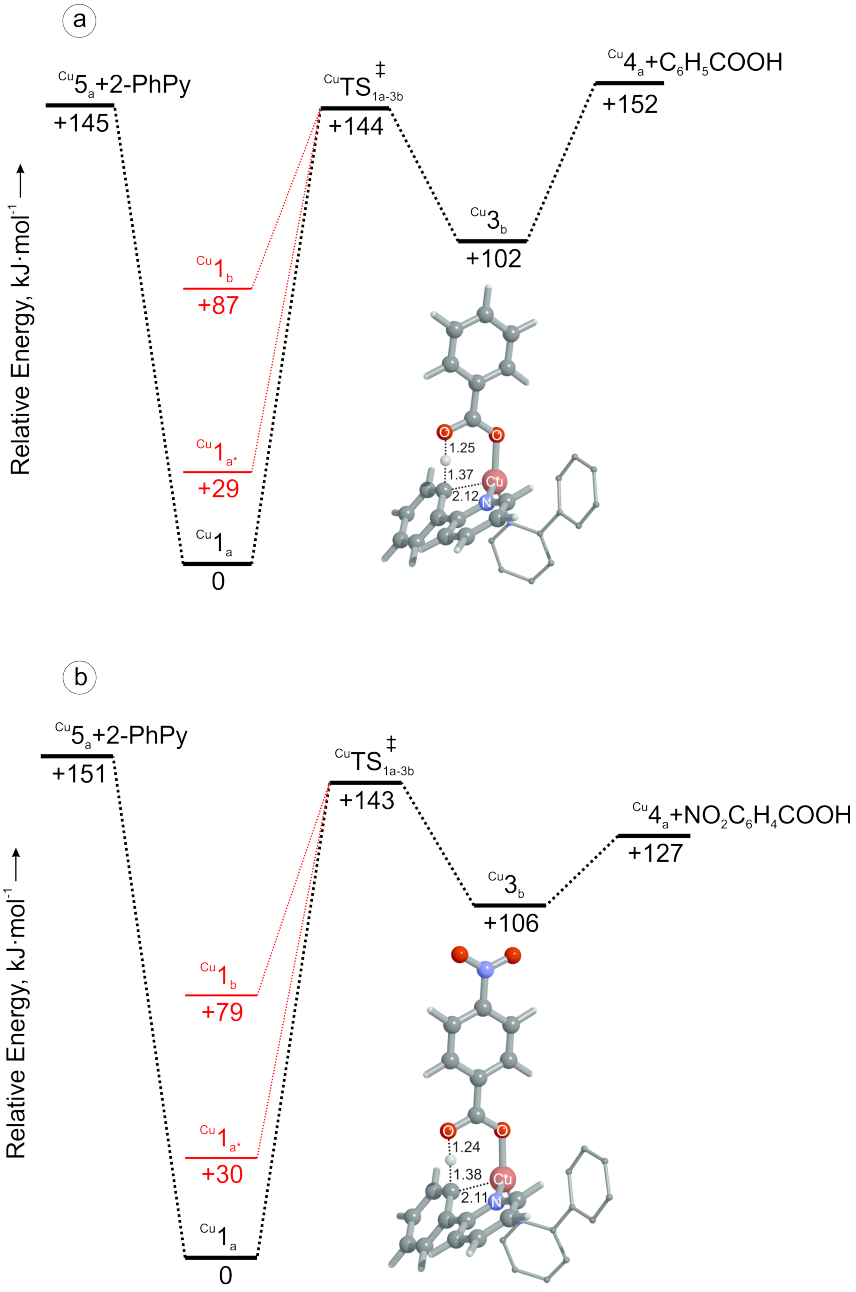

Figure 3.42: a) Zero point potential energy surface (B3LYP/6-31G*:SDD(Cu)) for the Cu assisted C-H activation of 2-PhPy with a $C_6H_5COO^-$ counter ion; b) zero point potential energy surface (B3LYP/6-31G*:SDD(Cu)) for the Cu assisted C-H activation of 2-PhPy with a $NO_2C_6H_4COO^-$ counter ion. Representations of structures are shown in Scheme 3.9. All distances are in Å.

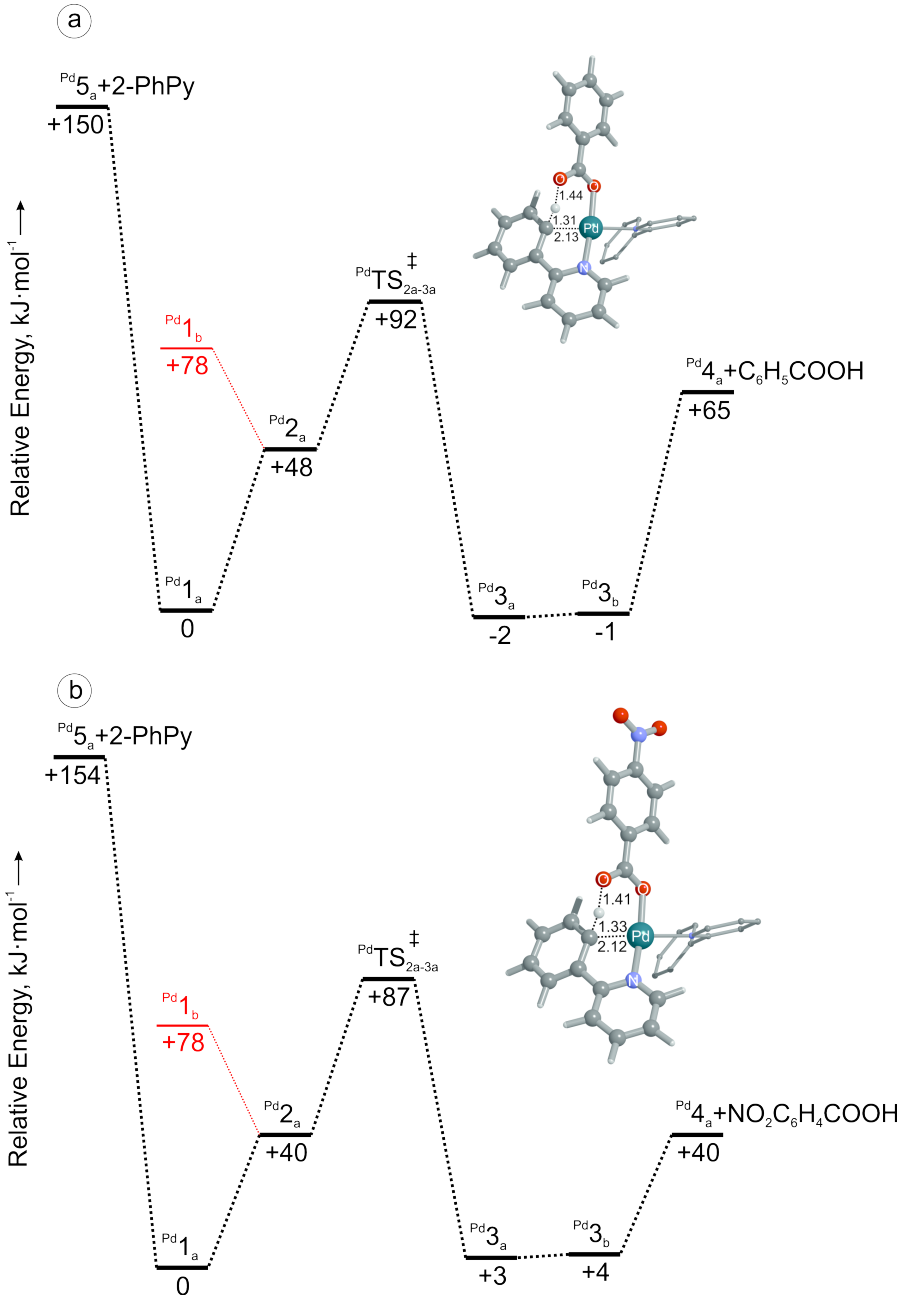

Figure 3.43: a) Zero point potential energy surface (B3LYP/6-31G*:SDD(Pd)) for the Pd assisted C-H activation of 2-PhPy with a $C_6H_5COO^-$ counter ion; b) zero point potential energy surface (B3LYP/6-31G*:SDD(Pd)) for the Pd assisted C-H activation of 2-PhPy with a $NO_2C_6H_4COO^-$ counter ion. Representations of structures are shown in Scheme 3.9. All distances are in Å.

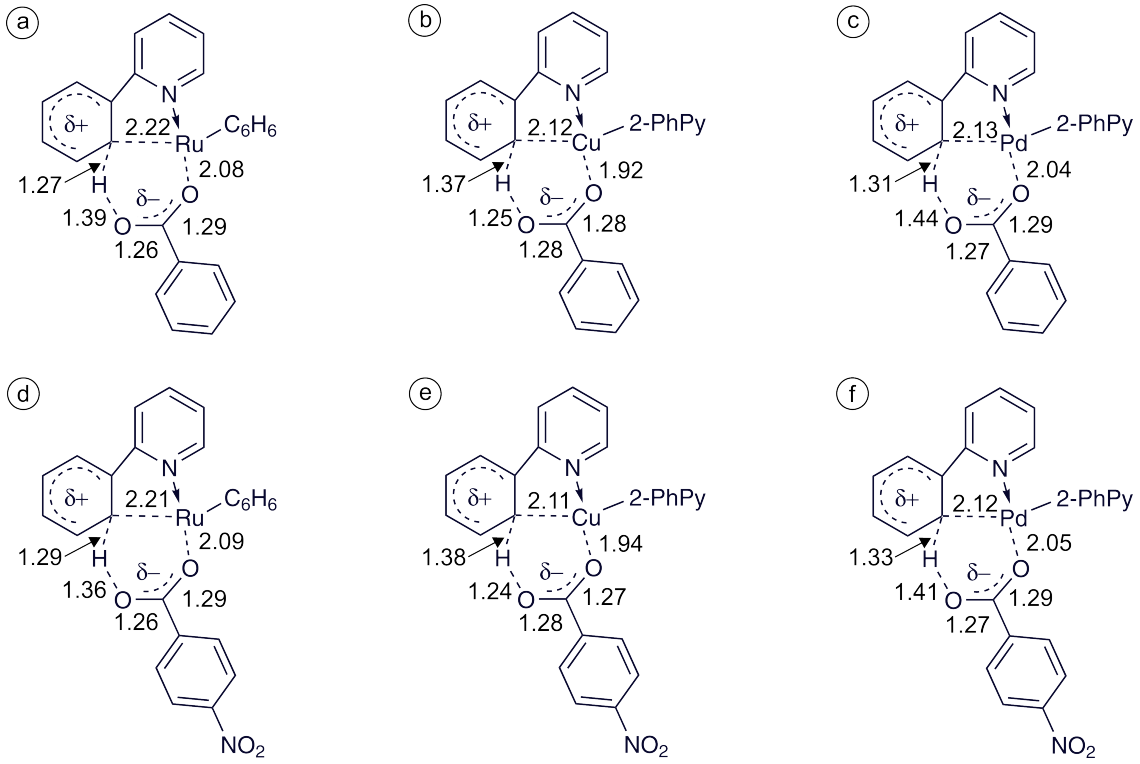

Figure 3.44: Six-membered transition structures showing key bond lengths for a) $^{\mathrm{Ru}}\mathrm{TS}_{\mathrm{2a\text{-}3a}}$, b) $^{\mathrm{Cu}}\mathrm{TS}_{\mathrm{1a\text{-}3b}}$ and c) $^{\mathrm{Pd}}\mathrm{TS}_{\mathrm{2a\text{-}3a}}$ with a benzoate counter ion, and d) $^{\mathrm{Ru}}\mathrm{TS}_{\mathrm{2a\text{-}3a}}$, e) $^{\mathrm{Cu}}\mathrm{TS}_{\mathrm{1a\text{-}3b}}$, and f) $^{\mathrm{Pd}}\mathrm{TS}_{\mathrm{2a\text{-}3a}}$ with a 4-nitrobenzoate counter ion. All distances are in Å.

Chapter 4

Conclusion

The studies described in this dissertation represent some of the fundamental findings for organometallic chemistry research. The employment of ESI-MS, IRMPD and quantum chemical calculations can be very helpful for the investigation of reaction mechanisms. Our results show, that one also needs to be careful in while interpreting and applying them to the specific cases.

The studies of $Cu(OAc)_2$ behavior in dry organic solvents (methanol and acetonitrile) revealed a high degree of clusterization, and that the clusters with three to six copper atoms dominate the spectra. The abundance of these clusters however is strongly dependent on the presence of water in the solution: even small water contents significantly suppress the amount of clusters. Monomeric copper complexes become dominant with the water contents of 5 vol. %. This finding could be important for further investigations of reaction mechanisms catalyzed by copper acetate and help in distinguishing between single-atom and cluster chemistry for what is driving the catalytic cycle.

In the second study - investigation of copper catalyzed cross coupling between thiol esters and boronic acids - we were able to follow the kinetics of the reaction and determine the concentration changes of reactants and products. The investigation of reaction intermediates was not very successful, probably as the result of either a high abundance of sodiated ions in the spectrum, or because of the high reactivity of copper-boronate complexes. Although the copper complexes were little abundant, we profited from the large intensities of reagent and product complexes with sodium. This fact allowed us to monitor the reaction kinetics with ESI-MS and obtain the rate constants at different temperatures. The determined activation energy for the reaction according to the Arrhenius equation was found to be 81 $\pm$ 5 $kJ \cdot mol^{-1}$. The Gibbs energy at 298K was determined as 103 $\pm$ 5

$kJ \cdot mol^{-1}$, activation enthalpy as 76 ± 5 $kJ \cdot mol^{-1}$ and the activation entropy yielded -100 ± 5 $J \cdot mol^{-1} \cdot K^{-1}$.

In the third project, an investigation of complexes with three isomeric phenylpyridines and Ni^{2+} cations was carried out. The study revealed that 3- and 4-PhPy behave similarly to each other, however 2-PhPy differs in two ways. First, the steric hindrance of 2-PhPy prevents the formation of the three- and higher ligated species. Second, in the nickel - 2PhPy complexes one of the *o*-C-H bonds of the phenyl ring comes in close proximity to the metal center which enables activation of the C-H bond and formation of a metallocycle. IM-MS was found to be a useful method for the investigation of the coordination and steric effects for the isomeric organometallic complexes, such as $[NiCl(PhPy)_2]^+$.

The last study was into the mechanism of carboxylate assisted C-H activation. We have shown that the carboxylate assisted C-H activation of 2-phenylpyridine can be studied in the gas phase with ruthenium, copper, and palladium catalysts. IRMPD spectroscopy confirmed that isolation of ruthenium acetate and copper acetate complexes with non-activated 2-phenylpyridine is possible. It was also possible to induce the C-H activation of these complexes in the collision cell and study it in greater detail. We have determined the energies required for C-H activation and subsequent acetic acid elimination. In the case of palladium, we have observed a mixture of activated and non-activated complexes with 2-PhPy. Further careful analysis revealed that the experimentally observed appearance energy for AcOH loss in the case of Ru and Pd reflects the binding energy of acetic acid to the metal center after the C-H activation step. On the other hand the energy determined for copper complexes reflects the energy needed for C-H activation. Potential energy surfaces for each of the C-H activation cases were constructed using DFT calculations. Similar structures were found for all three metals along the reaction coordinate, however their relative energies are very different.

The C-H activation step was also studied using Hammett plots for copper complexes with a series of substituted benzoates. The results show that electron-withdrawing substituents at the benzoate counter ion accelerate the C-H activation step. The explanation can be found in the cyclic nature of the transition structure, where C-H bond dissociation is assisted by the formation of a metal-carbon bond. Carboxylates derived from stronger acids further support the formation of the metal-carbon bond.

Bibliography

[1] X.-F. Wu, P. Anbarasan, H. Neumann, M. Beller. *Ang. Chem. Int. Ed.* **49**, 9047–9050 (2010).

[2] E.-i. Negishi. *Ang. Chem. Int. Ed.* **50**, 6738–6764 (2011).

[3] A. Suzuki, Y. Yamamoto. *Chem. Lett.* **40**, 894–901 (2011).

[4] A. Suzuki. *Ang. Chem. Int. Ed.* **50**, 6722–6737 (2011).

[5] F. D. Armin de Meijere (editor) *Metal-Catalyzed Cross-Coupling Reactions, Second Edition*, (WILEY-VCH Verlag GmbH & Co. KGaA, Weinheim2004).

[6] D. H. Ringger, P. Chen. *Ang. Chem. Int. Ed.* **52**, 4686–4689 (2013).

[7] M. Yamashita, J. B. Fenn. *J. Phys. Chem.* **88**, 4451–4459 (1984).

[8] J. B. Fenn, M. Mann, C. K. Meng, S. F. Wong, C. M. Whitehouse. *Science* **246**, 64–71 (1989).

[9] J. B. Fenn. *Ang. Chem. Int. Ed.* **42**, 3871–3894 (2003).

[10] M. N. Eberlin. *Eur. J. Mass Spectrom.* **13**, 19–28 (2007).

[11] L. S. Santos. *Eur. J. Org. Chem.* 235–253 (2008).

[12] L. Santos (editor) *Reactive Intermediates*, (Wiley-VCH Verlag GmbH & Co. KGaA2010).

[13] J. M. Riveros, M. Sena, G. H. Guedes, L. A. Xavier, R. Slepetys. *Pure and Applied Chemistry* **70**, 1969–1976 (1998).

[14] C. Aubry, J. L. Holmes. *Int. J. Mass Spectrom.* **200**, 277–284 (2000).

[15] K. L. Vikse, M. P. Woods, J. S. McIndoe. *Organometallics* **29**, 6615–6618 (2010).

[16] K. L. Vikse, Z. Ahmadi, J. Luo, N. van der Wal, K. Daze, N. Taylor, J. S. McIndoe. *Int. J. Mass Spectrom.* **323**, 8–13 (2012).

[17] A. T. Lubben, J. S. McIndoe, A. S. Weller. *Organometallics* **27**, 3303–3306 (2008).

[18] D. Agrawal, D. Schroeder, C. M. Frech. *Organometallics* **30**, 3579–3587 (2011).

[19] H. Wang, J. Liu, R. G. Cooks, Z. Ouyang. *Ang. Chem. Int. Ed.* **49**, 877–880 (2010).

[20] X. Yan, R. Augusti, X. Li, R. G. Cooks. *ChemPlusChem* **78**, 1142–1148 (2013).

[21] D. Agrawal, D. Schroeder. *Organometallics* **30**, 32–35 (2011).

[22] F. Coelho, M. N. Eberlin. *Ang. Chem. Int. Ed.* **50**, 5261–5263 (2011).

[23] L. P. E. Yunker, R. L. Stoddard, J. S. McIndoe. *J. Mass Spectrom.* **49**, 1–8 (2014).

[24] G. Gerdes, P. Chen. *Organometallics* **22**, 2217–2225 (2003).

[25] J. A. Labinger, J. E. Bercaw, M. Tilset. *Organometallics* **25**, 805–808 (2006).

[26] G. Gerdes, P. Chen. *Organometallics* **25**, 809–811 (2006).

[27] N. C. Polfer. *Chem. Soc. Rev.* **40**, 2211–2221 (2011).

[28] J. Roithova. *Chem. Soc. Rev.* **41**, 547–559 (2012).

[29] S. Gronert. *Chem. Rev.* **101**, 329–360 (2001).

[30] S. Gronert. *Mass Spectrom. Rev.* **24**, 100–120 (2005).

[31] M. A. Schade, J. E. Feckenstem, P. Knochel, K. Koszinowski. *J. Org. Chem.* **75**, 6848–6857 (2010).

[32] K. L. Vikse, M. A. Henderson, A. G. Oliver, J. S. McIndoe. *Chem. Commun.* **46**, 7412–7414 (2010).

[33] J. Roithova, D. Schroder. *Chem. Eur. J.* **14**, 2180–2188 (2008).

[34] J. Roithova, P. Milko. *J. Am. Chem. Soc.* **132**, 281–288 (2010).

[35] J. Roithova, S. Jankova, L. Jasikova, J. Vana, S. Hybelbauerova. *Ang. Chem. Int. Ed.* **51**, 8378–8382 (2012).

[36] C. J. Shaffer, D. Schroder, C. Guetz, A. Luetzen. *Ang. Chem. Int. Ed.* **51**, 8097–8100 (2012).

[37] L. Fiebig, J. Kuttner, G. Hilt, M. C. Schwarzer, G. Frenking, H.-G. Schmalz, M. Schaefer. *J. Org. Chem.* **78**, 10485–10493 (2013).

[38] S. Banerjee, S. Mazumdar. *Int. J. Anal. Chem.* 282574 (2012).

[39] R. B. Cole (editor) *Electrospray and MALDI Mass Spectrometry: Fundamentals, Instrumentation, Practicalities, and Biological Applications, Second Edition*, (Wiley2012).

[40] J. V. Iribarne, B. A. Thomson. *J. Chem. Phys.* **64**, 2287–2294 (1976).

[41] S. Nguyen, J. B. Fenn. *P. Nat. Acad. Sci. USA* **104**, 1111–1117 (2007).

[42] M. Gamero-Castano, J. F. de la Mora. *J. Chem. Phys.* **113**, 815–832 (2000).

[43] J. F. de la Mora. *Anal. Chim. Acta* **406**, 93–104 (2000).

[44] D. Schroder, T. Weiske, H. Schwarz. *Int. J. Mass Spectrom.* **219**, 729–738 (2002).

[45] R. A. J. O'Hair. *Chem. Commun.* 1469–1481 (2006).

[46] G. J. Vanberkel, G. L. Glish, S. A. McLuckey. *Anal. Chem.* **62**, 1284–1295 (1990).

[47] W. Paul. *Ang. Chem. Int. Ed.* **29**, 739–748 (1990).

[48] N. B. Cech, C. G. Enke. *Mass Spectrom. Rev.* **20**, 362–387 (2001).

[49] W. Paul. *Rev. Mod. Phys.* **62**, 531–540 (1990).

[50] E. W. Mcdaniel, W. S. Barnes, D. W. Martin. *Rev. Sci. Instrum.* **33**, 2–7 (1962).

[51] D. E. Clemmer, R. R. Hudgins, M. F. Jarrold. *J. Am. Chem. Soc.* **117**, 10141–10142 (1995).

[52] A. B. Kanu, P. Dwivedi, M. Tam, L. Matz, J. Hill, Herbert H. *J. Mass Spectrom.* **43**, 1–22 (2008).

[53] F. Lanucara, S. W. Holman, C. J. Gray, C. E. Eyers. *Nature Chem.* **6**, 281–294 (2014).

[54] C. Lapthorn, F. Pullen, B. Z. Chowdhry. *Mass Spectrom. Rev.* **32**, 43–71 (2013).

[55] D. Schroder, M. Budesinsky, J. Roithova. *J. Am. Chem. Soc.* **134**, 15897–15905 (2012).

[56] S. D. Pringle, K. Giles, J. L. Wildgoose, J. P. Williams, S. E. Slade, K. Thalassinos, R. H. Bateman, M. T. Bowers, J. H. Scrivens. *Int. J. Mass Spectrom.* **261**, 1–12 (2007).

[57] A. Revesz, D. Schroder, T. A. Rokob, M. Havlik, B. Dolensky. *Phys. Chem. Chem. Phys.* **14**, 6987–6995 (2012).

[58] C. Trage, M. Diefenbach, D. Schroder, H. Schwarz. *Chem. Eur. J.* **12**, 2454–2464 (2006).

[59] https://depts.washington.edu/bushlab/instruments/ .

[60] M. J. Frisch, G. W. Trucks, H. B. Schlegel, G. E. Scuseria, M. A. Robb, J. R. Cheeseman, G. Scalmani, V. Barone, B. Mennucci, G. A. Petersson, H. Nakatsuji, M. Caricato, X. Li, H. P. Hratchian, A. F. Izmaylov, J. Bloino, G. Zheng, J. L. Sonnenberg, M. Hada, M. Ehara, K. Toyota, R. Fukuda, J. Hasegawa, M. Ishida, T. Nakajima, Y. Honda, O. Kitao, H. Nakai, T. Vreven, J. A. Montgomery, Jr., J. E. Peralta, F. Ogliaro, M. Bearpark, J. J. Heyd, E. Brothers, K. N. Kudin, V. N. Staroverov, R. Kobayashi, J. Normand, K. Raghavachari, A. Rendell, J. C. Burant, S. S. Iyengar, J. Tomasi, M. Cossi, N. Rega, J. M. Millam, M. Klene, J. E. Knox, J. B. Cross, V. Bakken, C. Adamo, J. Jaramillo, R. Gomperts, R. E. Stratmann, O. Yazyev, A. J. Austin, R. Cammi, C. Pomelli, J. W. Ochterski, R. L. Martin, K. Morokuma, V. G. Zakrzewski, G. A. Voth, P. Salvador, J. J. Dannenberg, S. Dapprich, A. D. Daniels, . Farkas, J. B. Foresman, J. V. Ortiz, J. Cioslowski, D. J. Fox. *Gaussian-09 Revision D.01* . Gaussian Inc. Wallingford CT 2009.

[61] *TURBOMOLE V6.2 2010, a development of University of Karlsruhe and Forschungszentrum Karlsruhe GmbH, 1989-2007, TURBOMOLE GmbH, since 2007; available from http://www.turbomole.com.*.

[62] C. Lee, W. Yang, R. G. Parr. *Phys. Rev. B* **37**, 785–789 (1988).

[63] A. D. Becke. *Phys. Rev. A* **38**, 3098–3100 (1988).

[64] A. D. Becke. *J. Chem. Phys.* **98**, 5648–5652 (1993).

[65] P. J. Stephens, F. J. Devlin, C. F. Chabalowski, M. J. Frisch. *J. Phys. Chem.* **98**, 11623–11627 (1994).

[66] F. Weigend, R. Ahlrichs. *Phys. Chem. Chem. Phys.* **7**, 3297–3305 (2005).

[67] S. Grimme, J. Antony, S. Ehrlich, H. Krieg. *J. Chem. Phys.* **132**, 154104 (2010).

[68] Y. Zhao, D. Truhlar **120**, 215–241 (2008).

[69] L. Noodleman. *J. Chem. Phys.* **74**, 5737–5743 (1981).

[70] S. Grimme. *J. Comput. Chem.* **27**, 1787–1799 (2006).

[71] D. Schroder, H. Schwarz, P. Milko, J. Roithova. *J. Phys. Chem. A* **110**, 8346–8353 (2006).

[72] A. Simon, C. Joblin, N. Polfer, J. Oomens. *J. Phys. Chem. A* **112**, 8551–8560 (2008).

[73] http://www.thermoscientific.de/content/dam/tfs/ATG/CMD/CMDNormalized-Collision-Energy-Technology-EN.pdf .

[74] E.-L. Zins, C. Pepe, D. Schroder. *J. Mass Spectrom.* **45**, 1253–1260 (2010).

[75] E.-L. Zins, D. Rondeau, P. Karoyan, C. Fosse, S. Rochut, C. Pepe. *J. Mass Spectrom.* **44**, 1668–1675 (2009).

[76] E.-L. Zins, C. Pepe, D. Rondeau, S. Rochut, N. Galland, J.-C. Tabet. *J. Mass Spectrom.* **44**, 12–17 (2009).

[77] F. Derwa, E. Depauw, P. Natalis. *J. Am. Soc. Mass Spec.* **26**, 117–118 (1991).

[78] C. Collette, E. De Pauw. *Rapid Commun. Mass Spectrom.* **12**, 165–170.

[79] G. H. Luo, I. Marginean, A. Vertes. *Anal. Chem.* **74**, 6185–6190 (2002).

[80] J. F. Greisch, V. Gabelica, F. Remacle, E. De Pauw. *Rapid Commun. Mass Spectrom.* **17**, 1847–1854 (2003).

[81] G. Bouchoux, J. Y. Salpin, D. Leblanc. *Int. J. Mass Spectrom.* **153**, 37–48 (1996).

[82] J. Hyvl, D. Agrawal, R. Pohl, M. Suri, F. Glorius, D. Schroder. *Organometallics* **32**, 807–816 (2013).

[83] J. M. Villalobos, J. Srogl, L. S. Liebeskind. *J. Am. Chem. Soc.* **129**, 15734–15735 (2007).

[84] J. N. Vanniekerk, F. R. L. Schoening. *Nature* **171**, 36–37 (1953).

[85] S. Sattar, D. Eden. *J. Phys. Chem.* **86**, 140–144 (1982).

[86] G. C. Didonato, B. K. L. *Int. J. Mass Spectrom.* **69**, 67–83 (1986).

[87] A. Tsybizova, J. Tarabek, M. Buchta, P. Holy, D. Schroeder. *Rapid Commun. Mass Spectrom.* **26**, 2287–2294 (2012).

[88] A. Tsybizova, J. Roithova. *Mass Spectrom. Rev.* n/a–n/a (2015).

[89] L. S. Liebeskind, J. Srogl. *Org. Lett.* **4**, 979–981 (2002).

[90] Z. Zhang, L. S. Liebeskind. *Org. Lett.* **8**, 4331–4333 (2006).

[91] H. Yang, H. Li, R. Wittenberg, M. Egi, W. Huang, L. S. Liebeskind. *J. Am. Chem. Soc.* **129**, 1132–1140 (2007).

[92] H. Prokopcova, L. Pisani, C. O. Kappe. *Synlett* 43–46 (2007).

[93] A. Morita, S. Kuwahara. *Org. Lett.* **8**, 1613–1616 (2006).

[94] S. Oumouch, M. Bourotte, M. Schmitt, J. J. Bourguignon. *Synthesis* 25–27 (2005).

[95] A. Lengar, C. O. Kappe. *Org. Lett.* **6**, 771–774 (2004).

[96] F. A. Alphonse, F. Suzenet, A. Keromnes, B. Lebret, G. Guillaumet. *Org. Lett.* **5**, 803–805 (2003).

[97] A. Varela-Alvarez, L. S. Liebeskind, D. G. Musaev. *Organometallics* **31**, 7958–7968 (2012).

[98] L. Wang, C. Dai, S. K. Burroughs, S. L. Wang, B. Wang. *Chem. Eur. J.* **19**, 7587–7594 (2013).

[99] A. E. King, T. C. Brunold, S. S. Stahl. *J. Am. Chem. Soc.* **131**, 5044–5045 (2009).

[100] E. Ferrer Flegeau, C. Bruneau, P. H. Dixneuf, A. Jutand. *J. Am. Chem. Soc.* **133**, 10161–10170 (2011).

[101] N. R. Deprez, M. S. Sanford. *J. Am. Chem. Soc.* **131**, 11234–11241 (2009).

[102] S. R. Whitfield, M. S. Sanford. *J. Am. Chem. Soc.* **129**, 15142–15143 (2007).

[103] D. Schroder, M. Engeser, M. Bronstrup, C. Daniel, J. Spandl, H. Hartl. *Int. J. Mass Spectrom.* **228**, 743–757 (2003).

[104] D. Schroder, H. Schwarz. *Can. J. Chem.* **83**, 1936–1940 (2005).

[105] M. Besora, J.-L. Carreon-Macedo, A. Cimas, J. N. Harvey. *Advances In Inorganic Chemistry, Vol 61: Metal Ion Controlled Reactivity* **61**, 573–623 (2009).

[106] L. Ackermann. *Chem. Rev.* **111**, 1315–1345 (2011).

[107] D. H. Ess, S. M. Bischof, J. Oxgaard, R. A. Periana, W. A. Goddard. *Organometallics* **27**, 6440–6445 (2008).

[108] D. Lapointe, K. Fagnou. *Chemistry Letters* **39**, 1118–1126 (2010).

[109] R. Jazzar, J. Hitce, A. Renaudat, J. Sofack-Kreutzer, O. Baudoin. *Chem. Eur. J.* **16**, 2654–2672 (2010).

[110] X. Chen, X.-S. Hao, C. E. Goodhue, J.-Q. Yu. *J. Am. Chem. Soc.* **128**, 6790–6791 (2006).

[111] A. John, K. M. Nicholas. *J. Org. Chem.* **76**, 4158–4162 (2011).

[112] C. J. Shaffer, A. Revesz, D. Schroder, L. Severa, F. Teply, E.-L. Zins, L. Jasikova, J. Roithova. *Ang. Chem. Int. Ed.* **51**, 10050–10053 (2012).

[113] P. Milko, J. Roithova, N. Tsierkezos, D. Schroeder. *J. Am. Chem. Soc.* **130**, 7186–7187 (2008).

[114] T. A. Rokob, L. Rulisek, J. Srogl, A. Revesz, E. L. Zins, D. Schroeder. *Inorg. Chem.* **50**, 9968–9979 (2011).

[115] L. Jasikova, E. Hanikyrova, D. Schroeder, J. Roithova. *J. Mass Spectrom.* **47**, 460–465 (2012).

[116] S. Grimme, W. Hujo, B. Kirchner. *Phys. Chem. Chem. Phys.* **14**, 4875–4883 (2012).

[117] A. G. Harrison. *J. Mass Spectrom.* **34**, 577–589.

[118] H. Lioe, R. A. J. O'Hair. *Org. Biomol. Chem.* **3**, 3618–3628 (2005).